ABSTRACT

STRUCTURAL STUDIES TO DETERMINE THE MECHANISMS SUPPORTING MULTIFERROIC AND FERROELECTRIC PROPERTIES OF COMPLEX OXIDES

by
Han Zhang

Multiferroics are a class of materials which possess both magnetic and electrical polarization with possible coupling between them. They show promise to enable new sensors and data storage devices with novel features, such as the possibility of writing polarization bits with magnetic fields at low power. The coexisting magnetic and ferroelectric order parameters are usually weakly coupled, preventing practical use. The development and study of new classes of materials with large magnetoelectric couplings is of high importance. Understanding the structure of these materials is key to this effort.

As one class of these systems, the $RX_3(BO_3)_4$ has been shown to have a giant magnetoelectric (for R=Ho, X=Al) effect of $P = 0.36\mu C/cm^2$ in magnetic fields, which is significantly higher than the reported values for other multiferroic compounds. The atomic level origin is still not understood. In this work, macroscopic and atomic level properties of the full class $RX_3(BO_3)_4$ (R=Ho, Gd, Eu, Sm, Nd, and X=Al or Fe) are explored by various experimental measurements, complemented by density functional theory calculations. In $HoAl_3(BO_3)_4$, an anomalous change in the structure is found in the temperature range where large magnetoelectric effects occur. No large structural change or distortion of the HoO_6 polyhedra is seen to occur with a magnetic field. The magnetic field dependent structural measurements reveal enhanced structural correlation between neighboring HoO_6 polyhedra. A qualitative atomic-level description of the mechanism behind the large electric polarization induced by magnetic fields in the general class of

$RAl_3(BO_3)_4$ systems (R= rare earth) is developed. A detailed structure related mechanism for the general $RX_3(BO_3)_4$ is developed by high-resolution x-ray diffraction measurements.

Another system under study is the standard class of ferroelectrics: $ATiO_3$ including $SrTiO_3$ and $BaTiO_3$. The A=Sr system is known not to possess a polarization state in bulk form. In this work, pressure dependent structural measurements on monodispersed nanoscale $SrTiO_3$ (STO) samples with average diameters of 10 to ~80 nm are conducted. A structural phase diagram of nanoscale $SrTiO_3$ with reduced dimension is developed. A robust pressure independent polar structure is detected in the 10 nm sample for pressures up to 13 GPa while a size-dependent cubic to tetragonal transition occurs (at $P = P_c$) for larger particle sizes. The stability and polar characteristics of the A=Ba system are explored, and mechanisms for stabilizing the polar phase in nanoscale $SrTiO_3$ and $BaTiO_3$ are examined.

STRUCTURAL STUDIES TO DETERMINE THE MECHANISMS SUPPORTING MULTIFERROIC AND FERROELECTRIC PROPERTIES OF COMPLEX OXIDES

by
Han Zhang

A Dissertation
Submitted to the Faculty of
New Jersey Institute of Technology and
Rutgers, The State University of New Jersey-Newark,
in Partial Fulfillment of the Requirements for the Degree of
Doctor of Philosophy in Applied Physics

Department of Physics

May 2018

.

APPROVAL PAGE

STRUCTURAL STUDIES TO DETERMINE THE MECHANISMS SUPPORTING MULTIFERROIC AND FERROELECTRIC PROPERTIES OF COMPLEX OXIDES

Han Zhang

Dr. Trevor A. Tyson, Dissertation Advisor — Date
Distinguished Professor of Applied Physics, NJIT

Dr. Onofrio L. Russo, Committee Member — Date
Associate Professor of Applied Physics, NJIT

Dr. Tao Zhou, Committee Member — Date
Associate Professor of Applied Physics, NJIT

Dr. Keun H. Ahn, Committee Member — Date
Associate Professor of Applied Physics, NJIT

Dr. Zhen Wu, Committee Member — Date
Professor of Department of Physics, Rutgers-Newark

BIOGRAPHICAL SKETCH

Author: Han Zhang

Degree: Doctor of Philosophy

Date: May 2018

Undergraduate and Graduate Education:

- Doctor of Philosophy in Applied Physics,
  New Jersey Institute of Technology, Newark, NJ, 2018

- Bachelor of Science in Physics,
  Nanjing University, Nanjing, P. R. China, 2011

Major: Applied Physics

Presentations and Publications:

H. Zhang, T. Yu, Z. Chen, C. S. Nelson, L. N. Bezmaternykh, A. M. M. Abeykoon and T. A. Tyson, "Probing Magnetostructural Correlations in Multiferroic $HoAl_3(BO_3)_4$", Physical Review B Condensed Matter and Material Physics, **92** (10), 104108 (2015).

H. Zhang, S. Liu, M. E. Scofield, S. S Wong, Xingguo Hong, V. Prakapenka, E. Greenberg and T. A. Tyson, "Structural Phase Transitions in SrTiO3 Nanoparticles", Applied Physics Letter 111 (5), 052904 (2017).

X. Qi, W. Zhong, X. Yao, H. Zhang, Q. Ding, Q. Wu, Y. Deng, C. Au, and Y. Du, "Controllable and Large-scale Synthesis of Metal-free Carbon Nanofibers and Carbon Nanocoils over Water-soluble Na_xK_y Catalysts", Carbon, **50** (2), 646 (2012).

X. Qi, Q. Ding, H. Zhang, W. Zhong, C. Au, Y. Du, "Large-scale and Controllable Synthesis of Metal-free Carbon Nanofibers and Carbon Nanotubes over Water-soluble Na_2CO_3", Material Letters, **81** (15), 135 (2012).

H. Zhang, T. Yu, H. Zhang, T. Yu, Z. Chen, C. Nelson, L. N. Bezmaternykh, Y-S. Chen, A. M. M. Abeykoon, and T. A. Tyson, "Temperature Dependent Structural

Studies of Multiferroic $RA_3(BO_3)_4$", American Physical Society March Meeting 2018, Abstract #E09.00014, Los Angeles, CA, Oral Presentation.

H. Zhang, T. A. Tyson, T. Yu, A. M. M. Abeykoon, "Temperature-Dependent Structure of $BiFeO_3$: Probing For Spin-Lattice Correlations", American Physical Society March Meeting 2016, Abstract #R30.00011, Baltimore, MD, Oral Presentation.

H. Zhang, T. Yu, Z. Chen, C. Nelson, L. N. Bezmaternykh, Y-S. Chen, A. M. M. Abeykoon, and T. A. Tyson, "Structure of Multiferroic $RAl_3(BO_3)_4$ and $RFe_3(BO_3)_4$ in the Region of High Electric Polarization", American Physical Society March Meeting 2016, Abstract #R30.00008, Baltimore, MD, Oral Presentation.

H. Zhang, T. Yu, M. Scofield, D. Bobb-Semple, J. Tao, C. Jaye, D. Fisher, S. Wong, and T. A. Tyson, "Phase Transition in Nanoscale $SrTiO_3$", American Physical Society March Meeting 2016, Abstract # C30.00005, Baltimore, MD, Oral Presentation.

H. Zhang, T. Yu, T. A. Tyson, Z. Chen, A. M. M. Abeykoon, C. Nelson, and L. N. Bezmaternykh, "A Study of the Origin of Large Magnetic Field Coupled Electric Polarization in $HoAl(BO_3)_4$", American Physical Society March Meeting 2015, Abstract #Q6.004, San Antonio, TX, Oral Presentation.

H. Zhang, T. A. Tyson, X. Hong, M. Scofield, and S. Wong, "Structural Stability of Nano-scale $SrTiO_3$ Under Pressure", American Physical Society March Meeting 2015, Abstract #B6.002, San Antonio, TX, Oral Presentation.

H. Zhang, T. Yu, T. A. Tyson, C. Nelson and L. N. Bezmaternykh, "Probing the Origin of Large Magnetic Field coupled Electric Polarization in the $RAl_3(BO_3)_4$ system", American Physical Society March Meeting 2014, Abstract #A41.00012, Denver, CO, Oral Presentation.

谨以此献给我的家人

This dissertation is dedicated to my families
that I love so much



ACKNOWLEDGMENT

I would like to express my sincere gratitude to my advisor, Dr. Trevor Tyson, for his continuous support of my Ph.D. study and research. His mentorship has helped me achieve independence and confidence. His wisdom and life experience have helped me through some of the darkest times that I have encountered.

I would like to thank my committee members, Dr. Onofrio Russo, Dr. Tao Zhou, Dr. Keun Ahn from NJIT and Dr. Zhen Wu from Rutgers University, for giving suggestions for my dissertation work. I would like to thank Dr. Roger Lalancette from Rutgers University for his advice in single crystal x-ray diffraction. I would like to thank Dr. Zhiqiang Chen, Dr. Xingguo Hong, Dr. Milinda Abeykoon, Dr. Christie Nelson from Brookhaven National Laboratory; Dr. Yu-sheng Chen, Dr. Vitali Prakapenka, Dr. Eran Greenberg from Argonne National Laboratory; and Dr. Katharine Page, Dr. Travis Williams from Oak Ridge National Laboratory, for their guidance during my time at the laboratories. I would like to give my thanks to Dr. Lenard Bezmaternykh from L. V. Kirensky Institute of Physic, Dr. Stanislaus Wong from Stony Brook University, and Dr. Dean Evans from Wright-Patterson Air Force Base, for the sample preparation. I would also like to thank the U.S. Department of Energy, the Department of Physics at NJIT, and the U.S. Air Force for providing the financial aid.

I would like to express my deep appreciation to my wife, Ms. Ye Zhou; her encouragement and support have brightened my life. I would also like to sincerely thank my parents, Ms. Fengying Wang and Mr. Xudong Zhang; their education and unconditional love have made me the person I am.

I would like to thank my dear friends: Dr. Siliang Wu, Dr. Bin Xie, Dr. Xin Chen, Dr. Haixiao Zhang and Dr. Ye Yuan for their company in my life and support in my work.

TABLE OF CONTENTS

TABLE OF CONTENTS
(Continued)

Chapter **Page**

TABLE OF CONTENTS
(Continued)

TABLE OF CONTENTS
(Continued)

Chapter **Page**

LIST OF TABLES

LIST OF FIGURES

LIST OF FIGURES
(Continued)

LIST OF FIGURES
(Continued)

LIST OF FIGURES
(Continued)

LIST OF FIGURES
(Continued)

Figure **Page**

CHAPTER 1

INTRODUCTION TO MULTIFERROICS

1.1 Ferroelectricity

1.1.1 General Concept of Ferroelectricity

Ferroelectricity [1] was first discovered in 1920 in Rochelle Salt by *Valasek* [2], it describes materials that have a spontaneous electric polarization that can be reversed by applying an external electric field. The term is analogized to ferromagnetism, in which a material exhibits a permanent magnetic moment which can be switched with the application of an external magnetic field. A typical polarization hysteresis loop is displayed in Figure 1.1.

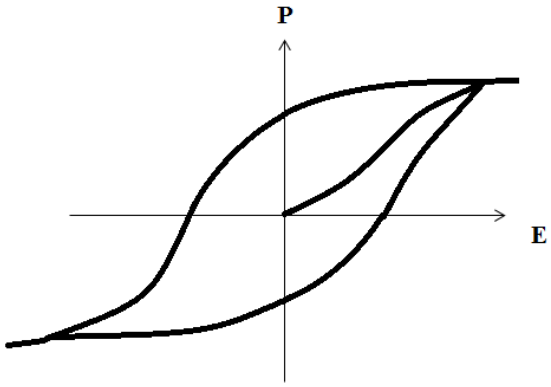

Figure 1.1 Ferroelectric hysteresis loop.

1.1.2 Proper and Improper Ferroelectrics

The ferroelectric state can be achieved by various mechanisms. A critical and necessary condition for having a polarization state in a material is the absence of a center of inversion. If a structural instability resulting in a polar state associated with the electronic pairing serves as the main driving force of the transition, such materials are called "proper" ferroelectrics [1]. Some of the well-known example materials are $BaTiO_3$ and $BiFeO_3$. In BiTaO3 there is a distinct displacement of the Ti and O ions of high symmetry positions [3]. If, on the other hand, the inversion symmetry breaking is caused by some more complex lattice distortion or if it appears as an accidental by-product of some other ordering, for example, charge ordering, the ferroelectricity is called "improper". Table 1.1 is a list of some well-known proper and improper ferroelectrics. More Details will be discussed in the next few sections.

Table 1.1 Classification of Ferroelectrics

	Mechanism of Symmetry Breaking	**Materials**
Proper	Covalent Bonding between $3d^0$ transition metal and oxygen	$BaTiO_3$
	Polarization of $6s^2$ lone pair of Bi or Pb	$BiMnO_3$, $BiFeO_3$, $Pb(Fe_{2/3}W_{1/3})O_3$
Improper	Structural transition	hexagonal $RMnO_3$
	Charge ordering	$LuFe_2O_4$
	Magnetic ordering	Orthorhombic $RMnO_3$, RMn_2O_5, $CoCr_2O_4$

Source: [1(f)]

1.2 (Anti)Ferromagnetism

Unpaired electrons on atoms inside a material give rise to the existence of magnetic dipole moments. The effect that the unpaired magnetic dipole moments tend to align in parallel to an external magnetic field is called paramagnetism. Under some circumstances, if a material exhibits a net magnetic polarization without the existence of an external magnetic field, this material is called ferromagnetic. If the moments of the aligned and anti-aligned ions of a material balance completely, then it is called antiferromagnetic, a schematic graph is shown in Figure 1.2.

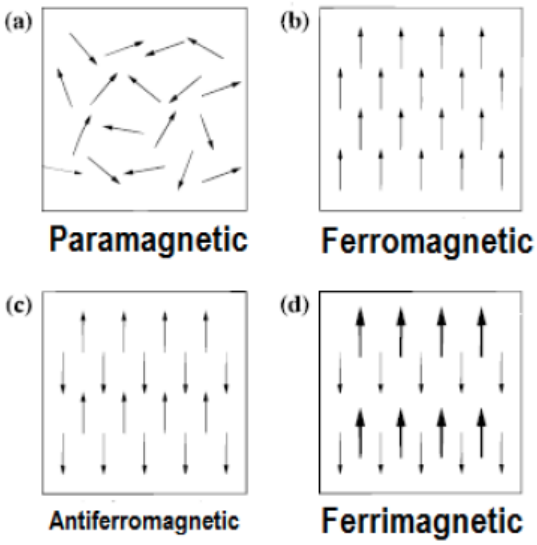

Figure 1.2 Schematic diagram of different kinds of magnetism.
Source: [4]

1.3 Magnetoelectric Effect (ME)

The term “Magnetoelectric effect” is used to describe the coupling between electric and magnetic parameters, in which the electric (magnetic) polarization can be induced or modified by applying an external magnetic (electric) field. The correlation between these

parameters can be either linear or non-linear, depending on the specific driving mechanism. The effect was first observed by *Röntgen* in 1888, with a moving dielectric in a magnetic field generating a polarization [5]. Later in 1894, *Curie* proposed the possibility of an intrinsic magnetoelectric effect in some crystals [6], but it was not until 1926 that *Debye* first used the phrase "magnetoelectric effect" to describe such kind of phenomenon [7]. More Details of ME effect can be found in these recent reviews [8].

1.4 Review of Multiferroics

1.4.1 General Discussion of Multiferroics

The term 'multiferroic' was first defined by *Schmid* [9] in the late 20th century, to describe those materials that possess two or more of the so-called 'ferroic' properties: ferroelectricity, ferromagnetism, and ferroelasticity. As shown in Figure 1.3

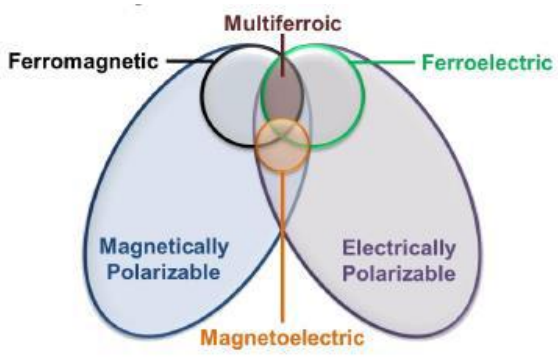

Figure 1.3 Multiferroic materials.
Source: [8(e)]

However, the current trend is to exclude the requirement for ferroelasticity in practice. Therefore, the word ‘multiferroic’ today often refers to the materials in which ferromagnetism and ferroelectricity coexist, and it can also be called “ME multiferroics” or “magnetic ferroelectrics”.

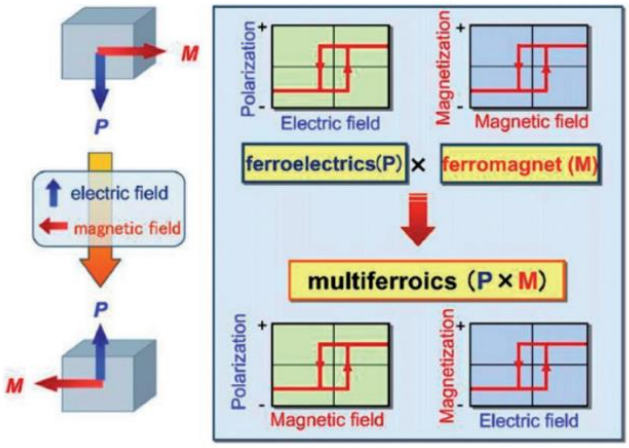

Figure 1.4 Diagram of “ME multiferroics” [1(d)], ferroelectricity and ferromagnetism coexist in the same system, while the electrical parameters and magnetic parameters can be tuned by modifying the other.
Source: [1(d)]

Multiferroic materials may exhibit unusual physical properties because of the coupling between their magnetic and electric order parameters, which in turn have a very promising future in multiple applications. Figure 1.5 shows the phase control for ferroics and multiferroics [10].

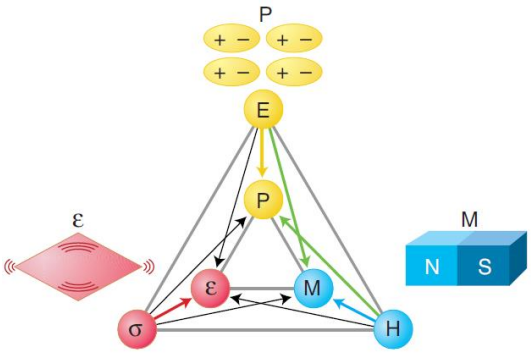

Figure 1.5 The electric field *E*, magnetic field *H*, and stress ϭ control the electric polarization *P*, magnetization *M*, and strain Ɛ, respectively. The coupling between these parameters allows the mutual control of each other.
Source: [10]

1.4.2 Incompatibility of Ferroelectricity and Magnetism.

As promising as it may sound for the properties of multiferroics, the coexistence of ferroelectricity and magnetism is usually rare. From a structural perspective, a multiferroic system requires the simultaneous breaking of both the spatial-inversion and time-reversal symmetry, which narrows down to only 13 out of 233 Shubnikov magnetic point group. Meanwhile, from the point of view of microscopic mechanisms, most ferroelectrics are transition metal oxides that possess empty d shells, while magnetism, on the other hand, usually requires transition metals with partially filled d shells - the difference in filling of the *d* shells required for ferroelectricity and magnetism makes these two ordered states mutually exclusive [1(c),1(e), 8(f)].

Still, there are a handful of materials that appear to be multiferroics, but the presence of electric and magnetic dipoles does not necessarily mean strong coupling between the two. As a contrast, the coexisting magnetic and ferroelectric order parameters are usually weakly coupled, given the mechanisms of ferroelectricity and magnetism are quite different and often do not strongly interfere with each other. The

following section will be focusing on the mechanisms of different types of multiferroics to obtain a comprehensive picture of multiferroic materials.

1.4.3 Approaches to the Coexistence of Ferroelectricity and Magnetism.

Multiferroics form a very diverse class of materials, and even today there is no universal "theory of multiferroics" that can describe them completely (See reviews in Ref. [1] and [8]) To obtain a comprehensive picture of multiferroics requires detailed theoretical analysis and measurements on a broad class of specific systems. Multiferroics can be divided into two classes. In one class, the coexisting magnetic and ferroelectric order parameters are weakly coupled, with the onset of ferroelectricity occurring independently of the appearance of magnetic ordering. In the other class of multiferroics, the magnetic ordering breaks the inversion symmetry and results in a polar state which supports ferroelectricity. Ferroelectricity can also be induced by charge ordering in multiferroics [11]. This coupling between magnetization and polarization typically occurs in systems with low net polarization (typically < ~1 $\mu C/cm^2$). We note that the polarization value in most multiferroics is small compared to the classic ferroelectric systems such as $BaTiO_3$ ($P \sim 75\ \mu C/cm^2$) [12].

In the search for materials with larger magnetoelectric couplings, compounds including $Ni_3V_2O_8$ [13], $MnWO_4$ [14], $LiCu_2O_2$ [15], $CuFeO_2$ [16], $CoCr_2O_4$ [17] and other systems such as $Ba(Ti_{0.9}Fe_{0.1})O_{2.81}$[18], $NdCrTiO_5$ [19], ferrites [20] and manganites [21] were examined.

In one type of multiferroic materials, the ferroelectricity is induced by lone pair electrons, such as $BiFeO_3$. $BiFeO_3$ has received intense investigation because it is one of the few multiferroics with both ferroelectricity and magnetism occurring above room

temperature; possibly enabling real devices (see reviews in Ref. [1]). In this system, Bi^{3+} ions with two electrons in the 6s orbit (lone pair) shift away from the centrosymmetric positions with respect to the surrounding oxygen ions, leading to ferroelectricity. But because the ferroelectric and magnetic (Fe^{3+} in this case) units are different, the coupling between them is weak. Other similar systems are like $BiMnO_3$, $Pb(Fe_{2/3}W_{1/3})O_3$.

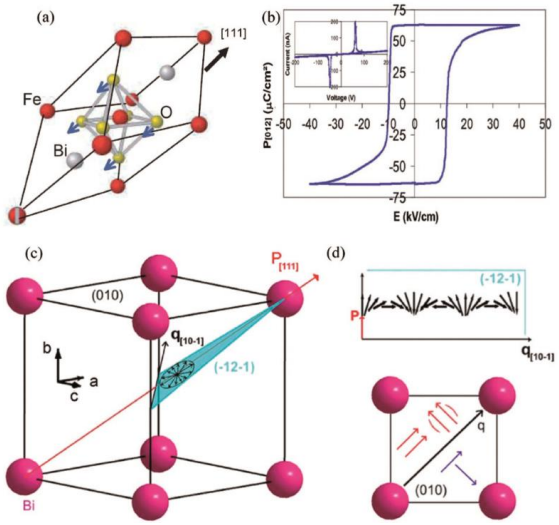

Figure 1.6 (a) Lattice structure of $BiFeO_3$, (b) Measured P-E loop of $BiFeO_3$, (c) spontaneous polarization P is along the [111] direction, and the spiral magnet propagation defined by the wave vector q. (d) Polarization in the (101) plane.
Source: [1(d)]

Another type of multiferroics of interest is the one that ferroelectricity is associated with a structural transition. A typical example is the hexagonal rare earth manganites $RMnO_3$ [21(c)], such as $YMnO_3$. In the $YMnO_3$ system, the appearance of an electric dipole moment is found below the temperature of a lattice transition. The dipole moment is believed to be contributed by the nonlinear coupling to nonpolar lattice distortions. The shift of atomic positions from a centrosymmetric phase in ferroelectric $YMnO_3$ is indicated in Figure 1.7.

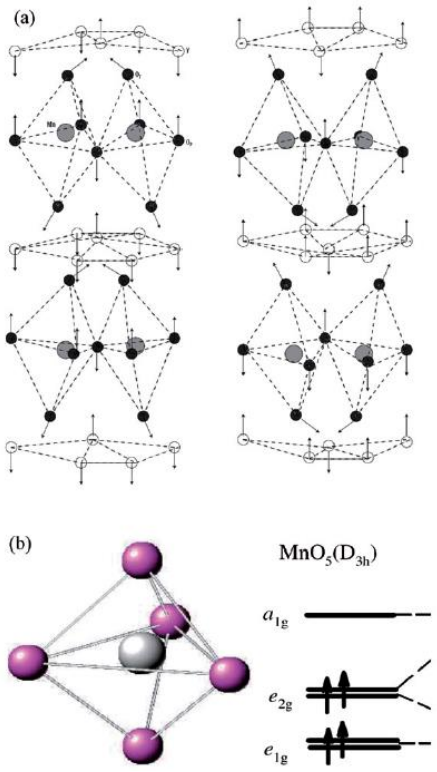

Figure 1.7 (a) Lattice structure of ferroelectric $YMnO_3$, the arrows indicate the shift of atoms from centrosymmetric positions. (b) the electron configuration of Mn ions.
Source: [1(d)]

The most recent interest in multiferroics was reignited by the discovery of high magnetic tuneability of electric polarization and a dielectric constant in the class of materials known as 'frustrated magnets'. In the first type of such system, ferroelectricity is induced by magnetic spirals or other nontrivial magnetic ordering. For example, the rare earth manganites $TbMnO_3$ [21(d)], in which ferroelectricity is induced by the formation of a symmetry-lowering magnetic ground state that lacks inversion symmetry. The resulting polarization is small (~ 0.08 $\mu C/cm^2$), but because it is caused directly by the magnetic ordering, a possible new magnetoelectric interaction should be expected. The second type of system is one with exchange striction without magnetic spirals. For instance, orthorhombic RMn_2O_5 [21(e)] (R = Tb, Dy, and Ho) was also found to exhibit

significant magneto-dielectric effects near a unique commensurate-incommensurate magnetic transition where magnetic transitions are intricately coupled with changes in the dielectric properties. Details of the mechanism behind this system are more complicated. One can refer to ref. [1(f)] for further information. Tables of Multiferroic materials with spiral spin order been investigated (Ref. [1(d)]) are presented below.

Another interesting system is the magnetic oxide Ni_3TeO_6 [22]. Studies show this system exhibits no signature of ferroelectricity (no spontaneous polarization seen in zero magnetic field) down to 10 K (in zero magnetic field) but undergoes a single magnetic transition at 52 K, below which the system is antiferromagnetic. Recently, it was reported that this material exhibits nonhysteretic magnetoelectric switching in the presence of the c direction magnetic fields. As another example, the $LuFe_2O_4$ [23] system is found to support ferroelectricity which comes from the combination of two factors: crystal structure as well as the frustrated charge ordering resulting from ordered Fe^{2+} and Fe^{3+} sites. Figure 1.8 is a sketch of the charge ordering in the $LuFe_2O_4$ system.

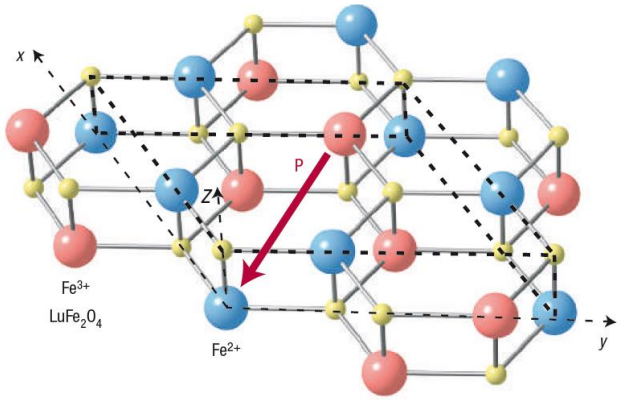

Figure 1.8 Charge ordering in the bilayered $LuFe_2O_4$ system. The charge transfer from top to bottom layer gives rise to a net electric polarization.
Source: [1(f)]

There is also a special compound family to be mentioned, which is the polar crystals with a strong interaction of the magnetic order parameter and the electrical polarization, such as $LiFeP_2O_7$ [24]. The coupling of the magnetic order parameter with the existing polarization makes it an interesting material to study.

The systems discussed above all possess different kinds of structures, and hence the physical properties, the mechanism behind the coupling of their electrical and magnetic parameters are unique to each specific system. This makes it evident that that structural information is essential, on the atomic level (spin coupling) up the micron level (domain formation). Hence, detailed structural studies will be coupled with magnetic and other bulk measurements on these materials. The following tables of multiferroic systems were taken from ref [1(d)].

Table 1.2 A List of Multiferroics Excluding Those Ferroelectricity Induced by Spiral Spin Order

Compound	Crystal Structure	Magnetic ions	Mechanism for multiferroics	Ferroelectric Polarization ($\mu C/cm^{-2}$)	Ferroelectric transition temperature(K)	Magnetic transition temperature(K)
$RFe_3(BO_3)_4$	R32	R^{3+}, Fe^{3+}	Ferroelectric-active BO3 group	~9	~38	~37
$Pb(B_{1/2}B'_{1/2})O_3$ B=Fe,Mn,Ni,Co;B'=Nb,W,Ta	Pm3m	B'	B ions Ferroelectricity, B' ions magnetism	~65	~385	~143
$BiFeO_3$	R3c	Fe^{3+}	Lone pair at A-site	~75	~1103	~643
$BiMnO_3$	C2	Mn^{3+}	Lone pair at A-site	~20	~800	~100
$(Y,Yb)MnO_3$	$P6_3cm$	Mn^{3+}	Geometric	~6	~950	~77
$HoMnO_3$	$P6_3cm$	Mn^{3+}	Geometric	~5.6	~875	~76 (Mn^{3+}), ~5 (Ho^{3+})
$InMnO_3$	$P6_3cm$	Mn^{3+}	Geometric	~2	~500	~50
$YCrO_3$	P21	Cr^{3+}	Geometric	~2	~475	~140
$Pr_{1-x}Ca_xMnO_3$	Pnma	Mn^{3+}, Mn^{4+}	Site and bond centered charge-order	~4.4	~230	~230
$LuFe_2O_4$	$R\bar{3}m$	Fe^{2+}, Fe^{3+}	Charge frustration	~26	~330	~330
$Ca_3Co_{2-x}Mn_xO_7$	R3c	Co^{2+}, Mn^{4+}	Charge ordered state plus magnetostriction	~90	~16.5	~16
RMn_2O_5	Pbam	Mn^{3+}, Mn^{4+}	Charge ordered state plus magnetostriction	~40	~38	T_N=43, T_{CM}=33
$DyFeO_3$	Pbnm	Fe^{3+}, Dy^{3+}	Magnetostriction between adjacent antiferromagnetic Dy and Fe ions	~0.4	~3.5	T_N(Dy)~3.5 T_N(Fe)~645

Source: [1(d)]

Table 1.3 A List of Multiferroics with Spiral Spin-order Induced Ferroelectricity

Compound	**Crystal Structure**	**Magnetic ions**	**Spiral spin wave vector *q***	**Ferroelectric temperature (K)**	**Spontaneous polarization ($\mu C/cm^{-2}$)**
$LiCu_2O_2$	Pnma	Cu^{2+}	(0.5,0.174,0)	<23	4
$LiCuVO_4$	Pnma	Cu^{2+}	(0,0.53,0)	<3	20
$Ni_3V_2O_8$	Mmm	Ni^{2+}	(0.28,0,0)	3.9-6.3	100
$RbFe(MoO_4)_2$	$P\bar{3}m1$	Fe^{3+}	(1/3,1/3,0.458)	<3.8	5.5
$CuCrO_2$, $AgCrO_2$	$R\bar{3}m$	Cr^{3+}	(1/3,1/3,0)	<24	
$NaCrO_2$, $LiCrO_2$	$R\bar{3}m$	Cr^{3+}	(1/3,1/3,0), (-2/3,1/3,1/2)	<60	Antiferroelectric
$CuFeO_2$	$R\bar{3}m$	Fe^{3+}	(b,b,0), b=0.2-0.25	<11	300
$RMnO_3$	Pbnm	Mn^{3+}	(0,k,1), k=0.2-0.39	<28	500
$CoCr_2O_4$	M3m	Cr^{3+}	(b,b,0), B=0.63	<26	2
$AMSi_2O_6$, A=Na,Li, M=Fe,Cr	C2/c	Cr^{3+}, Fe^{3+}		<6	14
$MnWO_4$	Pc/2	Mn^{2+}	(-0.21,0.5,0.46)	7-12.5	55
CuO	C2/c	Cu^{2+}	(0.506,0,-0.843)	213-230	150
$(Ba,Sr)_2Zn_2Fe_{12}O_{22}$	Rhombohedral Y	Fe^{3+}	(0,0,3d),0<d<1/2	<325	150
$Ba_2Mg_2Fe_{12}O_{12}$	Rhombohedral Y	Fe^{3+}	//[001]	<195	80
$ZnCr_2Se_4$	Cubic Spinel	Cr^{3+}	(b,0,0)	<20	
Cr_2BeO_4	Orthorhombic	Cr^{3+}	(0,0,b)	<28	

Source: [1(d)]

1.5 Applications of Multiferroics

In terms of applications, the most direct use for multiferroics is as magnetic field sensors utilizing the sensitivity of the electric polarization to magnetic fields [1(d),4, 25]; a schematic diagram is shown in Figure 1.9.

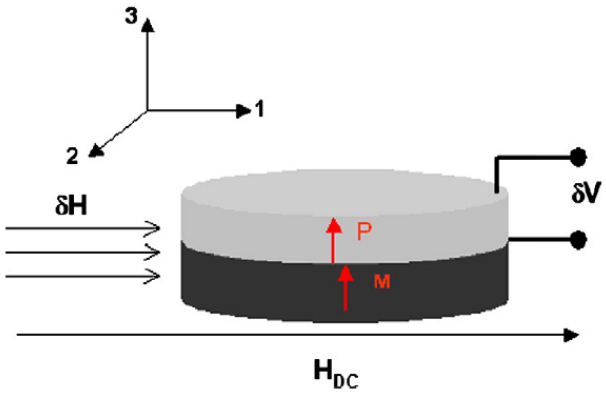

Figure 1.9 Schematic diagram of a magnetic field sensor.
Source: [25]

Meanwhile, since multiferroics provide alternative ways to read and write data using both electric polarization and magnetization, as well as the mutual control between them, multiferroics have a huge potential in data storage and memory devices [26]. Figure 1.10 presents a sketch of an eight-logic memory cell [27]. The information stored by the magnetization (blue horizontal arrow) and polarization (red vertical arrow) directions of the multiferroic layer (MF1) and the ferromagnetic layer (FM2) in (*a*) and of the MF1 layer and the MF2 layer in (*b*). It was read by the resistance of the magnetic trilayer (R), written into MF1 by an applied external field and written into FM2 in (*a*) or MF2 in (*b*) by applying a voltage across the MF2 in the layer.

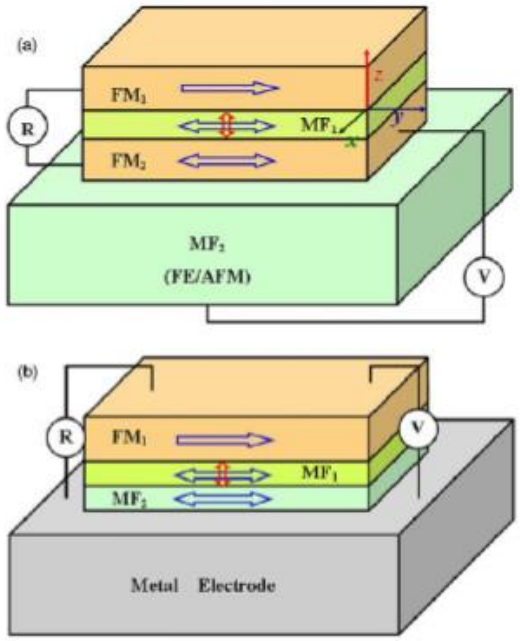

Figure 1.10 Schematic design of the proposed eight-logic memory cell.
Source: [27]

Current industries favor the FeRAM devices despite the disadvantage of a destructive read operation since MRAMs are much slower and less power efficient during read/write operations. The availability of multiferroic materials with strong coupling between different ordered states will enable data storage systems with multiple components, and devices which can operate while using considerably less power than current devices. Figure 1.11 (a) presents a sketch of an ME read-head sensor and Figure 1.11 (b) shows a possible MERAM device, binary information is stored by the magnetization direction (thick white arrows) of the bottom ferromagnetic layer (blue), is read by the resistance of the magnetic trilayer (*R*p when the magnetizations of the two ferromagnetic layers are parallel), and is written by applying a voltage (*V*) across the multiferroic ferroelectric–antiferromagnetic layer (FE-AFM; green) [28].

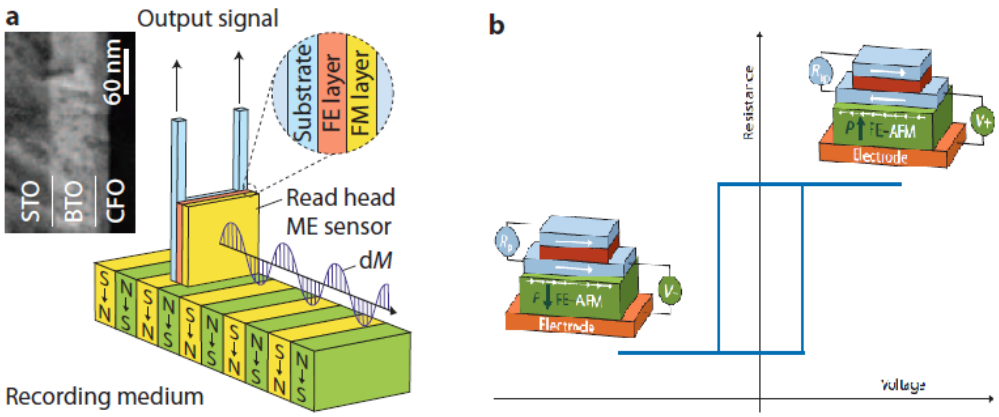

Figure 1.11 (a) Sketch of an ME read-head sensor, (inset) a transmission electron microscopy image of the CFO/BTO heterostructure grown on a single-crystal STO substrate. (b) Sketch of a possible MERAM element.
Source: [28]

Other applications such as gate dielectrics for semiconductor devices [29] and piezoelectric transformers [30] were reported as well. Systematic experimental work has been conducted by many groups to enable these possible applications [31].

1.6 Rare Earth Boron Oxide $RA_3(BO_3)_4$

One of the recently examined classes of multiferroic compounds is rare earth iron borates, $RFe_3(BO_3)_4$ (R = rare earth, Y). These systems have attracted considerable attention mainly due to the non-centrosymmetric geometry (see Figure 1.12) and large magnetoelectric effects (with value of electric polarization of order ~ 1 $\mu C/cm^2$), such as $GdFe_3(BO_3)_4$ [32], $DyFe_3(BO_3)_4$ [33], $HoFe_3(BO_3)_4$ [34] $YFe_3(BO_3)_4$ [32(b)], $NdFe_3(BO_3)_4$ [35] and $PrFe_3(BO_3)_4$ [36].

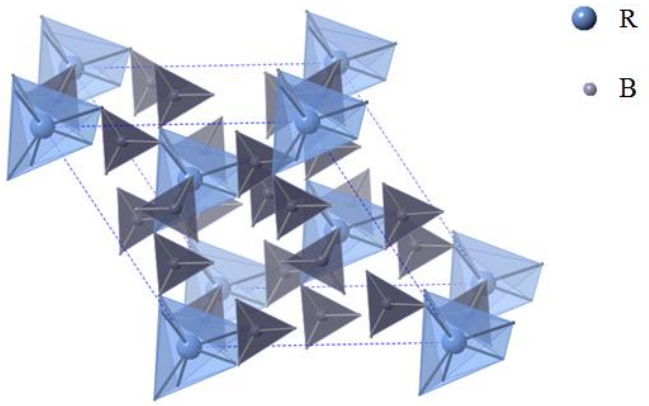

Figure 1.12 Crystal structure of $RA_3(BO_3)_4$.

Many interesting properties of this compound family have been discovered in recent years. For example, the study of $EuFe_3(BO_3)_4$ reveals the appearance of new phonon modes below 58 K [37] and changes in the phonon frequencies *vs.* temperature plot near T_N giving evidence of spin-phonon coupling. The onset of the new phonon modes is argued to coincide with a structural transition from the R32 to the $P3_121$ space groups on cooling. The appearance of new phonon modes is also reported in $PrFe_3(BO_3)_4$ at ~ 30 K [36]. This system is reported to have a strong coupling between the phonon and crystal-field excitations with coupling constant W ~ 15 cm^{-1}. Meanwhile, studies have shown that the phonon frequencies change only weakly in $RFe_3(BO_3)_4$ for different R ions at room temperature [38]. We note that the $RFe_3(BO_3)_4$ system exhibit complex magnetic structure due to the presence of the magnetic R (4f) and Fe (3d) sites. The first magnetic transition (due to Fe ordering) occurs near ~40 K. In the case for R = Ho and Gd, spin reorientation of the Fe moments in the a-b plane occurs at lower temperatures (~ 10 K for for Ge and ~5 K for Ho), due to strong coupling between spins on the R and Fe sites [32(b), 34(c), 34(f)]. It has been found that the polarization along the a and c axes

are related to the magnetic field induced ordering at the Fe and Ho sites, respectively. The nature and range of the magnetic correlations are not well understood. This behavior is not observed in the R = Y, Er [39], and Tb systems [40].

Recent reports show that the transition metal Fe is not essential to establish large magnetoelectricity in this class of materials [41]. This suggests that a study of the properties of the isostructural compound $RAl_3(BO_3)_4$ (RABO) with only 4f electrons on the R site driving the magnetism, would be quite useful to determine the basic physics behind the borate systems. First-principles calculation on $TbAl_3(BO_3)_4$ [42] revealed that this class of material has a very promising potential in magneto-optical usage. An experimental study of the $TmAl_3(BO_3)_4$ [41] system has reported magnetoelectric polarization changes in the a and c directions reach values up to 0.03 $\mu C/cm^2$ at 7 T with the applied magnetic field along the a axis. The magnetoelectric polarization is found to be proportional to the lattice contraction in a magnetic field. The results of this investigation clearly prove the existence of a significant coupling between the rare-earth magnetic moment and the lattice in $RAl_3(BO_3)_4$ although the atomic level description is not clear. It is possible that external pressure may alter the polarization of these materials.

More recently a giant magnetoelectric effect of P = 0.36 $\mu C/cm^2$ was found in $HoAl_3(BO_3)_4$ [43] along x-axis when a 7 T magnetic field is applied along the y-axis. The magnetoelectric effect in the $HoAl_3(BO_3)_4$ system increased with decreasing magnetic anisotropy. This phenomenon is considered quite interesting because the value discovered is significantly higher than the reported values for other multiferroic

compounds (for example $TbMnO_3$ with P = 0.08 μC/cm^2, $GdMn_2O_5$ with P = 0.12 μC/cm^2).

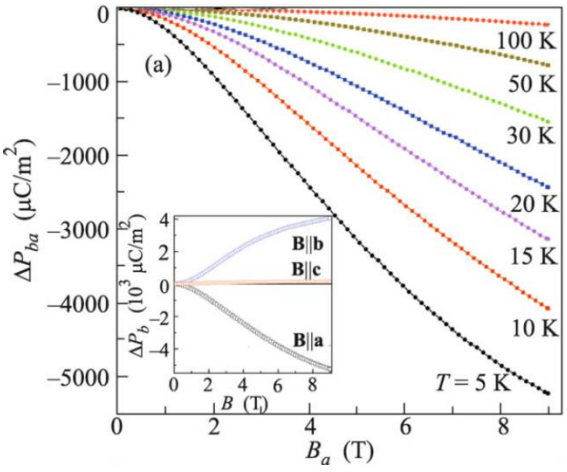

Figure 1.13 Electric polarization of HABO measured along b axis when applying an external magnetic field along the a axis. [43]
Source: [43]

Meanwhile, although the measurement of magnetic susceptibility, magnetization, and polarization of the $RAl_3(BO_3)_4$ system have been conducted by other groups so far, the atomic level origin of magnetoelectric effect in the $HoAl_3(BO_3)_4$ system is still not yet understood. Microscopic models [44] of the $HoAl_3(BO_3)_4$ system have been developed and make definite predictions of the mechanism driving the ferroelectric coupling to polarization. A magnetostriction based mechanism involving distortion of the HoO_6 polyhedra with the applied magnetic field was proposed. Chapters 4 and 5 will be focused on the intensive study that has been conducted with the $RA_3(BO_3)_4$ system.

CHAPTER 2

SIZE DEPENDENT BEHAVIOR OF FERROELECTRICS

2.1 Size Dependence of the Phase Transition in Nanocrystals: General Discussion

Phase stability of nanostructures has been one of the central issues in material science which have attracted considerable interest in recent years [45]. For a given sample which processes, for example, a temperature dependent phase transition, the transition occurs when the temperature reaches a critical value T_C. Generally, the T_C of a nanoparticle drops with decreasing particle size because of the lowered cohesive energy of the under-coordinated surface atoms and the size-dependent portion of surface atoms relative to the entire specimen [46]. T_C elevation by reducing the solid size happened to nanoclusters consisting of III-A and IV-A elements. The T_C depression and elevation can also be called undercooling or overheating as well. In a bulk specimen, the phase transition is usually considered to be linked with external conditions such as temperature or pressure, and such transition can be described well with classical theory. However, at the nanometer regime, the introduction of the new degree of the freedom, the particle size (or surface to volume ratio), makes it possible to tune the phase transition of the material. Such phenomenon is not limited to some specific crystal structures but over a wide range of chemical systems. Some of the recent examples are $BiFeO_3$ [47], $BaTiO_3$ [48], Cu_2S [49], Fe_2O_3 [50], PbS [51], TiO_2 [52].

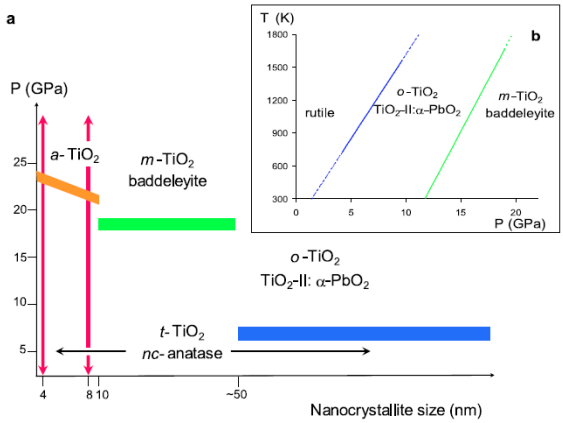

Figure 2.1 TiO_2 Phase Diagrams. (a) Size-dependent phase stability of TiO_2, (b) phase diagram of bulk TiO_2.
Source: [52]

The size dependence of phase stability involves both static and kinetic components, which goes beyond the scope of the classical theory. Furthermore, all the detectable properties such as the Debye temperature, the specific heat, etc. are no longer constant but can be affected by the particle size [53].

Despite the importance of the size-dependent transition of materials, the microscopic mechanisms of it are still unclear for many of the systems under study. For systems where the "static" part plays the major role in the size-dependent transition, such behavior can usually be modeled and calculated in quite good agreement with experimental results, one of the examples is the well-known $SrTiO_3$ thin film [54]. However, when it comes to the kinetic contribution analysis becomes more complicated because of the inhomogeneous kinetic effect in the nanometer regime. Theories are also being developed to try to explain the possible kinetic mechanism. For example, the bond-order-length-strength (BOLS) correlation mechanism to the pressure domain has led to an analytical expression for the correlation between the critical pressure and the particle size and their effect on the phase stability [45(a)].

2.2 $SrTiO_3$ Perovskites

Perovskites form a particularly interesting class of materials because even slight modifications of the crystal structure can lead to drastic changes in physical properties, such as superconductivity, ferroelectricity, and ferromagnetism. Strontium titanate, $SrTiO_3$ (STO), is generally considered to be a model perovskite and plays an important role in the understanding of soft-mode-driven phase transitions, which have been extensively studied for more than five decades.

$SrTiO_3$ is known as an incipient ferroelectric material, with the pure form remaining paraelectric down to temperatures of ~0 K. Small perturbations of the structure, such as but not limited to isotope substitution [55], Ca doping [56], the application of electric fields [57], and/or stress [58], can result in the onset of a ferroelectric state at finite temperatures. For example, isotopic substitution with ^{18}O yields evidence of a ferroelectric transition temperature with T_c ~ 23 K. The largest enhancement of T_c was first reported by Haeni *et al.* When applying tensile strain in STO epitaxial films, a ferroelectric transition can be observed above room temperature [59], as is indicated in Figure 2.2.

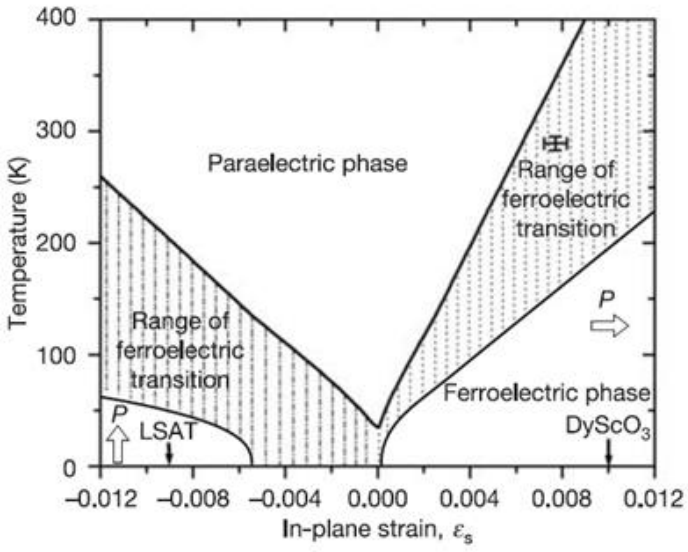

Figure 2.2 Variation in T_c of $SrTiO_3$ with biaxial in-plane strain, reported by *Haeni, et al*. *Source: [59]*

It has also been reported that the phase transition behavior and domain structure in anisotropically-strained STO thin films differ significantly as compared with isotopically-strained films [60]. In the asymmetrically-strained STO system, the anisotropy of properties along two different directions is observed in measurements of switchable polarization, relaxor character, and permittivity. According to a study conducted by Jang *et al*., the role of strain is to stabilize longer range correlations of pre-existing nanopolar regions (PNRs) [61], related to the unintentional Sr deficiency.

The bulk STO system is cubic under ambient conditions. However, the oxygen atoms located in the octahedral sites can easily rotate around the central titanium atom, thereby giving rise to possible distortions of the perfect crystal [62], as shown in Figure 2.3. An antiferrodistortive (AFD) transition to a non-polar tetragonal phase occurs at ~ 105 K at ambient pressure. This temperature-induced phase transition has been

intensively examined over decades [63], both experimentally and theoretically, with a soft phonon mode model proposed to describe the observed transition.

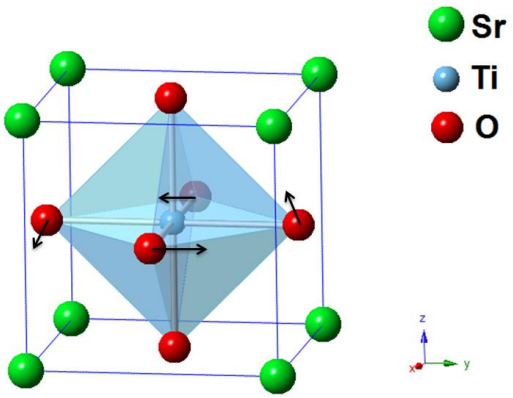

Figure 2.3 Crystal structure of $SrTiO_3$.

The AFD transition of the STO system can also be affected by applying pressure. In earlier experimental work on bulk samples, no sign of any anomaly in the elastic constants was observed between 0.4 to 2.2 GPa [64]. The transition temperature was found to have shifted linearly with increasing pressure below 0.85 GPa, and then altered nonlinearly above that pressure [65]. Later, evidence of the AFD transition induced by pressure was observed through a combination of experiments including Brillouin scattering (BS) [66], high-pressure Raman measurements [67], and X-ray absorption fine structure (XAFS) spectroscopy [68]. Although the pressure associated with the onset of the transition differed with each independent experimental method, the pressure values previously investigated fell within a range of 5.5 – 7.5 GPa. A theory explaining the phase transition within the STO system was also developed using *ab initio* density functional theory (DFT) methods, which predicted a transition near 6 GPa [69]. However, more recent experimental work has tended to favor a higher pressure for the detection of

such a phase transition. Guennou*et al*. [70] utilized single crystal X-ray diffraction (XRD) and Raman spectroscopy methods to report a transition pressure of 9.6 GPa, a finding which is also further supported by several recent works [71].

2.3 Nano-scale Perovskites

Studies of simple nanoscale perovskites have been conducted, with the aim of utilizing them in device applications for high-density storage. For example, the ferroelectric behavior of $BaTiO_3$ nanoparticles (see Ref. [3]) has been shown to disappear if the particle size is below a critical size of 5–10 nm. Meanwhile, in the STO system, lattice expansion [72] and nano-size effects [73] have been observed with reduced particle size. The increase in unit cell volume is well established in the literature for many metal oxides and has been observed in studies of small particles of $BaTiO_3$ [74]. This contrasts with metals such as gold, where the cell parameters shrink as their size is diminished. The experimental results of the lattice expansion in $BaTiO_3$ is shown in Figure 2.4.

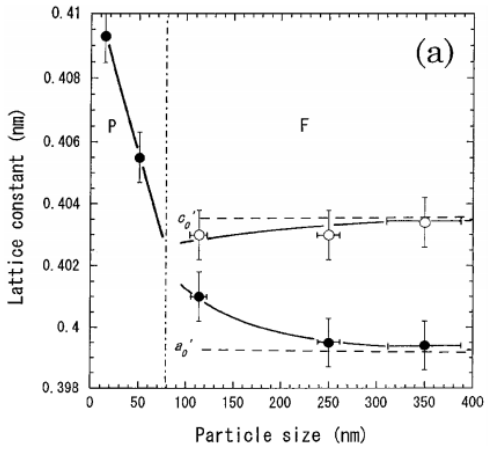

Figure 2.4 Lattice constant vs. particle size in $BaTiO_3$.
Source: [74]

The most consistent explanation for such a volume expansion in small oxide particles is the effect of truncation on the attractive Madelung potential that holds the oxide lattice together. The transition temperature of several perovskites from the classical paraelectric to the quantum paraelectric state has been reported to increase with decreasing particle size, which contrasts with the typical trend expected between transition temperature and size effects. For example, the classical paraelectric to classical ferroelectric phase transition found in $BaTiO_3$ and $PbTiO_3$ samples experienced a decrease in transition temperature with a corresponding decrease in particle size [75].

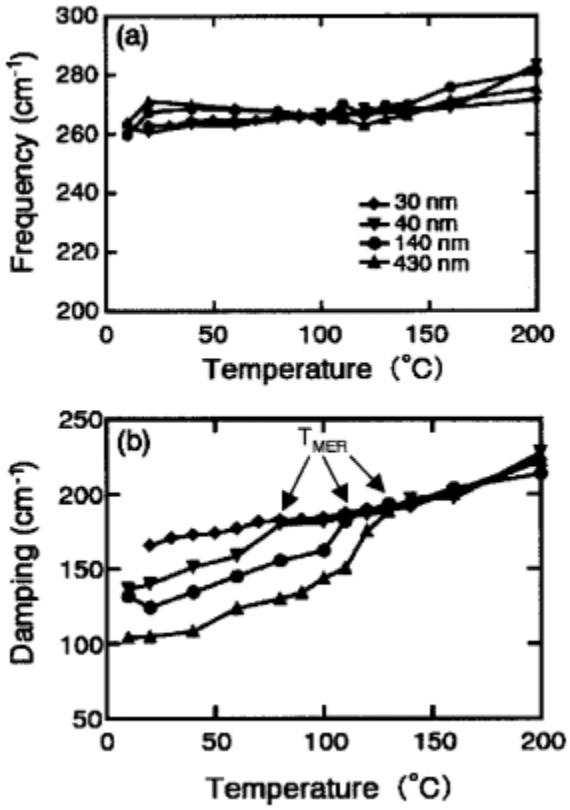

Figure 2.5 Temperature dependence of (a) resonance frequency and (b) damping factor for $BaTiO_3$ fine particles.
Source: [75]

Recently, interesting results are reported when mechanically grinding the $BaTiO_3$ bulk sample down to nano-size particles [76]. These results show that the 10nm $BaTiO_3$ nanoparticle, prepared by 25 hours of mechanical grinding in oleic acid as a surfactant, is ferroelectric. The nanoparticles have an electric polarization several times larger than it in the bulk $BaTiO_3$. This is considered to be quite astonishing, but the microscopic picture behind it is still yet to be revealed.

In our recent work conducted on various sizes of STO nanoparticles, a polar state over a wide temperature range (possibly with ferroelectric properties) was found in free-standing 10 nm nanoparticles [77].

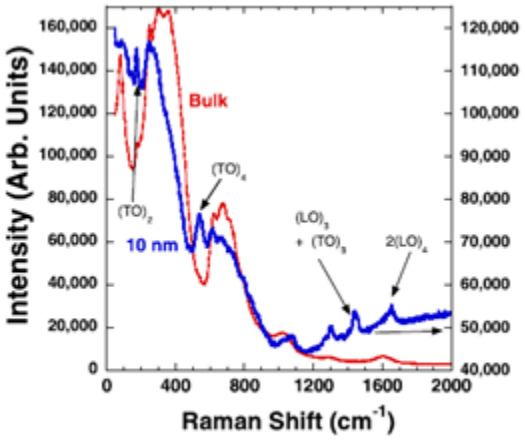

Figure 2.6 Detected polar modes in 10 nm $SrTiO_3$ nanoparticles.
Source: [77]

More recently, a scaled reduction of STO thin films was found to have produced ferroelectricity [54], which is shown in Figure 2.7.

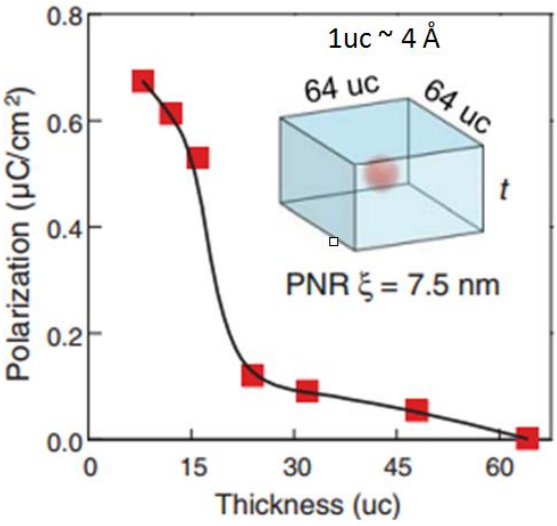

Figure 2.7 Simulations by *D. Lee et al.* [54] on polarization by size reduction in $SrTiO_3$ thin films.
Source: [54]

We note that while a large body of research has previously been conducted on STO films, very limited studies on ferroelectricity and the polar state of STO nanoparticles have been carried out. Nanoscale STO can potentially possess unique properties that are not exhibited by either bulk or film systems. It is very likely that nano-size STO particles will perform differently as compared with bulk samples upon varying reaction conditions.

CHAPTER 3

CHARACTERIZATION AND COMPUTATIONAL METHODS

The multiferroics that have been investigated were synthesized by various of methods. Details of the sample preparations will be covered in the following chapters. The specific heat behavior was examined with a Physics Property Measurement System (PPMS). The structures of the samples were explored with synchrotron radiation sources and neutron sources using multiple methods. Computations were conducted with Density Functional Theory (DFT) calculation. This chapter will be focused on the discussion of the characterization and computational methods mentioned above.

3.1 Introduction to X-rays and Neutron Scattering

X-rays are a term named by the German scientist Wilhelm Röntgen after their discovery in 1895 [78]. It is a form of electromagnetic radiation which consists of photons with energies ranging from 100 eV to 100 keV. By contrast, the neutrons are a type of particles that constitute the nuclei of atoms together with protons. The mass of a neutron is similar to that a proton. However, unlike the protons which are positively charged, the neutrons have no net electric charge. However, they carry an intrinsic spin and can probe magnetic order. Typical energy for the neutron is from 0.1 MeV to 500 MeV. Both the x-rays and the neutron have particle-like as well as wave-like properties. Table 3.1 displays some of them.

Table 3.1 Properties of X-ray and Neutron

	X-rays	**Neutron**
Rest Mass	0	1.675×10^{-27} kg
Charge	0	0
Spin	1	1/2
Magnetic Moment	0	$-1.913\ \mu_N$*

*Nuclear Magneton $\mu_N=5.051\times10^{-27}$ J/T

The x-rays and neutron scattering are very powerful tools that can be used to understand the properties of unknown matters, as their wavelengths λ are both very similar to interatomic spacing. They can be used to 'see' the structure of matters. Note that the structural information provided by the scattering techniques are statistically averaged (over some length scale characteristic of the method) rather than real-space pictures of particular instances. Meanwhile, given the difference in their nature, x-rays and neutrons interact with matters in very different ways: the x-rays interact with electrons via an electromagnetic interaction; while neutrons interact with atomic nuclei via very short-range force, as well as with unpaired electrons via the magnetic dipole moment.

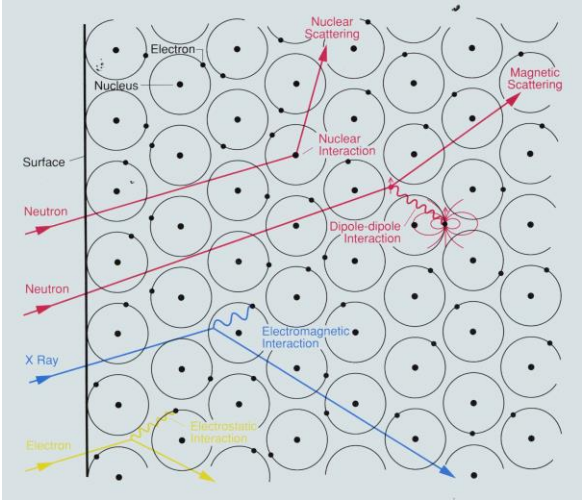

Figure 3.1 Interaction mechanism of x-rays and neutrons.
Source: R. Pinn, 'An introduction to x-ray and neutron scattering', the 17th National School of Neutron and X-ray, 2015.

Table 3.2 is a list of the (dis)advantages of both techniques:

Table 3.2 Comparison of X-rays and Neutron Techniques

	X-rays	**Neutrons**
Advantages	High brilliance x-ray sources	Penetrate bulk matter
		Strong contrast possible
	No kinematic restrictions	Energy similar to that of elementary excitations
	No restriction on energy transfer that can be studied	Scatter strongly by magnetic fields
		Data interpretation is direct
Disadvantages	Strong absorption of low energy photons	Low brilliance of neutron sources
	Low contrast for atoms with smaller Z	Some elements absorb neutrons strongly
	Radiation damage to samples	Kinematic restrictions on Q for large energy transfers
	Magnetic scattering usually not easy to observe	Provides statistical averages rather than real space pictures

3.2 Synchrotron Radiation (SR)

Synchrotron Radiation [79], by definition, is the radiation from charged particles, usually electrons, traveling in circular orbits at relativistic speeds. Unlike laboratory x-ray sources, which x-rays are usually generated in the x-ray tubes, synchrotron radiation sources are of significant advantages in many aspects, which include (1) high brightness and intensity, Figure 3.2 below shows the synchrotron source compared to the laboratory source (x-ray tubes); (2) high level polarization and excellent collimation; (3) Tunability in a wide range of energy ; (4) Various sample environments including extreme conditions like low temperature (~ 2K) or high pressure (hundreds of GPa). The use of SR sources is wildly applied to different areas of science.

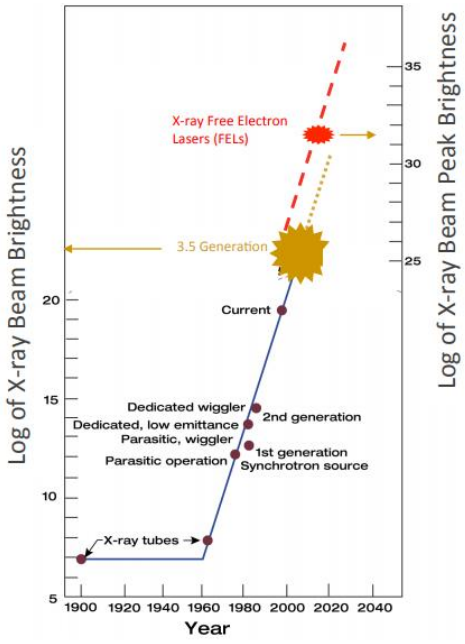

Figure 3.2 Brightness of different x-ray sources.
Source: D. Mills, 'Synchrotron Radiations: Production & Properties', 18th National School of Neutron and X-rays scattering, 2016

3.3 Neutron Sources

The generation of neutrons is more difficult than it of x-rays and is typically associated with more problems such as radiation shielding. Currently, there are two major types of high flux neutron sources: continuous and pulsed.

For the continuous source, the neutrons are generated by a nuclear reactor through a chain reaction. One of the largest facilities with a continuous neutron source in the world is the High Flux Isotope Reactor (HFIR) at Oak Ridge National Laboratory (ORNL). A schematic diagram is like Figure 3.3 below:

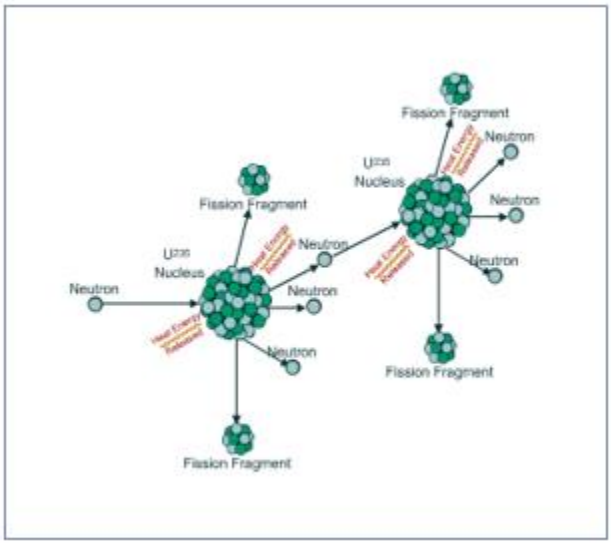

Figure 3.3 Schematic diagram of a continuous neutron source.
Source: D. Mills, 'Synchrotron Radiations: Production & Properties', 18th National School of Neutron and X-rays scattering, 2016.

The number of neutrons generated is ~10^{15} n/s. In the pulsed source (also known as spallation source), neutrons are generated by striking the target (e.g., Mercury) with pulses of high-energy protons. The peak flux from the spallation source is usually higher than a continuous source by a factor of ~10. One such facility is the Spallation Neutron Source (SNS) at ORNL.

3.4 Single Crystal X-ray and Neutron Diffraction

3.4.1 Theoretical Background

A Crystal is a three-dimensional repeating array of atoms or molecules; many materials are in the form of crystals, such as ice, table salt, diamond and so on. A single crystal (or monocrystalline) is a material in which the crystal lattice of the entire sample is continuous and unbroken with no grain boundaries. The smallest volume unit of highest symmetry which, when translated in 3-Dimension will generate the crystal (like blocks making up a wall), is called the unit cell of a crystal. The structural information of the unit cell is an identifying feature for a specific crystal. The determination of unit cell structure is usually achieved by x-ray and neutron diffraction.

In the case of an incident beam diffracted by a crystal, one defines the wavevector for the incident and outgoing beam to be $\boldsymbol{k}_i$, $\boldsymbol{k}_f$, respectively. The momentum transfer **Q** is defined as:

$$\boldsymbol{Q} = \boldsymbol{k}_f - \boldsymbol{k}_i, |\boldsymbol{Q}| = 4\pi \sin\theta / \lambda \tag{3.1}$$

The scattering intensity S(**Q**), defined as

$$S(\boldsymbol{Q}) = \frac{1}{N}\sum e^{-i\boldsymbol{Q}(\boldsymbol{R}_i - \boldsymbol{R}_j)} \tag{3.2}$$

with $\boldsymbol{R}_i = \boldsymbol{i} + \boldsymbol{u}_i$, where $\boldsymbol{i}$ is the equilibrium position of atom i, and $\boldsymbol{u}_i$ is any displacement from the equilibrium position. For S(**Q**) to become non-zero, it must satisfy

$$\boldsymbol{Q}(\boldsymbol{i}-\boldsymbol{j}) = 2M\pi \ (M = 0,1,2,3 \ldots) \tag{3.3}$$

Which leads to:

$$\boldsymbol{Q} = \boldsymbol{G}_{hkl} = h\boldsymbol{a}_1^* + k\boldsymbol{a}_2^* + l\boldsymbol{a}_3^* \tag{3.4}$$

The vectors $\boldsymbol{a}_1^*$, $\boldsymbol{a}_2^*$, $\boldsymbol{a}_3^*$ are defined as

$$\boldsymbol{a}_1^* = \frac{2\pi}{V_0}\boldsymbol{a}_2 \times \boldsymbol{a}_3 \ , \ \boldsymbol{a}_2^* = \frac{2\pi}{V_0}\boldsymbol{a}_3 \times \boldsymbol{a}_1 \ , \boldsymbol{a}_3^* = \frac{2\pi}{V_0}\boldsymbol{a}_1 \times \boldsymbol{a}_2 \ , \tag{3.5}$$

Where $\boldsymbol{a}_1$, $\boldsymbol{a}_2$, $\boldsymbol{a}_3$ are the primitive translation vectors of the unit cell. The vector $\boldsymbol{G}_{hkl}$ here is called the reciprocal lattice vector, and the lattice it defines is called the reciprocal lattice, h,k and l, are called Miller indices. The set of reciprocal vectors $\boldsymbol{G}_{hkl}$ determine the possible reflections in the diffraction. For a single crystal diffraction, reflections can only be reinforced in specific directions governed by the Bragg's law:

$$n\lambda = 2dsin(\Theta), n = 1,2,3 \ldots \tag{3.6}$$

Where d is the separation of a set of scattering planes perpendicular to $\boldsymbol{G}_{hkl}$.

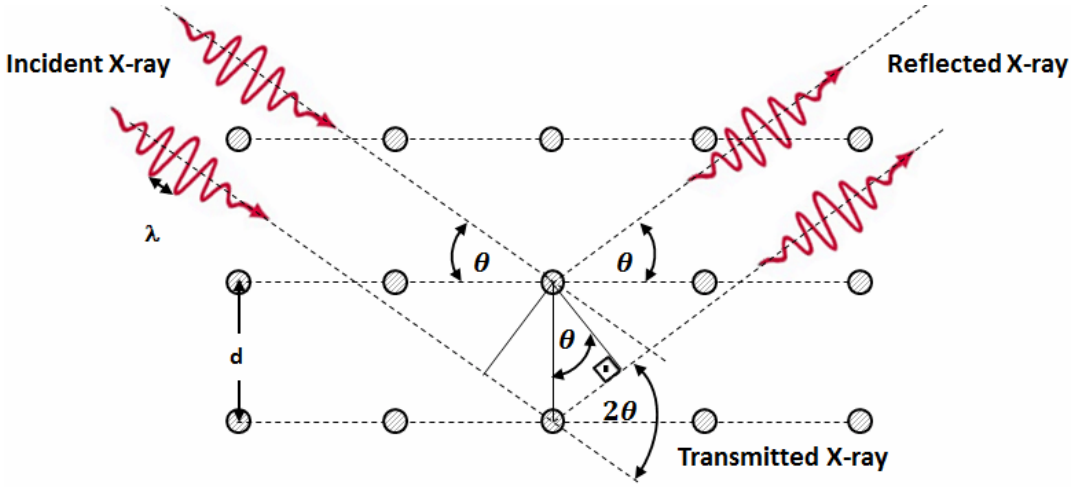

Figure 3.4 The schematic diagram of Bragg's law.

The intensity of the reflections can be calculated by [80]

$$I_{hkl} = I_0 \left(\frac{e^2}{m^2 c^4} \right) \frac{1 + cos^2\theta}{2} \frac{\lambda^3}{16\pi R^2 sin^2\theta cos\theta} \frac{|F_{hkl}|^2}{V_0^2} D \cdot \Delta V \cdot j \qquad (3.7)$$

Where I_0 is the intensity of the incident beam, D is a thermal factor, $\Delta V$is the volume of sample in diffraction and j is the multiplicity factor. F_{hkl} is called the (unit–cell) structure factor, which is, in essence, the resultant of N waves scattered in the direction of the reflection [hkl] by the N atoms in the unit cell. Note that the intensity of a reflection is proportional to $|F|^2$, not F, which means direct Fourier inversion of diffraction data to yield crystal structures is not possible — because the phase is unknown. It is called the well-known 'Phase Problem'. Therefore, to get the comprehensive picture of crystal structure, models must be used to fit to the data.

The idea of single crystal x-ray (and neutron) diffraction experiment is to collect crystal a complete set of reflections (out to a certain Qmax) and then try to find the model

that best fit to the data. The general steps of a diffraction experiment are like the ones in Figure 3.5.

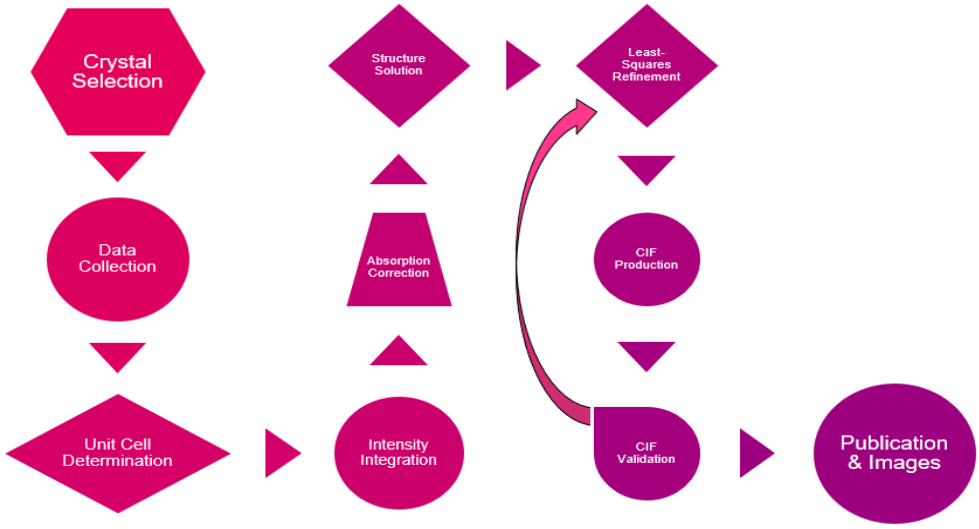

Figure 3.5 Structure determination from a single crystal diffraction experiment.
Source: C. Beavers, 'Single Crystal Diffraction: The Definitive Structural Technique', 17th National School of Neutron and X-ray Scattering, 2015.

3.4.2 Data Collection

The single crystal diffractometer should be able to collect the diffraction patterns, which consist of Three-dimensional (3-D) array of spots. Figure 3.6 is an example of a typical x-ray diffractometer:

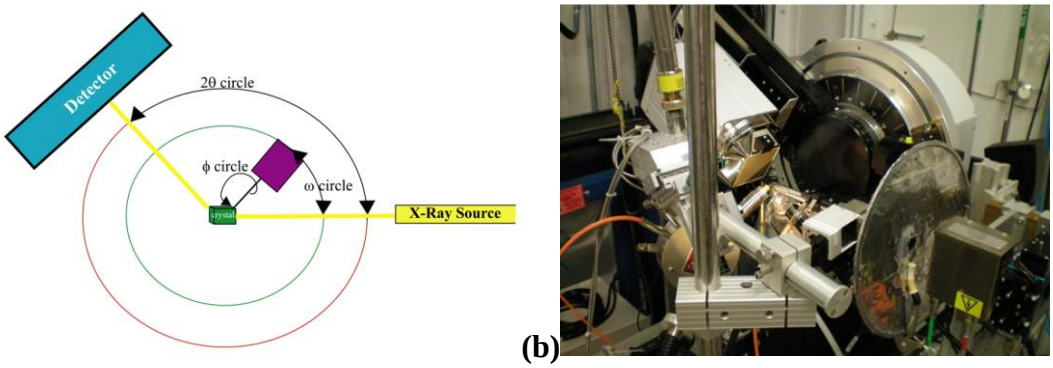

Figure 3.6 (a) schematic diagram of an x-ray diffractometer (b) The diffractometer at beamline 15-ID-B, Advanced Photon Source (APS), Argonne National Laboratory (ANL).

Three rotation angles combined with the Two-Dimensional (2-D) detector makes it easy to measure the entire crystal diffraction pattern.

As for the neutron diffractometer, limited by the neutron generation and detection technology, it is of difficult to design a spectrometer as the ones used in x-rays. Figure 3.7 shows the triple-axis spectrometer for neutron diffraction at station HB-1, HFIR, ORNL. The three axes can move freely in a limited range and make it possible to collect a portion of the entire diffraction pattern.

(a)

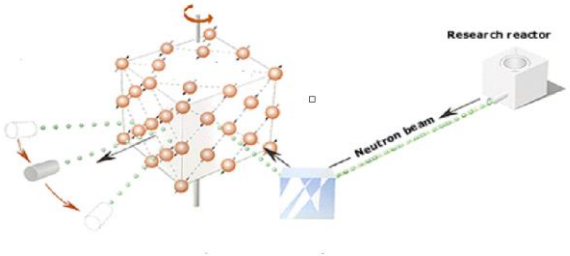

(b)

Figure 3.7 (a) Schematic diagram of a triple-axis neutron spectrometer. (b) Beamline HB-1 at HFIR, ORNL.

3.4.3 Structure Determination

3.4.3.1 Indexing. Indexing can also be referred as unit cell determination. There are multiple methods, but all strive for the same goal- to determine the unit cell dimensions and how the unit cell axes are defined in diffractometer coordinates. The matrix that relates the unit cell to the diffractometer is called the orientation matrix and will be used later in indexing. The process is roughly universal- reflections are collected as projected

from reciprocal space, where common vector directions are determined. The reciprocal space unit vectors are determined which are related to the real space unit cell lengths. After the unit cell is determined, the lattice type can be determined, and the unit cell can be refined, using the positions of the reflections.

(a) **(b)**

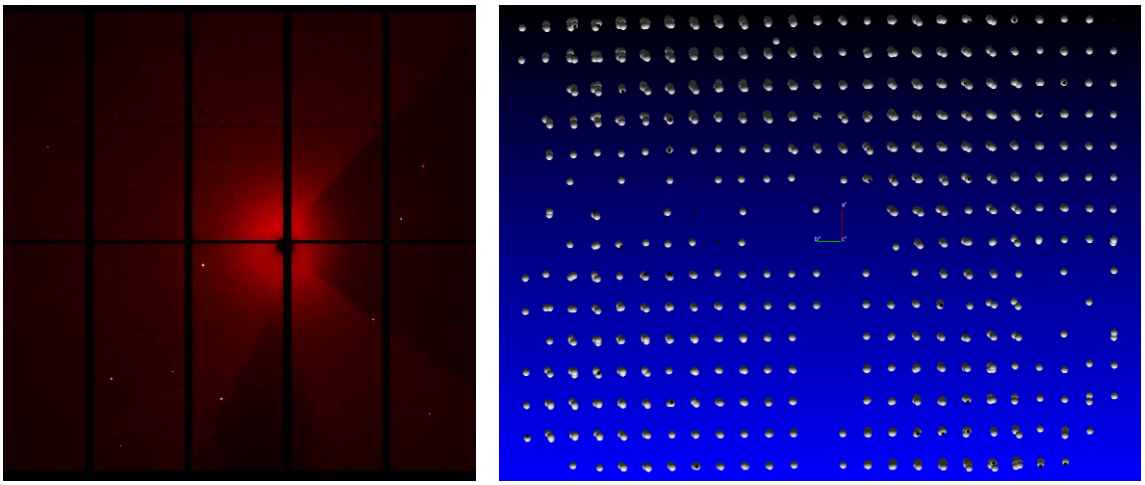

Figure 3.8 Indexing process of the $GdFe_3(BO_3)_4$ system. (a) One out of 1440 images collected from the diffractometer. (b)Representation of the reflections in reciprocal space.

3.4.3.2 Data Integration. Data integration is used to determine the number of x-rays responsible for each diffracted spot. The orientation matrix is used to determine where reflections should be, and the mosaicity of the crystal is calculated by measuring the angular spread of the reflections. The output of the integration is a list of reflections, usually with directional cosines and other information about their location in the data set.

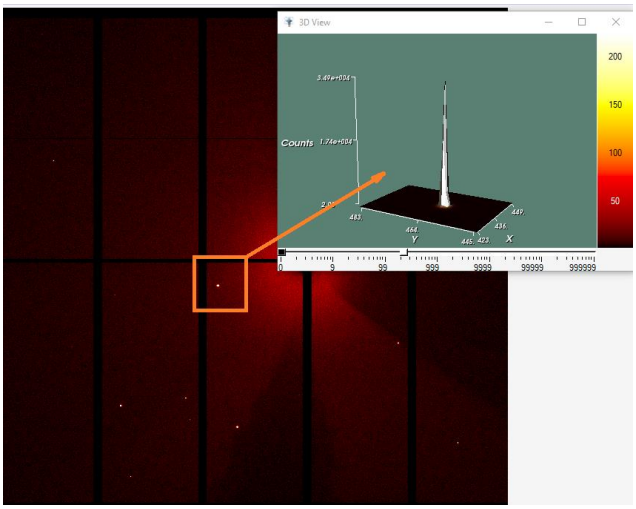

Figure 3.9 Three-Dimensional view of the selected reflection from the diffraction pattern of $GdFe_3(BO_3)_4$.

3.4.3.3 Absorption Correction. Since very few crystals are perfectly spherical, and fewer still match the size of the beam, a correction for the scattering volume for each image is needed.

3.4.3.4 Space Group Determination. This step uses systematic absences and symmetry of reciprocal lattices to determine crystal symmetry.

3.4.3.5 Structure Solution. The step to finding the correct structure solution is usually a very complicated procedure. In general, the Fourier synthesis for electron density from diffracted reflections is:

$$\rho_{xyz} = \frac{1}{V}\sum_{hkl} \bar{F}_{hkl} e^{-i2\pi(hx+ky+lz)} \tag{3.8}$$

Where F_{hkl} is the structure factor as mentioned in the previous section, and the intensity of the reflections is proportional to F^2 — but the phase is unknow. Modern structure

solution programs take the list of reflections from previous steps and find reflections that are related, then use probabilistic methods [81] to build a set of phases that produce reasonable (non-negative) electron density maps.

However, the initial set of phases are often still far from a complete solution. To obtain the correct structure, one (usually) must conduct an iterative process of refinement and validation. Figure 3.10 shows a standard procedure of such process.

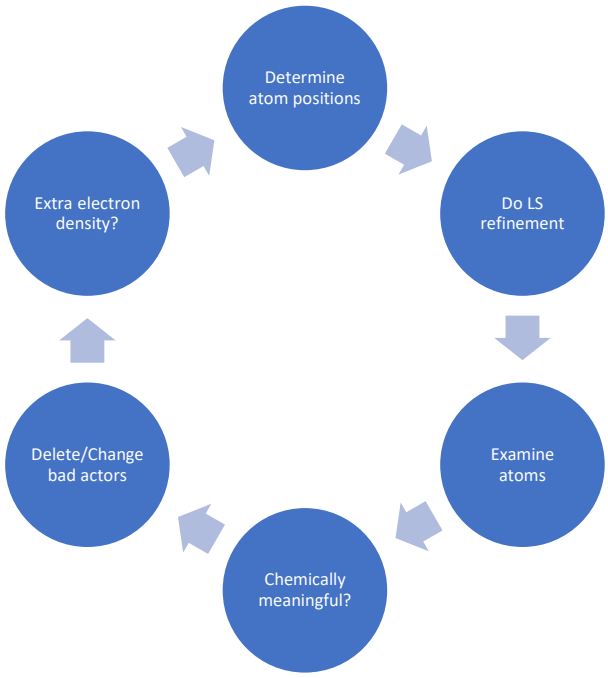

Figure 3.10 A procedure of refinement and validation for finding the structure solution.
Source: C. Beavers, 'Single Crystal Diffraction: The Definitive Structural Technique', 17th National School of Neutron and X-ray Scattering, 2015.

The structure solution result needs to be inspected carefully for chemical meaningfulness, such as but not limited to: do the bond distances make sense chemically? Are the atomic displacement parameters meaningful in size and shape? Are the peaks in difference charge density between the model and data? The refinement process usually makes it clear which electron density peaks are false- either the refined position or the

displacement ellipsoid becomes poorly defined. As the model evolves, the R-values, or the goodness of fit (GOF), which are commonly quoted measures of how well the model agrees with the data, should become smaller and smaller and then stabilize, as the model aligns with the data.

$$R_1 = \frac{\sum \left| |F_O| - |F_C| \right|}{\sum |F_O|} \tag{3.9}$$

$$wR_2 = \sqrt{\frac{\sum \omega (F_O^2 - F_C^2)^2}{\sum \omega (F_O^2)^2}} \tag{3.10}$$

$$GOF = \sqrt{\frac{\sum \omega (F_O^2 - F_C^2)^2}{N_R - N_P}} \tag{3.11}$$

In the above equations, F_O is the observed (experimental) data, F_C is the calculated (theoretical) data, ω is the weighting, N_R is the number of independent reflections and N_P is the number of refined parameters. While the R-values usually approach smaller values when the solution gets closer to the correct crystal structure in each of the individual refinement, in general there is, no standard for how good these values must be for a 'correct solution' [82]. The fact that a refinement result makes good sense both physically and chemically is still one of the most important things in determining the correct structure solutions.

3.5 High-Pressure X-ray Diffraction with Powder Samples

3.5.1 Powder Diffraction

Powder – or polycrystalline mass, is a form of the sample that contains all possible orientations of crystallites. In a powder diffraction experiment, while all physics principles for single crystal diffraction still hold, single crystal reciprocal lattice becomes smeared into spherical shells. (Care must be taken so that the grains are small enough to produce full rings with no sharp Bragg peaks.) As a result, diffraction pattern becomes cones (see Figure 3.11(a)) in 3-D space and displays as concentric rings (see Figure 3.11(b)) on a 2-D detector. All the spots on the same ring are diffracted by the scattering plane with the same Miller Indices (only the crystal orientation is different), therefore have the same d_{hkl} value, and the Bragg's law still holds.

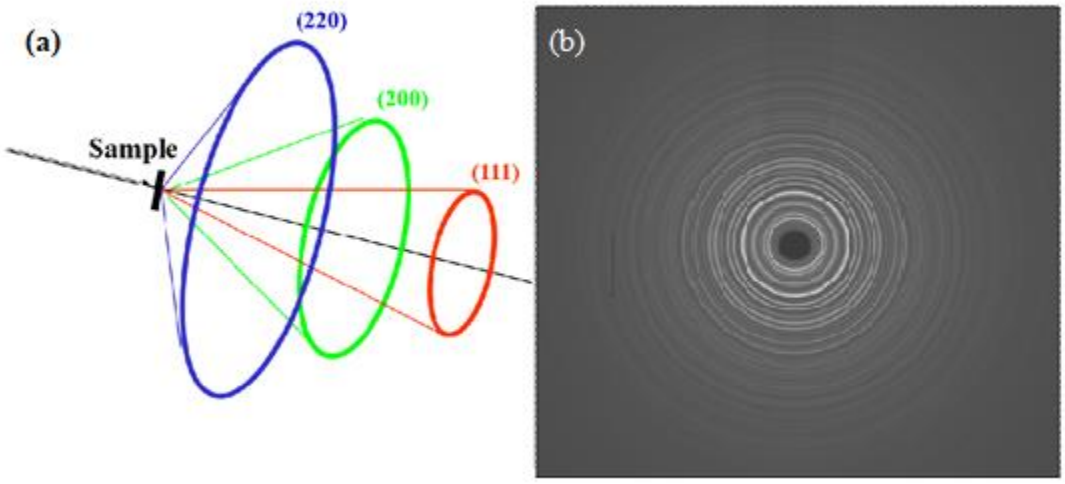

Figure 3.11 (a) Schematic diagram of powder diffraction in 3-D space. (b) Powder diffraction image taken by a 2-D detector with $HoAl_3(BO_3)_4$

3.5.2 Diamond Anvil Cell (DAC)

The Diamond Anvil Cell (DAC) has been used to obtain high-pressure sample environment since the 1950s [83], the early literature called it 'a diamond bomb' because of the extremely high pressure it can generate (can be above 300 GPa). Figure 3.12 and 3.13 are the schematic diagrams of DACs used in this work. Note that the DAC technology has been developing for decades that there're many types of DACs, commercial or homemade, adapted to a variety of research areas nowadays. However, their working mechanism is similar.

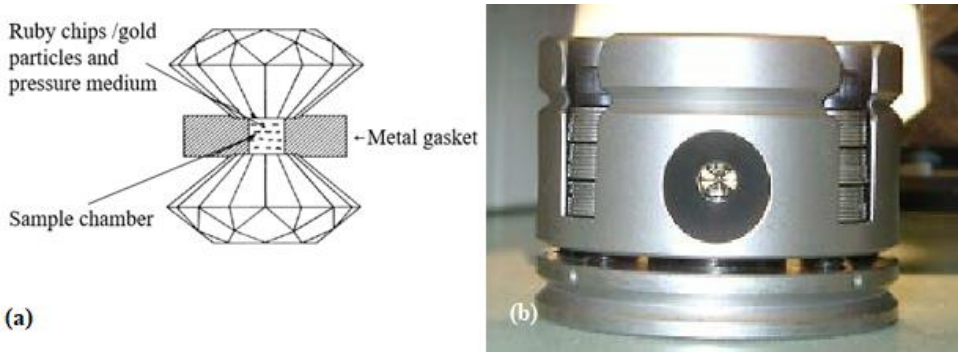

Figure 3.12 (a) Schematic diagram of a DAC (b) the screw-driven DAC used in this work

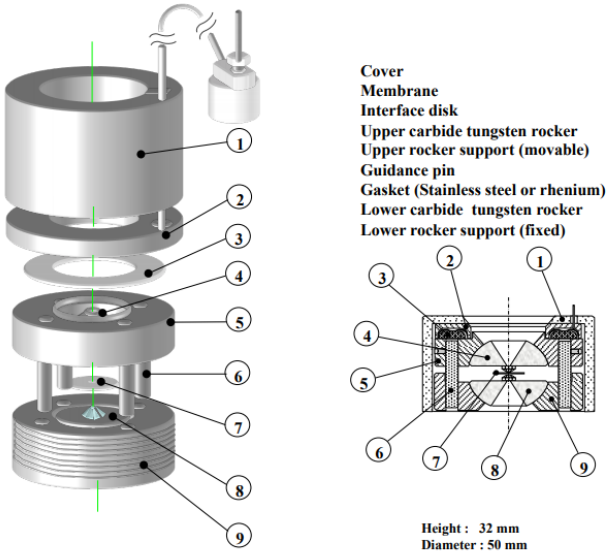

Figure 3.13 Schematic diagram of a gas-driven membrane DAC used in this work
Source: H. Liu, 'High-Pressure Applications', 17th National School of Neutron and X-ray Scattering, 2015.

The DACs, as shown in the above two graphs, contains two identically cut diamonds of gem quality, the tips being fattened to culets, with a diameter depending on the highest pressure one DAC is designed to reach. Typical culet sizes for DACs used in a synchrotron source are like 300 μm and 500 μm. Each diamond is mounted on a metallic support. For a DAC to reach higher pressure, the pair of the diamond needs to be aligned perfectly (parallel culets) [84].

In a high-pressure measurement, a piece of metal called a gasket (e.g., steel, tungsten) needs to be inserted between the pair of diamonds [85]. The diamonds will first be driven towards each other (usually by screws) to compress the gasket to create a pit at the center with typically ~50 μm as the thickness. A hole with proper size (depends on the pressure limit the DAC wants to reach) will then be drilled at the center of the pit to serve as the sample chamber. To ensure higher pressure limit, the sample chamber needs to be right at the center.

Samples will then be put into the chamber created as mentioned above, along with small ruby chips and/or gold particles to calibrate the pressure during measurements. The chamber will then be filled with pressure transmission medium, such as Methanol ethanol-water mixture; He gas; Ne gas and so on [86]. Each medium has its advantages, and the choice of the medium needs to be optimized based on the details of the individual experiment. The pressure medium used is chosen to ensure that the measurements are in the hydrostatic limit for the chosen pressure range.

After the sample and DAC been properly prepared, one can increase the pressure inside the sample chamber by driving the diamonds towards each other (typically with

clamps or screws). The reading of the current pressure can be acquired by measuring the ruby fluorescence lines [87], or by measuring the diffraction pattern of the gold particles.

3.6 Pair Distribution Function (PDF)

As the science and technology evolves, an increasing number of materials that are under study for their interesting properties are highly complex. They consist of multiple elements, have large unit cells and/or low dimensions, and many have incommensurate structures. Examples are like, but not limited to, (1) non-crystalline materials; (2) disordered materials; (3) nanostructures. For these types of materials, traditional crystallographic approach to structure determination is insufficient or even fails. Figure 3.14 is a demonstration of such a circumstance:

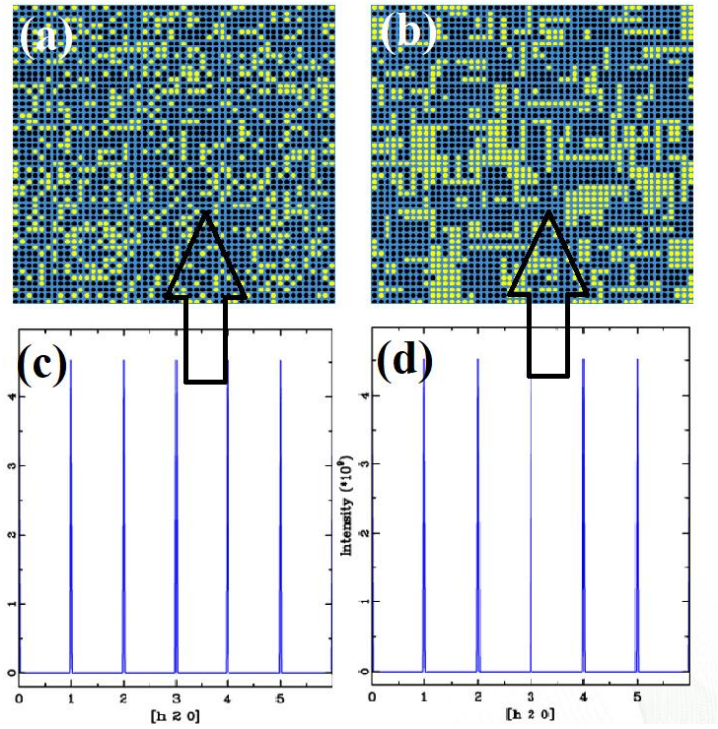

Figure 3.14 (a) (b) Cross section for a model crystal consisting of 70% black atoms and 30% vacancies, the overall averaged structure for (a) and (b) are the same, but local ordering is different. (c)(d) Bragg scattering of the two samples yields to identical patterns.
Source: T. Proffen, 'PDF Analysis', 18th National School of Neutron and X-ray Scattering, 2016.

In the above Figure, traditional crystallographic analysis such as Bragg scattering tells no difference between the two specimens in Figure 3.14 (a) and (b), while the properties of these crystals might totally depend on vacancy ordering. Another good example is with nanoparticles – in which case the lack of long-range order makes the very concept of a crystal invalid. To find a solution for such complexity, one needs to go beyond the Bragg equation and conventional crystallographic analysis.

The Pair Distribution Function (PDF) has been developed to address the problems as described above. Details can be found in a variety of books [88]. The PDF method uses the 'total scattering' approach which treats both the Bragg and diffuse scattering on an equal basis [88(b)]. Powder measurement of the sample are conducted to get the

coherent scattering function $I(Q)$ (intensity *vs.* the magnitude of the scattering vector Q), and is normalized by the incident flux per atom in the sample to yield to the total-scattering structure function $S(Q)$, note that $S(Q)$ is just a traditional powder diffraction pattern corrected for extrinsic contributions to the background intensity (e.g., Compton scattering) and properly normalized.

After the total-scattering function $S(Q)$ has been acquired, instead of trying to build a model to fit the data directly in reciprocal-space, as the traditional crystallographic approaches would normally do. A Fourier transform into real-space is done. But prior to this step, it is essential to point out that, to get a good resolution in real-space, the $S(Q)$ must be measured over a wide and high range of Q-values, a typical Q-value for excellent real-space resolution is Qmax~30-50 $Å^{-1}$. It is significantly higher than the Q-limit for laboratory x-ray sources (e.g., ~8 $Å^{-1}$ for a copper-K_α x-ray tube). Therefore, synchrotron radiation beamlines with short wavelengths are preferred to obtain high resolution in PDF analysis. Figure 3.15 illustrates this idea below:

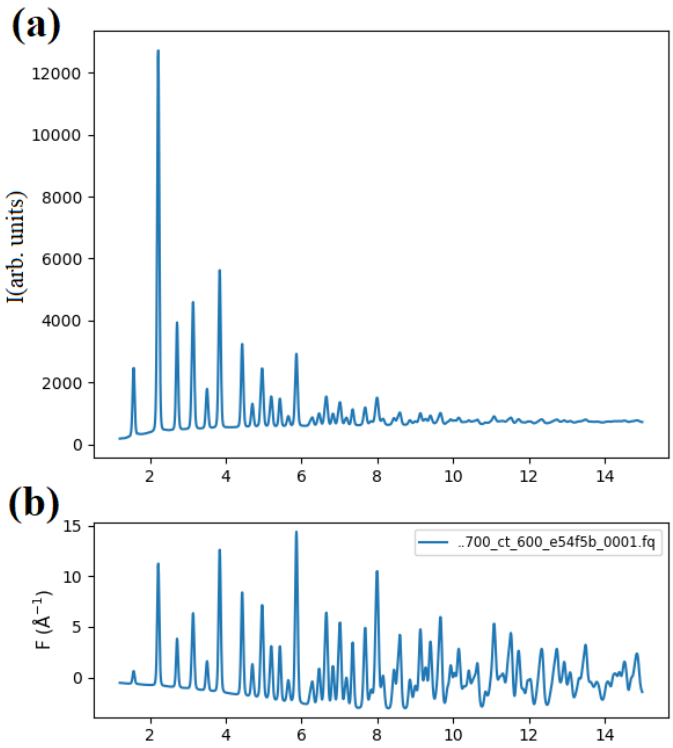

Figure 3.15 Comparison of the (a) raw data and (b) normalized reduced total scattering structure function $F(Q) = Q[S(Q) - 1]$ for 700 nm $BaTiO_3$ powder sample. X-axis is Q (not shown).

As shown above, the rather weak intensities at higher-Q areas, which are neglected in the conventional analysis of data, become quite important features in a total-scattering experiment. This is related to the sample scattering cross-section, and the theory will not be covered here, one can refer Ref. [88(f)] for more details.

The reduced pair distribution function, $G(r)$, is related to $S(Q)$ through the Fourier transform:

$$G(r) = \frac{2}{\pi} \int_{Q_{min}}^{Q_{max}} Q[S(Q) - 1]\sin(Qr)dQ \tag{3.12}$$

It is related to the pair distribution function $g(r)$, which gives the probability of finding an atom at a distance 'r' from a given atom:

$$g(r) = 4\pi\rho_0 r(g(r) - 1) \tag{3.13}$$

The concept can be illustrated in Figure 3.16 below, in general, a peak in the profile indicates the existence of a pair of atoms separated by the distance of a value equal to the peak position.

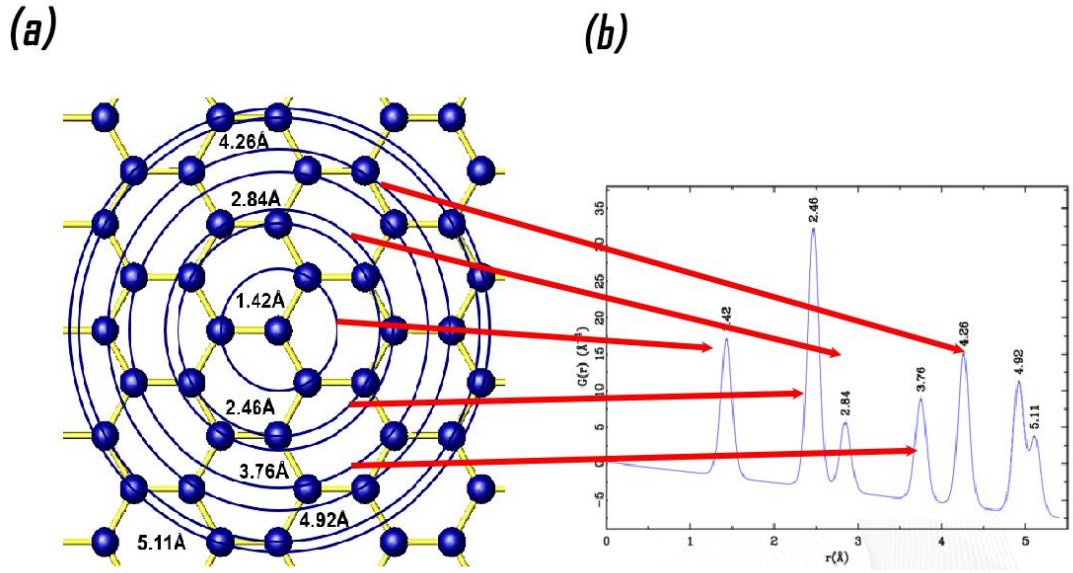

Figure 3.16 Illustrated of (a) schematic diagram of a crystal structure and (b) the corresponding $G(r)$ profile.
Source: T. Proffen, 'PDF Analysis', 18th National School of Neutron and X-ray Scattering, 2016.

Structural information can be extracted from real-space modeling with models described by a small number of atoms in a unit cell and yields information about the local structure. Parameters such as cell parameters, atomic positions, anisotropic thermal

ellipsoids can be refined using a least-squares (LS) approach until a best-fit is reached. The PDF method is especially useful in studying the short to medium range order/disorder in materials. This work uses the software package PDFgui [89] for all the data analysis.

3.7 X-ray Absorption Fine Structure Spectroscopy

X-ray Absorption Fine Structure Spectroscopy (XAFS) uses the X-ray photoelectric effect and the wave nature of the electron to determine local structures around specific atomic species in materials, unlike x-ray diffraction, it does not require long-range translational order – it works equally well in amorphous materials, liquids, polycrystalline solids, and molecular gases. A very detailed description can be found in the book by G. Bunker [90].

XAFS is an intrinsically quantum phenomenon, in which an x-ray photon incident on an atom within a sample is absorbed and excites a core electron to an outer orbit. The x-ray absorption probability is energy-dependent and can be analyzed by measuring the x-ray absorption coefficient, often denoted as μ. The term 'XAFS' is a very broad concept and contains various techniques: Extended X-ray Absorption Fine Structure (EXAFS); X-ray Absorption Near Edge Structure (XANES); Near Edge XAFS (NEXAFS) and Surface EXAFS (SEXAFS). Generally speaking, the techniques that used most are XANES and EXAFS, and it is of practical use to consider XAFS spectroscopy consists of two parts: XANES and EXAFS, such as shown in Figure 3.17:

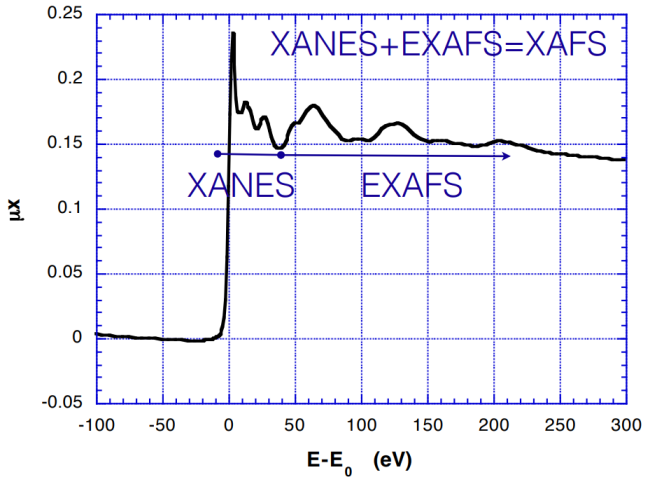

Figure 3.17 XAFS spectroscopy of ZnS transmission.
Source: G. Bunker, 'X-ray Absorption Spectroscopy', 18th National School of Neutron and X-ray Scattering, 2016.

The schematic diagram of the XAFS experiment is shown in Figure 3.18:

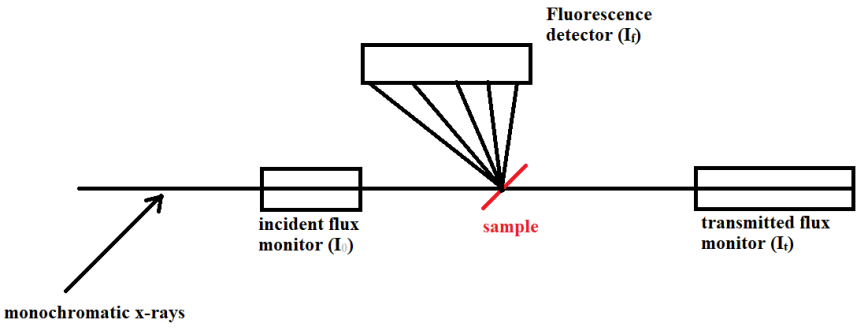

Figure 3.18 Schematic XAFS experiment.

The X-ray absorption coefficient μ is the central quantity of interest, as it leads to the absorption probability, which depends on dipole matrix element between initial core state and final quantum states of the excited electron determined by local structure. For the transmission signal,

$$\mu(E) = log\left({I_0}/{I_t}\right) \tag{3.14}$$

and for the fluorescence signal,

$$\mu(E) \propto {I_f}/{I_0} \tag{3.15}$$

In an XAFS measurement, x-ray photons cause transitions (of the electron of the selected atom) from an inner level to the unfilled final states of appropriate symmetry allowed by a dipole or higher selection rules. If photon energy exceeds binding energy E_0, the electron will have positive kinetic energy and propagates as a spherical wave with wavevector

$$k = \frac{2\pi}{\lambda} = \sqrt{\frac{2m}{h^2}(E - E_0)} \tag{3.16}$$

The electron wave emitted by a central atom is then scattered by neighboring atoms. Qualitatively, the outgoing and scattered parts of the final state wavefunction interfere where the initial state is localized. In general, XAFS determines the statistical properties of the distribution of atoms relative to the central absorbers. This information is encoded in the chi function:

$$\chi\,(E) = \frac{\mu(E) - \mu_0(E)}{\mu_0(E)} \tag{3.17}$$

in which $\mu_0(E)$ is the absorption coefficient without any neighboring atoms. The chi function represents the fractional change in the absorption coefficient that is due to the presence of neighboring atoms and can be modeled with mathematical approaches to extract local information around the central atom. Details can be found in ref. [90]. Here only the most basic form of the EXAFS equation is listed (single scattering only):

$$\chi\,(E) = \langle S_0^2 \sum_i \frac{3cos^2(\theta_i)}{kr_i^2} |f_i(k;r)| e^{-2r_i/\lambda(k)} \sin(2kr_i + \delta_i(k;,r)) \rangle \tag{3.18}$$

where r_i is the distance to the i_{th} neighbor; λ is the electron mean free path, and S_0^2 is a loss factor; f_i is the electron scattering amplitude of atom i, and δ_i is the phase shift. θ_i is the angle between the electric polarization vector of the x-ray beam and the vector from the central atom to neighboring atom i.

3.8 Heat Capacity

Heat Capacity is the ratio of the amount of heat that an object absorbs (or releases) to the change of the object's temperature in the limit of small temperature changes. The heat capacity per unit mass is called the specific heat. The expression is by definition:

$$C_p = \left(\frac{dQ}{dT}\right)_p, C_v = \left(\frac{dQ}{dT}\right)_v \tag{3.19}$$

Here the subscription p and v stand for constant pressure and volume. In this work, heat capacity measurements are conducted under constant pressure, therefore the C_p denotation will be used.

Heat capacity measurements conducted in this work are performed with the Physics Property Measurement System (PPMS), a schematic diagram of the setup is shown in Figure 3.19 below.

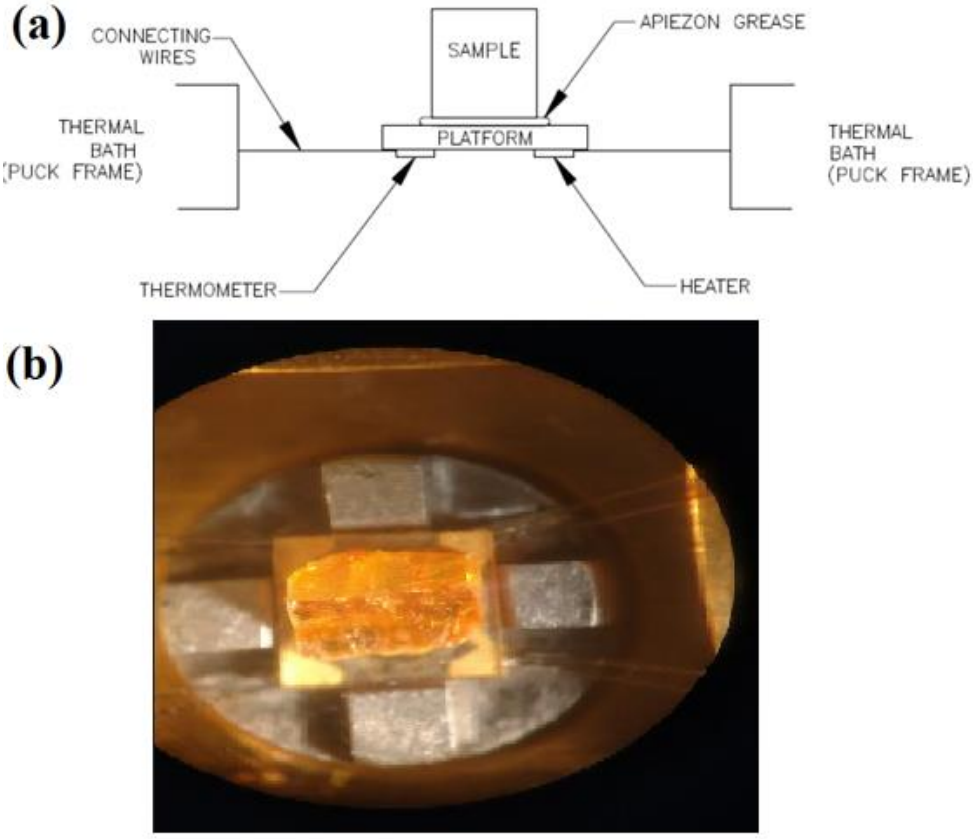

Figure 3.19 (a)Schematic diagram of a heat capacity measurement. (b) Image of the sample stage in our PPMS during heat capacity measurement.
Source: (a) user guide for Physics Property Measurement System, Quantum Design.

The PPMS system (Quantum Design) uses a relaxation technique for the accurate heat capacity measurement. After each measurement cycle–which is a heating period followed by a cooling period– the Heat Capacity option fits the entire temperature response of the sample platform to a model that accounts for both the thermal relaxation of the sample platform to the bath temperature and the relaxation between the sample platform and the sample itself [91]. By modeling this effect, the software can report the correct heat capacity values despite such poor contact. Before each measurement, a blank holder (everything but the sample) is used to determine the background C_p. Multiple measurements (typically) three are conducted at each temperature. In addition, samples are run in both warming and cooling directions to search for hysteresis effects if peaks due to transitions are seen in the samples.

3.9 Density Functional Theory (DFT)

The density functional theory (DFT) [92] with local spin density approximation (LSDA) is a very efficient and accurate scheme for modeling the many-electron problem of a system with fixed nuclei positions, such a crystal. The total energy in terms of the spin density $\rho_\sigma(r)$ is:

$$E_{tot}(\rho_\uparrow, \rho_\downarrow) = T_s(\rho_\uparrow, \rho_\downarrow) + E_{ee}(\rho_\uparrow, \rho_\downarrow) + E_{Ne}(\rho_\uparrow, \rho_\downarrow) + E_{xc}(\rho_\uparrow, \rho_\downarrow) + E_{NN} \qquad (3.20)$$

with E_{NN} the repulsive Coulomb energy of the fixed nuclei and the electronic contributions, T_s is the kinetic energy, E_{ee} is the electron-electron repulsion, E_{Ne} is the nuclear-electron attraction and E_{xc} is the exchange-correlation energies. For LSDA,

approximation has been made that E_{xc} can be written in terms of a local exchange-correlation energy density μ_{xc} times the total electron density as:

$$E_{xc} = \int \mu_{xc}(\rho_{\uparrow}, \rho_{\downarrow}) * [\rho_{\uparrow} + \rho_{\downarrow}]dr \tag{3.21}$$

Further, orbitals χ_{ik}^{σ} constrained to construct the spin densities need to be introduced to effectively minimize the total energy E_{tot}.

$$\rho_{\sigma}(r) = \sum_{i,k} \rho_{ik}^{\sigma} |\chi_{ik}^{\sigma}|^2 \tag{3.22}$$

Here ρ_{ik}^{σ} are occupation numbers. The variation of E_{tot} gives the Kohn-Sham equations,

$$[-\nabla^2 + V_{Ne} + V_{ee} + V_{xc}^{\sigma}]\chi_{ik}^{\sigma} = \epsilon_{ik}^{\sigma}\chi_{ik}^{\sigma}(r) \tag{3.23}$$

which need to be solved self-consistently in an iterative process by a computational method for solving the many-electron problem.

This work uses the software package wien2k [93] which utilizes the linearized augmented plane wave (LAPW) method for solving the Kohn-Sham equations for the ground state density, total energy, and eigenvalues of a many-electron system.

In the LAPW method, the unit cell of a crystal is divided into two types of regions: non-overlapping atomic spheres and the interstitial region. For the atomic sphere, the expression used for the plane wave is:

$$\emptyset_{\boldsymbol{k}_n} = \sum_{lm} [A_{lm,\boldsymbol{k}_n} \mu_l(r, E_l) + B_{lm,\boldsymbol{k}_n} \dot{\mu}_l(r, E_l)] Y_{lm}(\hat{r}) \tag{3.24}$$

where $Y_{lm}(\hat{r})$ is the spherical harmonics, $\mu_l(r, E_l)$ is the regular solution of the radial Schrödinger equation for energy E_l and the spherical part of the potential inside sphere t; $\dot{\mu}_l(r, E_l)$ is the energy derivative of μ_l; A_{lm} and B_{lm} are coefficients.

In the interstitial region, the expression for a plane wave is like:

$$\emptyset_{k_n} = \frac{1}{\sqrt{\omega}} e^{i\boldsymbol{k}_n \cdot \boldsymbol{r}} \tag{3.25}$$

The solution to the Kohn-Sham equations are expanded in this basis set of LAPW's according to the linear variation method:

$$\psi_{\boldsymbol{k}} = \sum_n c_n \emptyset_{k_n} \tag{3.26}$$

The coefficients c_n are calculated by the Rayleigh-Ritz variational principle. The convergence criterial is controlled by a cutoff parameter $R_{mt}K_{max}$, where R_{mt} is the smallest atomic sphere radius in the unite cell and K_{max} is the magnitude of the largest K vector in equation (3.26).

CHAPTER 4

PROBING MAGNETOSTRUCTURAL CORRELATIONS IN MULTIFERROIC $HoAl_3(BO_3)_4$

4.1 Introduction

The system $HoAl_3(BO_3)_4$ has recently been found to exhibit a large magnetoelectric effect. To understand the mechanism, macroscopic and atomic level properties of $HoAl_3(BO_3)_4$ were explored by temperature and magnetic field dependent heat capacity measurements, pressure and temperature dependent x-ray diffraction measurements, as well as temperature and magnetic field dependent x-ray absorption fine structure measurements. The experimental work was complemented by density functional theory calculations. An anomalous change in the structure is found in the temperature range where large magnetoelectric effects occur. No significant structural change or distortion of the HoO_6 polyhedra is seen to occur with a magnetic field. However, the magnetic field dependent structural measurements reveal enhanced correlation between neighboring HoO_6 polyhedra up to near 3 T. A qualitative atomic-level description of the mechanism behind the large electric polarization induced by magnetic is developed. Figures and tables in this chapter are from Zhang, *et al*., Physical Review B Condensed Matter and Material Physics, **92** (10), 104108 (2015).

4.2 Experimental and Computational Methods

$HoAl_3(BO_3)_4$ single crystals were grown from solution–melts based on bismuth trimolybdate and lithium molybdate. The facets of the crystals are smooth. The color of

crystals appears pink under fluorescent light. For all powder samples in the experiments, the crystals were ground and sieved to 500 mesh particle size (< 25 μm).

Single crystal diffraction measurements were conducted at room temperature on a single crystal of dimensions 0.19 mm × 0.30 mm × 0.58 mm using an APEX II diffractometer with Cu Kα radiation following the experimental methods and analysis approach described in Ref. [94]. The refinement results are presented in Table 4.1.

Table 4.1 Structural Parameters from Single Crystal Refinement*

Atoms	**x**	**y**	**z**		
Ho	0	0	0		
Al	0.8901(8)	2/3	2/3		
O1	0.8146(18)	0.4813(17)	0.83333		
O2	0.0770(22)	0.7436(22)	0.83333		
O3	0.8147(15)	0.7827(14)	0.8122(14)		
B1	2/3	1/3	0.8333		
B2	0.2210(28)	0.8870(28)	0.83333		
U_{ij} (Ho)	0.0074(13)	0.0074(13)	0.0112(15)	0.00372(63)	0.0000	0.0000
U_{ij} (Al)	0.0105(22)	0.0122(26)	0.0131(32)	0.0061(13)	0.0012(9)	0.0023(18)
U_{ij} (O1)	0.0244(57)	0.0244(57)	0.0055(56)	0.0167(70)	0.0040(27)	-0.0040(27)
U_{ij} (O2)	0.0152(70)	0.0152(70)	0.0041(70)	0.0050(68)	0.0015(34)	-0.0015(34)
U_{ij} (O3)	0.0210(58)	0.0204(6)	0.0117(43)	0.0098(51)	-0.0066(41)	-0.0002(43)
U_{ij} (B1)	0.0166(97)	0.0166(97)	0.0140(152)	0.0083(48)	0.0000	0.0000
U_{ij} (B2)	0.0108(77)	0.0108(77)	0.019(11)	-0.0005(104)	-0.0098(67)	0.0098(67)

Space Group: R32
a = 9.2891(16) Å, c = 7.2149(13) Å, Dx = 4.445 g/cm^3
Measurement Temperature: 296 K
Crystal Dimensions: 0.18 × 0.30 × 0.58 mm^3
wavelength: 1.54178 Å,
2θmax: 143.5°
BASF twin parameter: 0.178(56)
Absorption Coefficient : 25.25 mm^{-1}
EXTI extinction parameter:0.01485(33)
Number of Unique Observed Reflections $F_o>4\sigma(F_o)$: 228
Number of fitting parameters: 36
Amplitude of Max Peak in Final Difference map: 1.68 e/ Å^3 (Al)
R_1 = 4.98 %, wR_2 = 12.7 %, Goodness of Fit = 1.23

* Atomic displacement parameters Uij (Å^2) are in the order: U_{11}, U_{22}, U_{33}, U_{12}, U_{13} and U_{23}.

Heat capacity measurements on $HoAl_3(BO_3)_4$ single crystals were carried out with a Physical Property Measurement System (PPMS, Quantum Design) for magnetic fields up to 7 T on warming and cooling between 2 K and 300 K, utilizing a relaxation method [91]. Addenda measurements (grease without sample) were collected and subtracted from the sample measurements for each magnetic field.

For x-ray absorption fine structure (XAFS) measurements, polycrystalline samples were prepared by brushing the powder onto Kapton tape. Layers of tape were stacked to produce a uniform sample for transmission measurements with jump $\mu t \sim 1$, where $1/\mu$ is the absorption length. Spectra of $HoAl_3(BO_3)_4$ were measured at the National Laboratory's National Synchrotron Light Source (NSLS) of Brookhaven National Laboratory (BNL) beamline X19A in the ambient field *vs.* temperature and 5 K in a 10 T superconducting magnet for varying magnetic fields.

The Density Functional Theory (DFT) [92] based simulation of $HoAl_3(BO_3)_4$ was carried out by using the full-potential linearized augmented plane wave (FP-LAPW) method as implemented in the WIEN2k code [93]. The spin-polarized calculations with a spin-orbit coupling (SOC) were conducted with the magnetization along the (001) direction. We used the local spin density approximation plus onsite Coulomb interaction (LSDA+U) method with U_{eff} = 5eV. The crystal structure of $HoAl_3(BO_3)_4$ was obtained from our single crystal x-ray diffraction measurement. The convergence parameter $R_{mt}K_{max}$ was set to 7 with G_{max}= 18. Two thousand uniformly distributed k-points were used. A total energy convergence of 10^{-5} Ry was used as the convergence criterion. The phonon density of states (DOS) was obtained by first optimizing the structure (coordinates) at the experimental lattice parameters and conducting a frozen phonon

calculation using the VASP code [95]. The phonon density of states was then used to compute the heat capacity.

High-pressure x-ray diffraction experiments with powder samples were conducted on the X17C beamline at NSLS (at BNL). The data were collected in two independent runs for pressures between 0.6 to 10.2 GPa and the range 2.0 to 9.0 GPa, respectively. Monochromatic focused beams of size 22 μm × 25 μm (first run) and 25 μm × 20 μm (second run) were used. A wavelength of 0.4066 Å was used for the first run and 0.40722 Å was used for the second experiment. The powder diffraction images were collected with a Rayonix165 charge coupled device (CCD) detector. All experiments were performed in a diamond-anvil cell (DAC) with 400 μm culets with 4:1 methanol-ethanol mixture as the pressure transmitting medium. Several ruby chips were placed in different parts of the chamber for pressure measurements based on the ruby fluorescence wavelengths, and the average reading of three different rubies was used as the current pressure. Two 4000-second scans were collected continuously for each pressure with the sample. The program Fit2D [96] was utilized to integrate the two-dimensional diffraction images to yield one-dimensional intensity *vs.* 2θ XRD patterns. Rietveld refinements on the powder XRD data were conducted using the JANA2006 [97] software package.

Atomic Pair Distribution Function (PDF) analysis [88] is an effective method of studying the structural information of materials incorporating both the periodic and disordered features. The relative atomic positions, or the interatomic positional correlations, can be described by the function $G(r) = 4\pi r[\rho(r) - \rho_0]$, where ρ_o is the average atomic number density, $\rho(r)$ is the atomic pair-density, and r is a radial distance from a given scattering center. We performed two independent x-ray powder diffraction

experiments (Set A between 10 K and 350 K and Set B between 80 K and 350 K) to obtain the data required for the PDF study. Both were conducted at the X17A beamline at the NSLS, BNL. Data sets A and B both had the same experimental setup with x-ray beams 0.5 mm × 0.5 mm in size and wavelength $\lambda = 0.1839$ Å. The sample was packed in a cylindrical polyimide capillary 1mm in diameter. For data set A, it was placed 204.62 mm from the detector (and for data set B it was placed 206.05 mm away). Calibration was done by using a nickel standard. Set A was collected in a continuous flow cryostat with a cold finger, while set B was collected in a nitrogen gas stream system (Oxford Cryostream). The experimental background for each set-up was obtained by measuring empty sample holders in the same apparatus. The scattering data were collected with a Perkin-Elmer area detector. Multiple scans were performed for a total exposure time of 60 s (Set A) and 240 s (Set B) per temperature point. The Fit2D package was utilized to integrate two-dimensional diffraction images to yield one dimensional intensity *vs* 2θ XRD patterns. The intensity data were corrected and normalized to obtain the total scattering structure function S(Q) and then the atomic pair distribution function (PDF), G(r), using the PDFgetX3 [98] program. In the Fourier transform step to get G(r) from S(Q), the limits for the Q-range were chosen to reduce termination ripples. We used Q_{min} = 0.1 Å $^{-1}$and Q_{max} = 20.0 Å^{-1}. The program PDFgui was used to refine the structure at each temperature based on the extracted G(r) [89]. Data were first fit at 300 K (space group R32) and the refinement results were used for higher and lower temperature data sets for each consecutive temperature point. Unit cell parameters as well as atomic displacement parameters obtained from our single crystal x-ray measurement at room temperature were used as the initial values. In both data sets, anisotropic atomic

displacement parameters (ADPs) ($U_{11} = U_{22} \neq U_{33}$) were applied due to the hexagonal nature of the cell. The lattice parameters and ADPs were refined but the atomic coordinates were held fixed. This latter assumption is expected to be appropriate in this extremely stiff material as evidenced by the high-pressure results. In addition, it provides the simplest model to track the temperature dependence.

4.3 Results and Discussions

4.3.1 Crystal Structure

Figure 4.1 shows the crystal structure of $HoAl_3(BO_3)_4$, and we note that the cell is hexagonal with space group R32. There are seven unique atomic positions in a unit cell; oxygen atoms occupy three different positions, and boron atoms occupy two positions. We label them as O1, O2, O3 and B1, B2. Ho and Al atoms occupy separate unique sites. This labeling scheme will be used below. Ho^{3+} ions form HoO_6 polyhedra with six O3 atom first neighbors to the Ho site, in the shape of a slightly twisted prism. The HoO_6 polyhedra are connected with BO_3 triangles containing O2 and O3, while the BO_3 triangles containing only O1 are isolated from the HoO_6 polyhedra. No oxygen atom is shared by two nearby Ho ions.

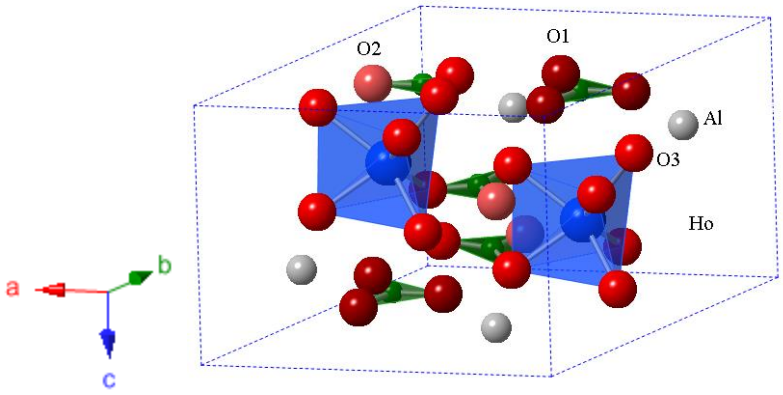

Figure 4.1 Crystal structure of hexagonal $HoAl_3(BO_3)_4$ with HoO_6 polyhedra connected by BO_3 planes containing O2 and O3 ions, while the BO_3 triangles with O1 ions are isolated.

Tables 4.1 and 4.2 present the refinement results of single crystal x-ray diffraction data collected at the room temperature. The unit cell parameters presented in Table 4.1 are consistent with those of the materials in the $RAl_3(BO_3)_4$ family like $TbAl_3(BO_3)_4$ [99]. Atomic displacement parameters are anisotropic ($U_{11} = U_{22} \neq U_{33}$) due to the hexagonal nature of the cell. Table 4.2 contains selected bond distances.

Table 4.2 Bond Distances (Å)

Bond Type	Distance
Ho-O3 × 6	2.323(11)
Al-O3 × 2	1.873(12)
Al-O1 × 2	1.923(11)
Al-O2 × 2	1.931(14)
B1-O1 × 3	1.374(17)
B2-O2	1.338(33)
B2-O3 × 2	1.367(17)

4.3.2. Heat Capacity

There is no current experimental data available for the heat capacity of the $RAl_3(BO_3)_4$ family for comparison while the behaviors of the heat capacity from multiple materials in the $RFe_3(BO_3)_4$ system are well studied (see above). The heat capacity data collected in this work for $HoAl_3(BO_3)_4$ are given in Figure 4.2 to 4.4. Figure 4.2(a), 4.2(b) and 4.2(c) present the results of heat capacity measurements under variable temperatures (2 – 300 K) and magnetic fields (0 – 8 T). There are no structural phase transitions (sharp features) observed (Figure 4.2(a)), although a smooth bump can be observed near 10 K (see the inset of Figure 4.2(a)). Measurements done on cooling from above this region down to 2 K and returning to the region above this feature (at 0 T) reveal no hysteresis, supporting the idea that there is no long-range structural transition associated with this feature. The position of the feature near 10 K moves to higher temperatures for magnetic fields above 2 T. This feature is possibly associated with Schottky anomalies (associated with the Ho crystal field) or possibly with a magnetic field induced ordering of Ho sites.

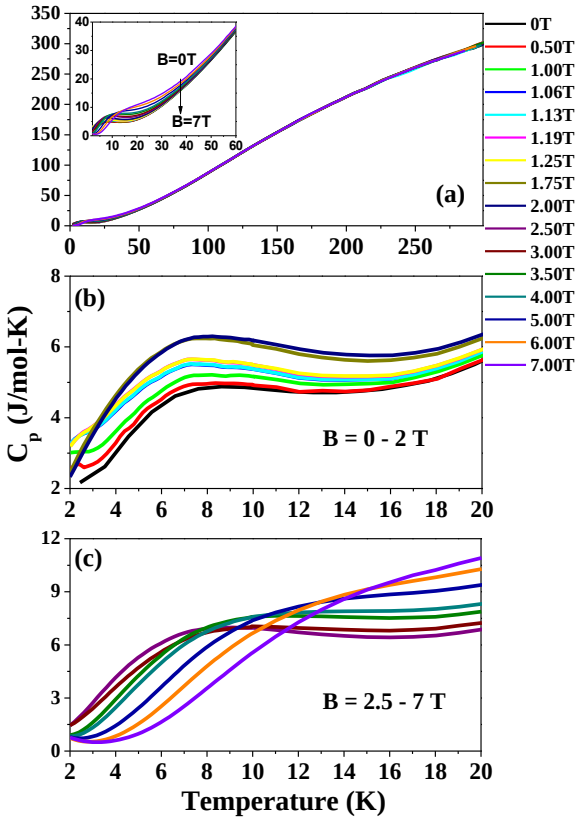

Figure 4.2 (a) Heat Capacity measurement of $HoAl_3(BO_3)_4$ between 2 to 300 K under magnetic fields from 0 to 7 T. The inset shows the low-temperature region between 2 to 60 K**.** Expanded scales for the region between 2 to 20 K are given in (b) and (c). The position of the peak shifts to a higher temperature for magnetic fields above 2 T.

The contribution of the Ho subsystem in specific heat has been studied theoretically (Schottky) and calculated in by Begunov *et al.,* based on a Hamiltonian which includes crystal field, Zeeman and Hyperfine interaction contributions [100]. Properties were calculated by diagonalizing the Hamiltonian for varying temperatures and magnetic fields. The contribution of the Ho subsystem was calculated by the formula $C_{Ho} = k_B \frac{<E^2>-<E>^2}{(k_B T)^2}$, where $<E^2>$ and $<E>^2$ using the derived states for varying

magnetic fields and temperatures. This atomic-like model predicted a shift of the wide peak near ~ 10 K to the low temperature region for external magnetic fields between 0 to 1 T, and towards the high temperature region for magnetic fields from 3 T to 6 T, which is similar to our results. Calculations were performed for magnetic fields at a limited set of values: 0, 0.1, 0.3, 0.5, 1, 3 and 6 T.

While the crystal field model has been used the describe the behavior of the heat capacity at low temperatures in $RAl_3(BO_3)_4$ system, in $RFe_3(BO_3)_4$ evidence has been found for order at the R site for R=Nd, Sm, Er, Ho, and Tb. For R=Nd both the Fe and Nd sites exhibit magnetic order below 30 K [101]. For the R=Sm system, simultaneous ordering of the Fe and Sm sites occurs at 34 K [102]. For R=Er, Tb and Ho, ordering of both sites occurs at 32, 40 K and 38 K, respectively [103]. In these systems coupling between the Fe and R site occurs which possibly enable this ordering. We note that recent work on the $HoAl_3(BO_3)_4$ system suggest an ordering of the Ho site at a temperature which is consistent with the appearance of the magnetoelectric effect [104]. While both approaches have been applied to this system, the emphasis here is to understand the magnetostructural correlations.

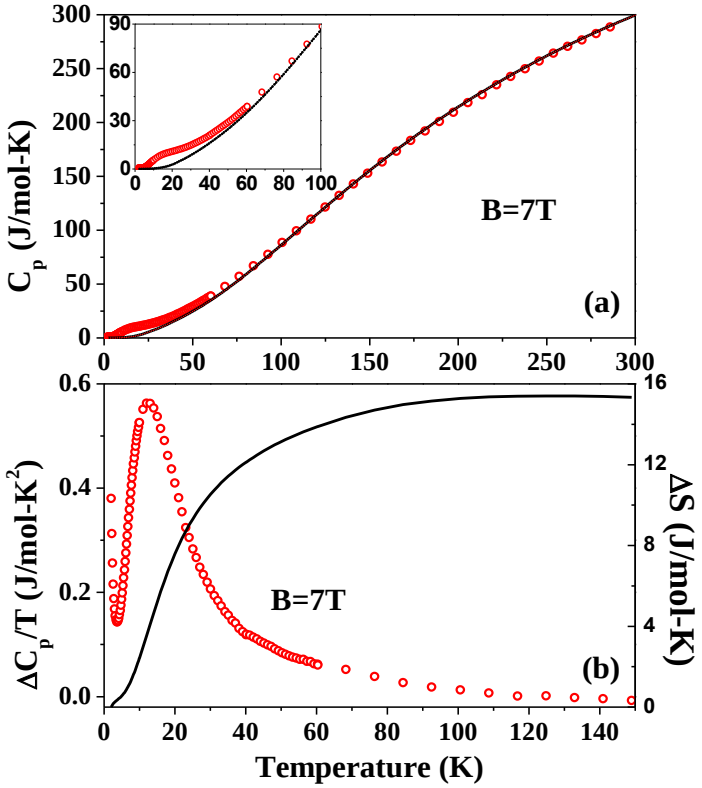

Figure 4.3 (a) Experimental value of heat capacity (red circles) at 7 T compared to DFT simulated (modeling the phonons) result (black dashed line). The inset shows an expanded scale for the low-temperature region. It can be seen that our simulated result agrees well with the experimental values in the high-temperature region, while significant deviations start to show up at around 60 K. (b) Difference of Experimental and simulated value of heat capacity (red circles) between 0 and 150 K under 7 T, and the calculated change in entropy (black solid line).

It is found in this work that the behavior of the specific heat has strong magnetic field dependence. The solid black line in Figure 4.3(a) gives our simulated result (Density Functional Theory model of the phonons from the frozen phonon method) for the lattice only contribution to the heat capacity of $HoAl_3(BO_3)_4$. The simulated and the experimental data match very well above ~ 60 K. This suggests that the heat capacity of HABO system is mostly from the lattice for temperatures above 60 K. The difference

between the lattice and the measured heat capacity is indicated as ΔC_P is shown in Figure 4.3(b) as the open circles. The change in entropy can be computed directly by integrating ΔC_P /T. Figure 4.3(b) also shows the calculated change in entropy for a 7 T magnetic field. Figures 4.4(a), 4.4(b), 4.4(c) give the overall picture of all the data at all magnetic fields studied. The change in entropy is seen to approach a constant value with the increase of temperature, as expected. It is seen to saturate for magnetic fields above ~ 2 to 3 T. These results are consistent with the saturation of the magnetization for magnetic fields above ~ 3 T (see Figure 4.13(e) below) at low temperature. However, it is important to note that our calculated results should be somewhat smaller than their actual values because of the omission of the region below 2 K in our measurements. This region is below the working range of our instrument. Both free Ho ion models and crystal field models predict saturation of the entropy with increasing magnetic fields. We note that in a single ion field induced Ho alignment model that the change in entropy has a value given by $\Delta S = R \ln(2S+1)$. For Ho^{3+} ($4f^{10}$) with S = 2 (or 4 μ_B per Ho Site) we obtain ΔS = 13. 4 J/(mol×K), which is close to observed results. To distinguish between these models, detailed crystal field modeling covering the range of magnetic fields and temperatures discussed here as well as systematic temperature and magnetic field dependent neutron diffraction experiments are needed. The models will be constrained by these heat capacity measurements. Here we focus on the structural properties.

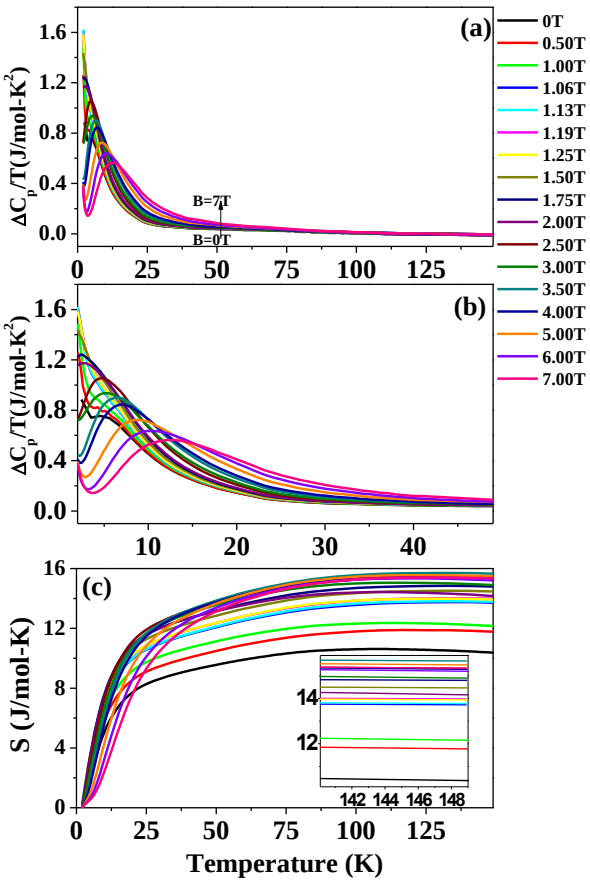

Figure 4.4 (a) Difference between the experimental and simulated value of heat capacity for magnetic fields from 0 to 7 T. (b) An expanded scales of temperature region between 2 and 50 K. The position of the peak shifts toward higher temperature region with the increasing magnetic field above 2 T, while no obvious trends are observed below 2 T. (c) The calculated changes in entropy. The curves converge to the same approximate value with increasing magnetic field. The inset is an expanded scale between 140 and 149 K.

4.3.3. High-Pressure X-ray Diffraction

Figures 4.5 to 4.8 show the results from high-pressure x-ray diffraction measurements between 0.6 and 10.2 GPa. Figures 5(a) and 5(b) show the XRD patterns of $HoAl_3(BO_3)_4$ in two data sets.

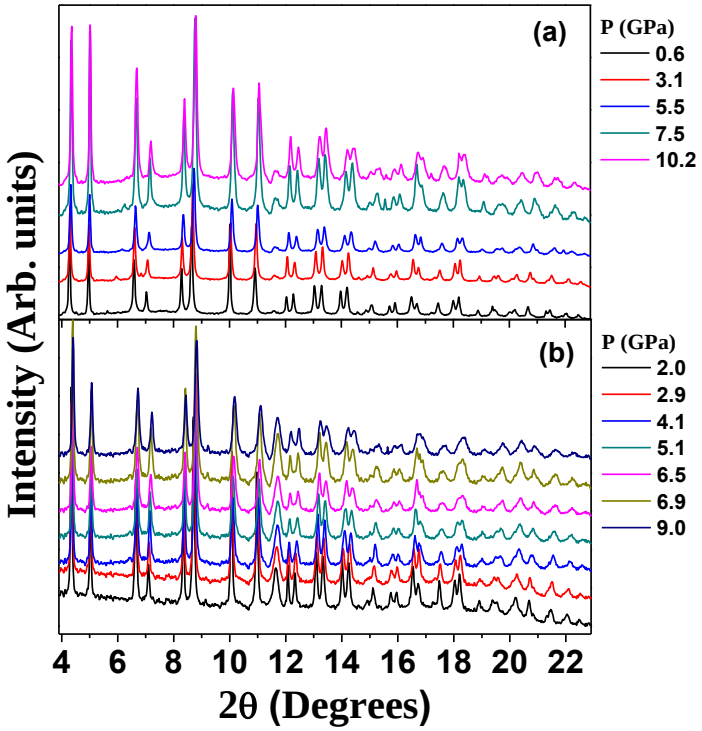

Figure 4.5 High-pressure synchrotron XRD patterns of (a) set A, (b) set B for $HoAl_3(BO_3)_4$. Peak positions continue shift systematically to higher 2θ values with increasing pressure.

No new peak appears in the whole pressure range indicating a continuous compression process on the samples without a structural phase change. The expected shift of the peaks to higher angle with increased pressure is seen. Rietveld refinements were performed on the XRD data to obtain the structural parameters. The profile of the refinement (data fit) is shown in Figure 4.6 for P = 0.64 GPa.

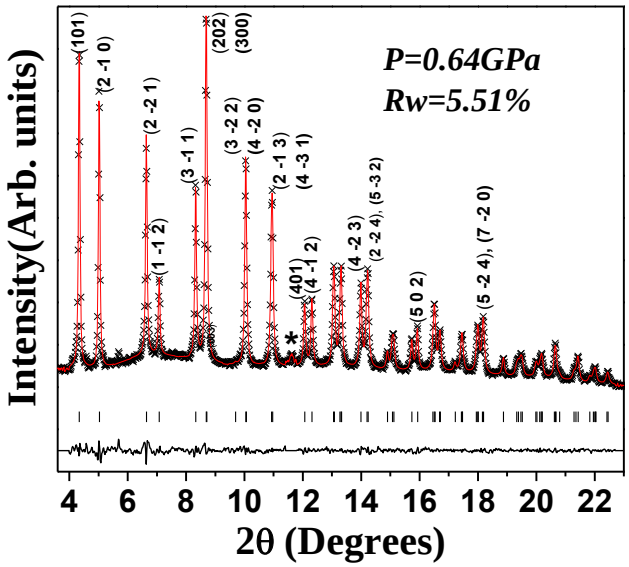

Figure 4.6 Rietveld refinement result at 0.64 GPa. The observed (crosses), calculated (solid line) and difference (bottom line) patterns are shown. The vertical bars show the peak positions for the refined hexagonal model. The symbol * indicates a peak of the steel gasket.

The small gasket peak region (steel gasket, indicated as *) was excluded during the refinement. The lattice change with pressure is shown in Figure 4.7.

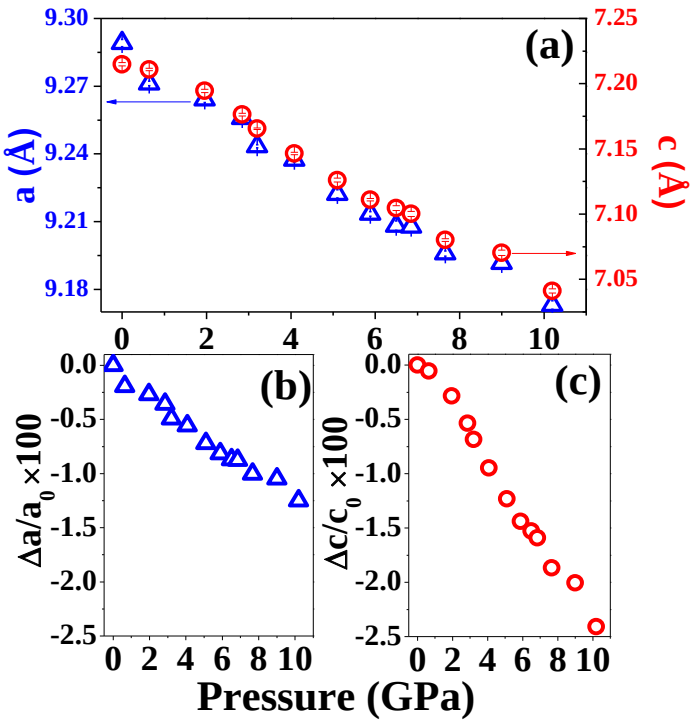

Figure 4.7 (a) Cell parameters of $HoAl_3(BO_3)_4$ obtained from the Rietveld refinements, with a (blue), c(red) *vs.* pressure shown, respectively**.** Pressure-dependent percent change in cell parameters, (b) a, (c) c, respectively.

The lattice is compressed at an almost constant rate in the entire pressure range, but the *c* direction is softer than the *a* direction. No anomalies are observed. The pressure dependent volume change can be seen in Figure 8(b) (black triangles). A first-order equation of state fit using the Murnaghan equation was performed, and the fitting curve is almost linear. The bulk modulus B_0 and its pressure derivative B_0' obtained from the fit are B_0 = 190.93 ± 10.35 GPa, B_0' = 3.30 ± 2.75GPa. B_0' behaves normally (typical values of B_0' are between 2 to 8 [105]). No current data are available for B_0 for other materials in the RABO family. However, comparison can be made with the values of B_0 for some other well-known materials including (in GPa): NaCl (24.0), bulk silicon (94) [105], MgO (156), $CaCO_3$ (75.3), 3C-SiC (248) [106], Diamond (442) [107], $LaMnO_3$ (108) [108]. It can be seen that B_0 for $HoAl_3(BO_3)_4$ is close to 3C-SiC(248), indicating a

very stiff material. This was also observed in these measurements as extreme difficulty in grinding this material.

DFT calculations were performed to make contact between models and the experiments. As can be seen in Figure 4.8, the red closed circles are the DFT calculated results of *c/a* (Figure 4.8 (a)) and V/V_0 (Figure 4.8 (b)) respectively.

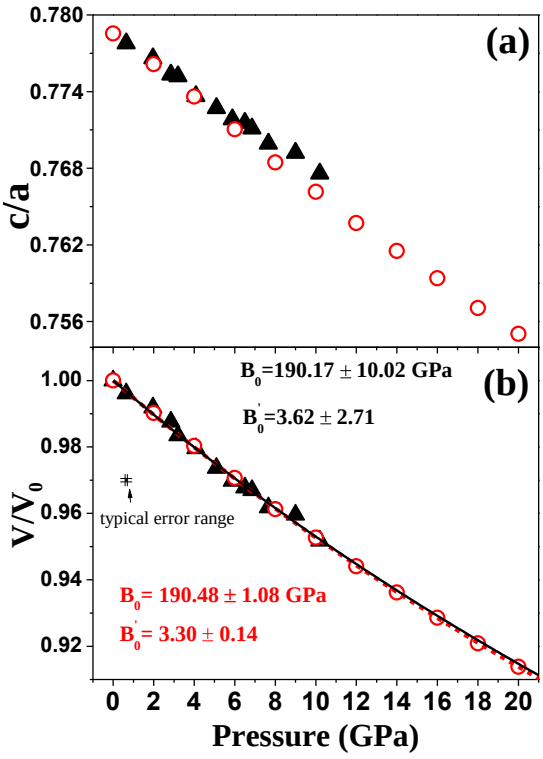

Figure 4.8 (a) Lattice parameter ratio c/a for experimental results (black triangles) and DFT calculated values (red circles). (b) V/V_0 for experimental results (black triangles) and DFT calculated values (red circles). The lines show the first order Murnaghan equation of state fit of experimental (solid) and DFT simulated (dash) results, respectively. V_0 = 539.1 $Å^3$ was used. Bulk Modulus (B_0, in GPa) compared with other materials: NaF (46.5), NaCl (24.0), MgO (156), $CaCO_3$ (75.27), 3C-SiC (248), $LaMnO_3$ (108), indicates that this material is very stiff.

The calculated values match reasonably well with the experimental results (black triangles). Moreover, the bulk modulus B_0 obtained from DFT calculations has a value of B_0 = 190.01 GPa, which is almost the same as the refinement results. These results and the heat capacity results indicate that the system can be readily modeled with DFT methods. Our high-pressure study also supports the observation of the anisotropic compressibility of $HoAl_3(BO_3)_4$ in which *c* is softer than *a*, as well as the stiffness of the sample. These properties should also be observed in temperature-dependent experiments. The changes in structure coincide with the region of larger magnetoelectric effects at low temperature and may possibly be related. Since low-temperature changes (lattice contraction) can be achieved by the application of high pressure, the application of pressure may enable us to probe low-temperature properties and electrical polarization measurements under pressure should be explored.

4.3.4 High Energy X-ray Diffraction (PDF measurements)

High scattering angle XRD data on $HoAl_3(BO_3)_4$ powder samples were taken for a PDF study. The image for a typical data set can be seen in Figure 4.9.

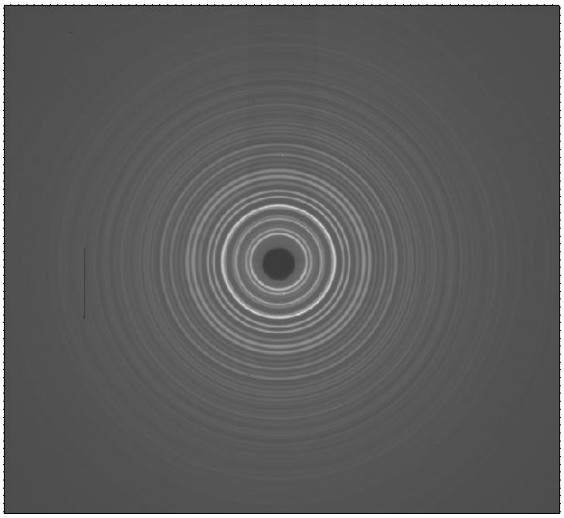

Figure 4.9 Two-Dimensional XRD raw data collected using a Perkin Elmer detector for the $HoAl_3(BO_3)_4$ powder sample. The data collected has very high quality with no bright spots from single crystal particles.

Note that no high-intensity spots from large single crystal particles are detected, and the circles are approximately continuous. The solid vertical line on the left side of the image shows a line of dead pixels in the detector, which was masked during data processing. Two independent data sets (A and B) were collected. The PDF technique is sensitive to the short-range structure and local bond distance in addition to the long-range periodic structure [88(b)]. Local distortions can be readily determined. Figure 4.10 shows the refinement result of $HoAl_3(BO_3)_4$ from 1 to 20 Å at room temperature from set B.

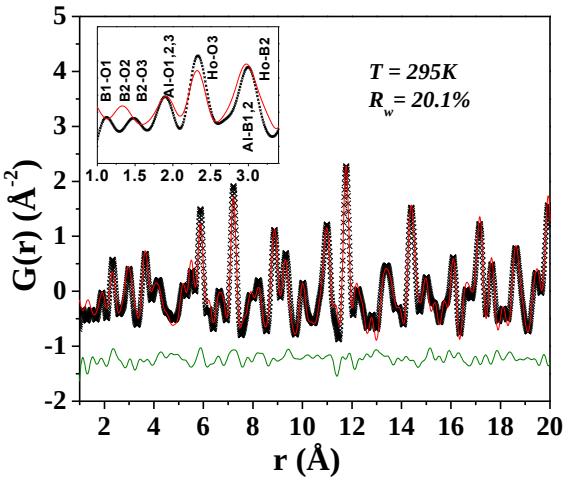

Figure 4.10 PDF G(r) of from the $HoAl_3(BO_3)_4$ powder sample (crosses), fit (solid red line) and the difference (bottom green line) are shown. The inset shows an expanded area of low r region with the corresponding bond(s) labeled.

The first atomic pair distance is above 1 Å (see Table 4.2), so the area between 0 to 1 Å were excluded from the refinement. The weighted R-factor R_w is 20.1%, which compares well with the value of perovskites such as $BaTiO_3$ [109] and other complex oxide systems. (Note that $R_w = \sqrt{\frac{\sum_{i=1}^{N} w(r_i)[G_{obs}(r_i)-G_{calc}(r_i)]^2}{\sum_{i=1}^{N} w(r_i)G_{obs}^2(r_i)}}$, with G_{obs} and G_{calc} as the experimental and calculated PDF, respectively, the weight for each data point is given by $w(r_i)$ [81(b)].) Atomic displacement parameters (ADPs, $U_{11} = U_{22} \neq U_{33}$) for Ho, Al, O1, O2 and O3 were refined, and U_{iso} was determined using $U_{iso} = (U_{11}+U_{22}+U_{33})/3$.

Figure 4.11 shows the temperature-dependent lattice parameters retrieved from the PDF refinement.

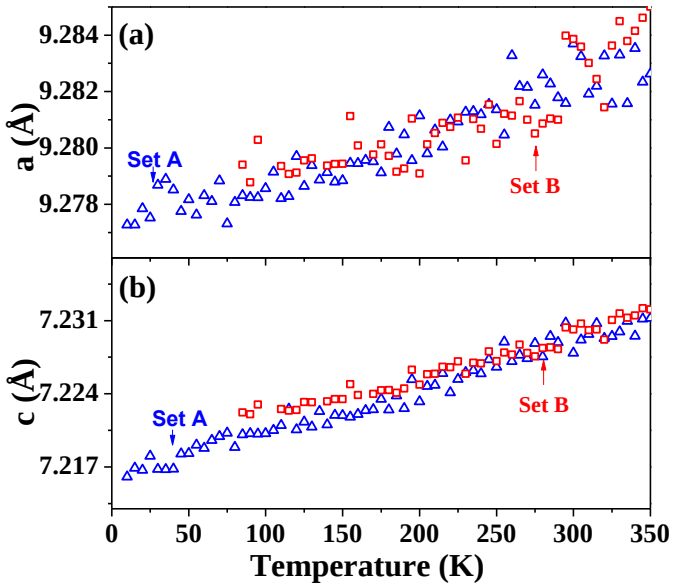

Figure 4.11 Cell parameters (a) a, (b) c, respectively, retrieved from a fit of PDF G(r). Blue triangles are the results from set A, while red squares are from set B.

The result from set A matches well with the ones from set B, suggesting our results are very reproducible. It can be seen that the change of *a* in the whole temperature range is very small (~10^{-3}Å), while the change in *c* is relatively larger (~10^{-2}Å). This indicates that the cell is softer in *c* direction, which agrees well with our observation from the pressure-dependent XRD measurements. Temperature-dependent ADPs are shown in Figure 4.12, for (a) Ho, (b) Al, (c) O1, (d) O2, (e) O3, respectively.

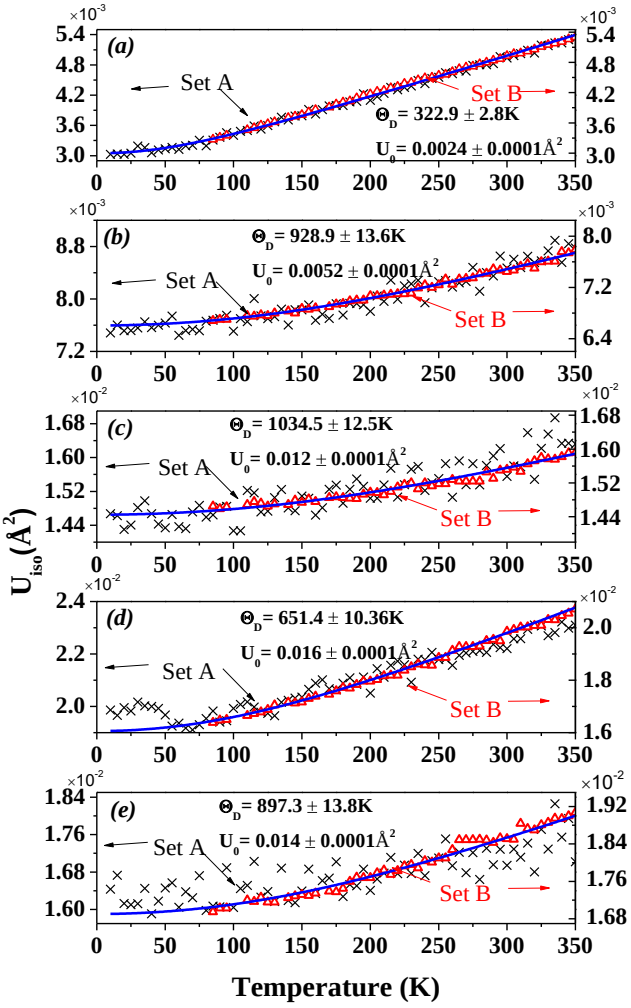

Figure 4.12 Refinement results of atomic displacement parameters (ADPs, U_{iso}) measured from 10 K to 350 K of each atom as (a) Ho, (b) Al, (c) O1 (d) O2, (e) O3, respectively. Set A (crosses) and Set B (triangles) are plotted on the same graph. The solid blue lines stand for the Debye model fits for set B. A small bump is detected for Ho at about 30 K, and a very significant change is seen for O2 below 50 K.

The results from set A are more scattered than the results from set B, mainly due to the experimental setup difference (A has 60 s counting time while B has 240 s counting time per temperature point). However, the overall trends and average results are similar. The most unusual variation in the structural parameters of $HoAl_3(BO_3)_4$ occurs at

low temperature. Hence, set A is focused on. The blue curves in Figure 4.12 are the fitting results based on a Debye model [110] given by $U = \frac{3h^2T}{4\pi^2 mk\Theta^2}[\phi(x) + \frac{1}{4}x] + U_0$, where x= $\frac{\Theta}{T}$ and $\phi(x) = \frac{1}{x}\int_0^x \frac{\xi d\xi}{e^{\xi}-1}$; Θ is the Debye temperature; *h* and *k* are the Planck and Boltzmann constants; *m* is the mass of the vibrating atom. U_0 reflects the static and nonthermal disorder. The U_0 parameter is quite small and is slightly modified by the experimental setup. Hence the data sets (A and B) are presented with slightly shifted scales (left scale and right scale, respectively) within the same window. It is noticed that the Debye temperatures determined from our fits for each atom are higher than typically found for the corresponding atoms [111]. For example, θ for a rare earth atom is usually < 200 K but here it is ~ 300 K. The value of θ for Al, O1, O2 and O are ~ 930, 1035, 651, and 897 K, respectively. It could be understood because this is a very stiff material, the bonds for atoms should be stronger than those in the normal materials. The larger value of bulk modulus found in our high pressure XRD measurement also supports these results.

In further investigation of ADPs, it is very clear to see a significant deviation in U_{iso} of O2 below 50 K (Figure 4.12(d)), as well as suggestions of a jump in U_{iso} of Ho (Figure 4.12(a)) at about 30 K. Such behavior of the refined-ADPs is usually due to an overall inadequate structural model [112] or some short-ranged effect which disagree with the average long-range structure. As we previously mentioned, there is no long-range structural phase transition occurs at this temperature region. The system possibly exhibits a local distortion [113], in which the Ho and O2 atoms are involved.

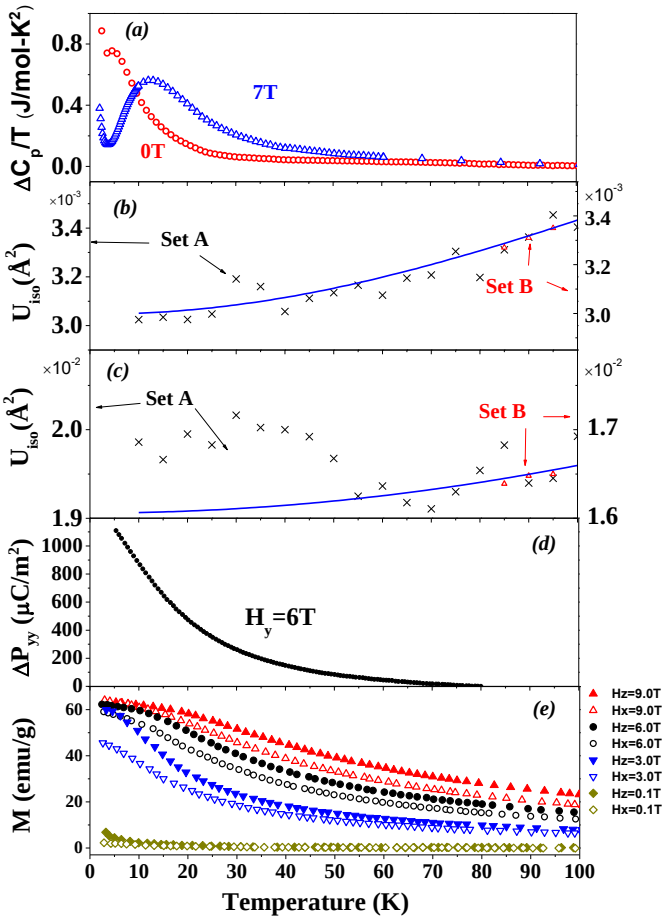

Figure 4.13 (a) Heat capacity measurements between 0 and 100 K at 0 T (red circles) and 7 T(blue triangles), together with ADPs for (b) Ho, (c) O2, respectively. (d) Temperature and field dependences of magnetoelectric polarization ΔP_{yy} taken from Ref. [42] (The magnetic field H was applied along the y-axis and the polarization was also measured along this axis.) (e) The reported magnetization data *vs.* applied a magnetic field (Ref. [42]). The solid symbols stand for H_z = 9 T (red), 6 T (black), 3 T (blue) and 0.1 T (dark yellow), respectively. The open symbols stand for H_x =9 T (red), 6 T (black), 3 T (blue) and 0.1 T (dark yellow), respectively.

Figure 4.13 presents an expanded view of the data between 0 and 100 K. Figures 4.13(d) and 4.13(e) are the reported experimental data for electrical polarization and magnetization taken from Ref. [44]. We note that the anomalies in the Ho and O2 ADPs

occur in the temperature region where the large magnetoelectric effect in $HoAl_3(BO_3)_4$ can be seen. The combined results suggest that the local distortion inside the cell at low temperature may be relevant to the magnetoelectric effect of the system. Since the O2 atoms are outside the HoO_6 polyhedra, a picture of the structure beyond just the HoO_6 polyhedra under a magnetic field is needed, and it will be addressed below.

4.3.5 X-ray Absorption Fine Structure Measurements

Magnetic field dependent absorption measurements at a fixed temperature (5 K) are shown in Figure 4.14, as the XAFS structure functions.

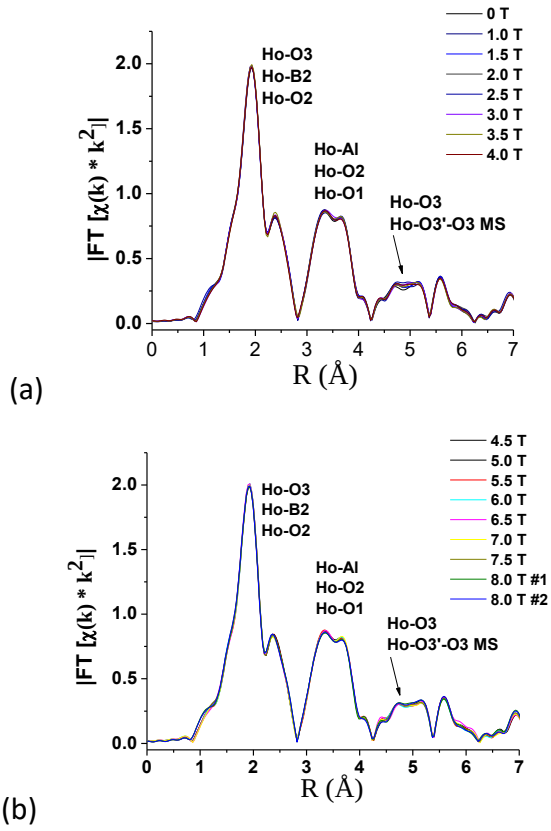

Figure 4.14 XAFS structure function (Fourier transform of fine structure times k^2) taken at 5 K for magnetic fields varying from 0 T to 4 T in (a) and 4.5 T to 8 T (b). Duplicate data sets at 8T (in (b)) show the statistical variation in the data. Note that significant changes occur in the region near ~ 5 Å with the largest change corresponding to magnetic fields increasing from 0 T to 3 T (the structural peaks are identified in Figure 4.16).

Duplicate data sets at 8 T show the statistical variation in the data at a fixed magnetic field. The most significant change in the structure with magnetic field occurs near ~ 5 Å. The structure changes significantly between 0 and 3 T and remains relatively stable for higher magnetic fields. The details will be described in depth below with the discussion of Figure 4.16. Temperature-dependent XAFS structure functions are presented in Figure 4.15. The result indicates a systematic reduction in all pair peaks with increased temperature. It is consistent with a temperature variation of the lattice parameters (Figure 4.11).

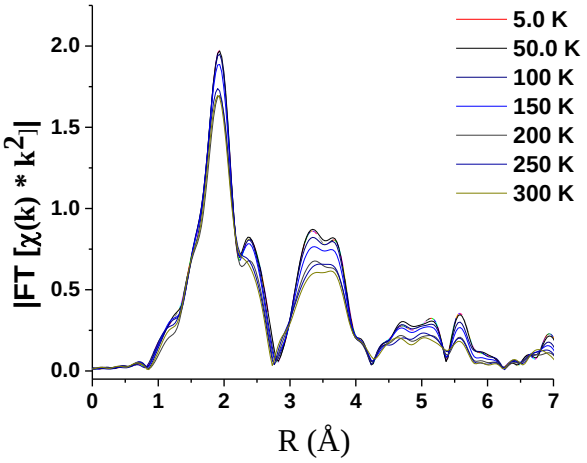

Figure 4.15 Temperate dependent XAFS structure function indicating a systematic reduction of all pair peaks with increased temperature.

The peak mentioned in Figure 4.14 with the most significant change with the magnetic field is further examined in Figure 4.16. It can be seen more clearly that the intensity of this peak near ~ 5 Å shows a strong variation with the magnetic fields up to ~3 T. This specific peak indicated by the arrow corresponds to scattering paths between Ho ions in one HoO_6 prism and the O3 atom on the nearby HoO_6 prism. A single scattering (Ho-O3) and a multiple scattering path (Ho-O3'-O3) which contribute to this

peak are illustrated in Figure 4.16(b). Meanwhile, no significant variation is with magnetic fields is found in the first peak which corresponds to the nearest neighbor Ho-O3 shell in the HoO_6 polyhedra. Specifically, in Figure 4.14, there is no significant change with magnetic fields in the nearest Ho-O3, Ho-B2 Ho-O2 and next major shell containing Ho-Al and Ho-O1/O2 pairs. The data show that the HoO_6 polyhedra remain stable within the entire magnetic field range measured

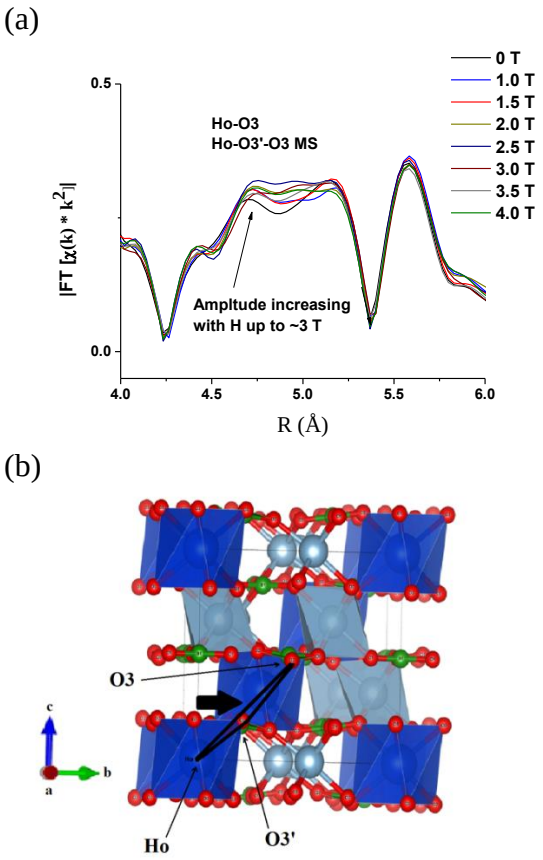

Figure 4.16 Expanded XAFS structure functions for magnetic fields between 0 T and 4 T are shown in (a). In panel (b) the single scattering path Ho-O3 and multiple scattering path (Ho-O3'-O3) associated with the peak are shown. This strong variation at low field (0 to ~ 3 T) is related enhanced coupling of neighboring HoO_6 polyhedra via the BO_3 planes.

Recently, a microscopic model of $HoAl_3(BO_3)_4$ model was reported [44]. In the model, all Ho ions in the crystal hold equivalent positions and are surrounded by a slightly twisted O3 prism with a triangular base. The electron density distribution of the 4f subshell for a Ho^{3+} ion takes the form of an ellipsoid flattened along the quantization axis (along z). The model suggests that without an external magnetic field the 4f subshell of a holmium ion takes the position that has the minimum overlap with the O3 shell, and the magnetic moment is directed along the z-axis (half parallel and half antiparallel). When an external field is applied, for example, in the z-direction, the magnetic moment of one-half of the ions will rotate by 180°. During the rotation, the overlapping of electron (Ho 4f and the O3) charge density will arise, which will create additional electrostatic forces that will cause the strain in the lattice. Such strain will reach its maximum when the magnetic moment of Ho^{3+} is in the xy plane. During this process, the forces acting on the holmium ions will differ for different oxygen ions, and this will lead to a shift of a Ho^{3+} ion in the x-direction. In the model, this process will eventually result in a decrease in the twist angle of the oxygen prism, and thus an electric dipole arises. This model agrees well with the observed fact in Ref. [43] that the $HoAl_3(BO_3)_4$ crystal undergoes positive magnetostriction λ_x and reaches its maximum at about 3 T. But continues to drop with the increasing magnetic field, because according to the model, the strain caused by the rotation of magnetic moment of Ho^{3+} will reach its maximum when it has rotated by 90°, after which it will continue to drop.

With respect to the XAFS results in the magnetic field, we note that the absence of changes in Ho-O3 nearest neighbor peak is inconsistent with the proposed theoretical model (Ref. [44]). Meanwhile, the strong variation of the Ho-O3 and Ho-O3'-O3 peaks

reflects the fact that coupling between two nearby HoO_6 polyhedra will be enhanced with increased magnetic field up to ~ 3 T, reach its maximum and maintain the level between 3 to 8 T. In this system, the magnetic field couples to the lattice and rotates the HoO_6 polyhedra initially but the stiffness of the lattice prevents rotations beyond a certain range. Hence, increasing the field has no effect beyond a cut-off magnetic field (~ 3 T in this case).

4.3.6. Density Functional Theory (DFT) Calculation

Our calculated LSDA+U Density of States (DOS) is shown in Figure 4.17, the total DOS reveals a wide bandgap of HABO with the value of ~ 5 eV, with localized 4f states in the middle of the gap. These results are consistent with the DFT calculations on $TbAl_3(BO_3)_4$ [42].

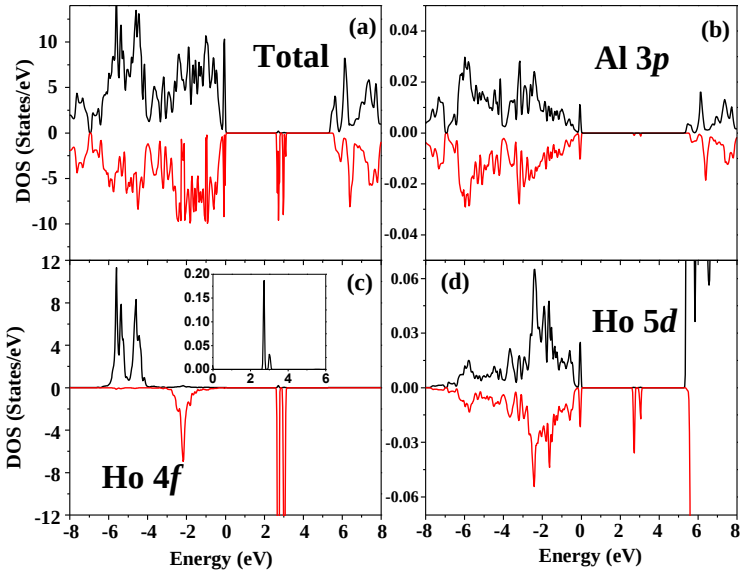

Figure 4.17 Total DOS (a) and the projected DOS of the Al-3p (b), Ho-4f (c) and Ho-5d bands (d). The red lines stand for the spin up contributions and black lines are for the spin down contributions. The inset is an expanded scale of the Ho 4f DOS between 0 and 6 eV.

The spin up states of Ho 4f are mostly between -6 and -3 eV, while the spin down states have a peak at about -2 eV and also occur near the center of the gap. The peak near -2 eV for the 4f spin down DOS is found in other rare earth borate systems including $TbFe_3(BO_3)_4$ [114] and $TbAl_3(BO_3)_4$. But in the Ho system, it is much broader. Unlike the iron borates, only the R ion (Ho for example) contributes to the magnetic properties. Specifically, Al (Figure 4.17 (b)) and oxygen (not shown) shows no direct or induced magnetization based on the calculated DOS.

The total electron density with spin up + spin down is plotted in Figure 4.18.

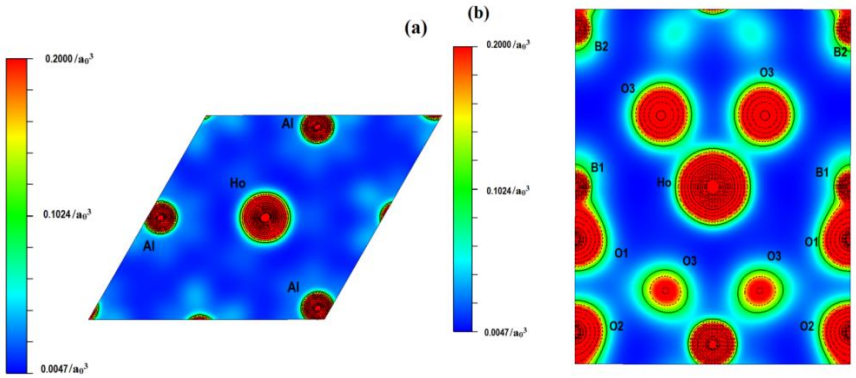

Figure 4.18 Cross section of the total electron density on (a) ab plane (z = 0) and (b) ac plane (x = 0). The Ho iron is centered in both images.

The projection on the ab and ac planes reveals that the shape of Ho density is a very slightly distorted sphere. To study the Ho 4f contribution to the total electron density and its spatial distribution, we calculated the spin density difference (spin up – spin down) [115] (see Figure 4.19). It is seen that the magnetic contribution comes from the Ho site only. The negative isosurfaces (for occupied 4f states near ~ -2 eV shown in Figure 4.17(c)) takes the shape of multiple lobes (Figure 4.19(b)), and the positive ones (for state between -6 and -3 eV) have the shape shown in Figure 4.19(a). All the isosurfaces have a high symmetry and are not significantly distorted with respect to any particular direction. In other words, to first order this moment can be rotated under the

external magnetic field. Therefore, it is unlikely that the rotation of Ho 4f moments will cause significant strain inside the HoO_6 polyhedra. This result supports our results derived from the XAFS measurement that the magnetoelectric properties of HABO system should not be related to the distortion inside the HoO_6 prism.

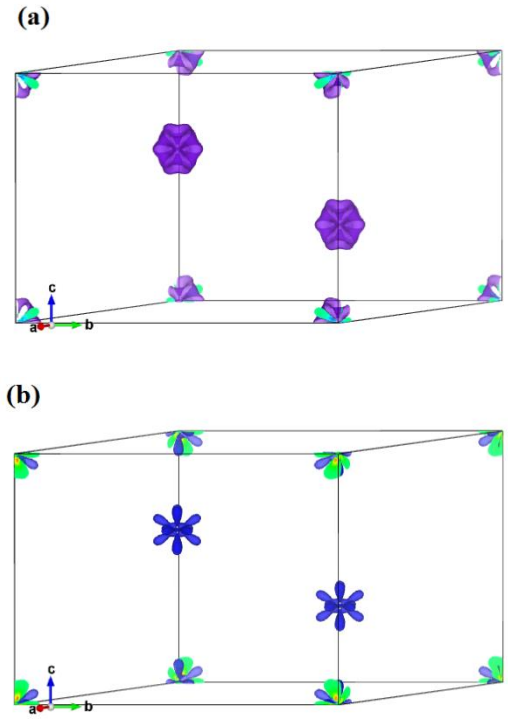

Figure 4.19 Spin density difference (spin up minus spin down) in 3-d space with the isosurface level equal to (a) $0.02/a_0^3$ and (b) $-0.02/a_0^3$, respectively. This emphasizes the Ho 4f band. Only the Ho site has non-zero spin density difference.

4.4 Summary

The magnetostructural properties of $HoAl_3(BO_3)_4$ were explored by temperature and magnetic field dependent heat capacity measurements, pressure, and temperature dependent x-ray diffraction measurements, as well as temperature and magnetic field dependent x-ray absorption fine structure measurements. The heat capacity was

measured (from 2 to 300 K) in magnetic fields (from 0 to 7 T) and the structure was measured form ~ 10 to 350 K. The structure for isotropic pressures between ambient and 10.2 GPa was also measured. Local structural measurements were conducted in magnetic fields (between 0 and 8 T at 5 K). These measurement results were combined with density functional calculations to predict the lattice contribution to the heat capacity, the pressure-dependent structure, the electronic structure, and the spin decomposed charge density. An anomalous change in the structure is found in the region of large magnetoelectric effects, which may be related. More detailed high-resolution temperature-dependent structural measurements and combined magnetic field and temperature structural studies are needed to provide a link between the ground state structure and the magnetoelectric effects.

From a local structure perspective, no significant change or distortion of the HoO_6 polyhedra is seen to occur with a magnetic field. However, the magnetic field dependent structural measurements reveal enhanced correlation between neighboring HoO_6 polyhedra. This observed response is seen to saturate ~ between 2 and 3 T due to the lattice stiffness. These results provide a microscopic level understanding of the mechanism behind the large electric polarization induced by magnetic fields in the general class of $RAl_3(BO_3)_4$ systems (R = rare earth).

4.5 Acknowledgement

This work is supported by Department of Energy Grant DE-FG02-07ER46402. Synchrotron powder x-ray diffraction and x-ray absorption data acquisition were performed at Brookhaven National Laboratory's National Synchrotron Light Source

(NSLS). Use of the NSLS was supported by the U.S. Department of Energy, Office of Science, Office of Basic Energy Sciences, under Contract No. DE-AC02-98CH10886. The Physical Properties Measurements System used in the heat capacity measurements was acquired under National Science Foundation Major Research Instrumentation Grant DMR-0923032 (American Recovery and Reinvestment Act award). This research used resources of the National Energy Research Scientific Computing Center, a U.S. Department of Energy Office of Science User Facility supported by the Office of Science of the U.S. Department of Energy under Contract No. DE-AC02-05CH11231.

CHAPTER 5

STRUCTURAL BEHAVIOR IN THE $RX_3(BO_3)_4$ (R= HO, EU, SM, ND, GD; X= FE, AL) SYSTEM UNDER LOW TEMPERATURE

5.1 Introduction

In the search for materials with large magnetoelectric couplings, the $RX_3(BO_3)_4$ (R=rare earth, X=Fe, Al) class has attracted considerable attention in recent years due to the large magnetoelectric effect. As discussed in the previous section, in the case of R= Ho and X= Al, the system remains a stable hexagonal phase R32 down to 5 K, and the electric field induced polarization can be as large as 0.36 $\mu c/cm^2$ [42]. Previous studies suggested an enhanced correlation between the neighboring HoO_6 polyhedra as well as possible Ho site ordering at low temperature [104]. Meanwhile, in the iron borates $RFe_3(BO_3)_4$, a first-order structural phase transition from R32 to $P3_121$ has been found in systems with R= Ho, Tb, Gd and Eu [116]. At the same time, the $RFe_3(BO_3)_4$ system exhibit complex magnetic structure due to the presence of the magnetic open shell R (4f) and Fe (3d) sites. The first magnetic transition (due to Fe ordering) occurs near ~40 K. In the case for R = Ho and Gd, spin reorientation of the Fe moments in the a-b plane occurs at lower temperatures (~ 10 K for Gd and ~5 K for Ho), caused by strong coupling between spins on the R and Fe sites [101,102,103]. We note that in the iron borates, the systems that possess much larger electric field induced polarization are the ones that are stable in the R32 phase, such as in R= Sm and Nd.

To understand the atomic level of mechanism that drives the magnetoelectric effect in the broader $RX_3(BO_3)_4$ class, a systematic study of the structural and magnetic properties has been conducted. High-Resolution single crystal x-ray diffraction experiments have been carried out with samples for R= Ho, Eu Sm, Nd, Gd; X= Fe, Al, to probe the behavior of structural changes between 300 K and 10 K. Single-crystal neutron diffraction data have been obtained for $HoAl_3(BO_3)_4$ to search for possible Ho site ordering at low temperature.

5.2 Experimental Methods

$RX_3(BO_3)_4$ (R= Ho, Eu, Sm, Nd, Gd; X= Fe, Al) single crystals were grown from solution–melts based on bismuth trimolybdate and lithium molybdate. The preparation details can be found in Ref. [117].

Heat capacity measurements on HoAl3(BO3)4 single crystals were carried out with a Physical Property Measurement System (PPMS, Quantum Design) on warming and cooling between 2 K and 300 K to locate transition and determine their nature, utilizing a relaxation method [91]. Addenda measurements (grease without sample) were collected and subtracted from the sample measurements.

Single crystal x-ray diffractions were performed at beamline 15-ID-D at the Advanced Photon Source (APS) at Argonne National Laboratory (ANL). The crystals measured were single phase materials with ~20 μm diameters. A monochromatic focused beam of wavelength 0.41328 Å and size 100 μm× 100 μm was used. The data were collected with a PILATUS 1M detector from 300 K to 10 K. The images were processed with APEX II and APEX III Bruker software for data reduction and with SADABS [118]

for absorption correction. The software XPREP [119] was utilized together with SHELXT [120] and PLATON [121] for structure solution and space group determination and confirmation.

To explore possible magnetic ordering, single crystal neutron diffractions between 5 K and 300K were conducted at beamline HB-1 at High Flux Isotope Reactor (HFIR) at Oak Ridge National Laboratory (ORNL). A beam of wavelength 2.46 Å was used. Powder samples were first explored, in addition oriented single crystal were examined to enhance the signal to noise ratio for specific reflections. The sample was aligned prior to the measurement with the c axis in the horizontal plane. The data were collected in a specific region to search for the forbidden peaks (100) and (101), together with the reference peaks (202) and (003). The exposure time for (100) and (101) peaks was 90 seconds at each temperature, and 15 seconds for the (202) and (003) peaks. The software package GRAFFITI was used for data analysis.

5.3 Results and Discussion

$HoFe_3(BO_3)_4$, $GdFe_3(BO_3)_4$ and $EuFe_3(BO_3)_4$ have been reported to exhibit a structural phase transition at ~ 420 K, 156 K, and 88 K, respectively [116]. This agrees well with our heat capacity measurement, as shown in Figure 5.1.

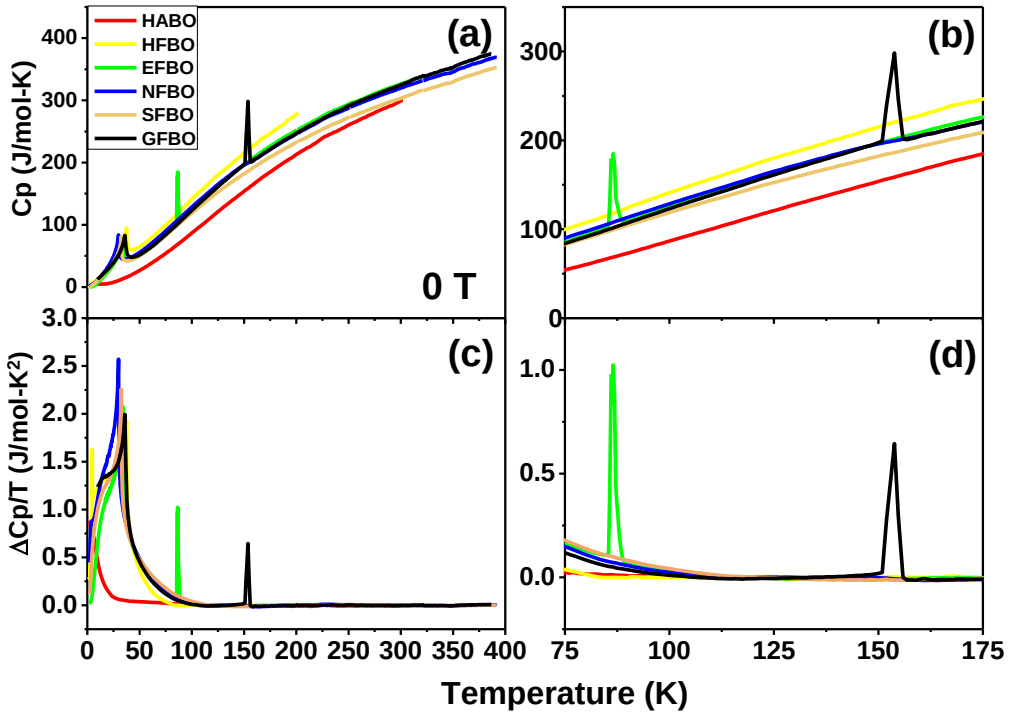

Figure 5.1 (a) Heat Capacity measurement for R=Ho, Eu, Nd, Sm, Gd and A= Al, Fe. (b) Expanded region between 75 and 175 K. (c) C_p/T for the same systems measured; (d) Expanded region for C_p/T between 75 and 175K.

The first order phase transition in systems with R=Gd and Eu is found to be near 156K and 88K, respectively. The transition temperature of the system with R=Ho is not within the measurement range; therefore, no anomaly can be seen. The heat capacity data were then fitted with a double Debye model given by:

$$C_p = 9qNk\left[v\left(\frac{T}{\theta_{D1}}\right)^3\int_0^{\theta_{D1}/T}\frac{x^4e^x}{(e^x-1)^2}dx + (1-v)\left(\frac{T}{\theta_{D2}}\right)^3\int_0^{\theta_{D2}/T}\frac{x^4e^x}{(e^x-1)^2}dx\right] \quad (5.1)$$

The result is shown in Figure 5.2:

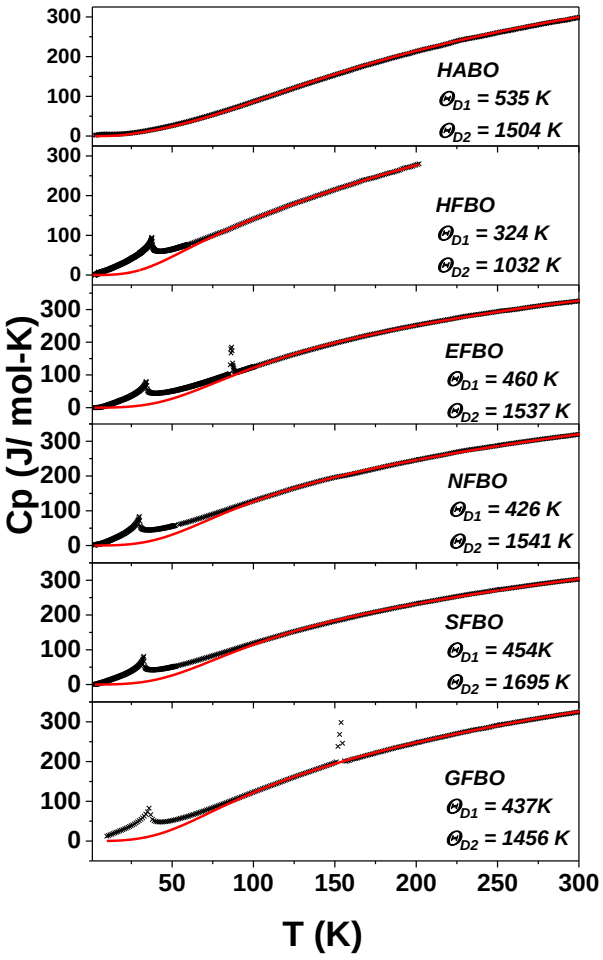

Figure 5.2 Results of the heat capacity measurements fitted with a Debye model.

The refined Debye temperature θ_{D1} (mainly contributed by the rare earth atom) in the HABO system is found to be the largest among all the system been measured. Indicating the significantly higher stiffness than any of the iron containing borates.

The crystal structures were determined by single crystal diffraction measurements. Details can be found in the experimental methods section. The high-temperature phase of the HFBO, GFBO, and EFBO is determined to be R32 and the low-

temperature structure to be $P3_121$. Meanwhile, other systems: $SmFe_3(BO_3)_4$, $NdFe_3(BO_3)_4$ and $HoAl_3(BO_3)_4$ all remain in the R32 space group between 10 K and 300 K. Table 5.1 and 5.2 shows the refinement results for $GdFe_3(BO_3)_4$ at 300 K and 110 K, respectively. The structure determination for other systems are done in the same way, detailed refinement results (at highest and lowest measured temperature) can be found in Appendix A.

Table 5.1 Structural Parameters from $GdFe_3(BO_3)_4$ at 300K

Atoms	**x**	**y**	**z**	**U_{eq} (Å^2)**
Gd	0.0000	0.0000	0.5000	0.00722(9)
Fe	0.11673(7)	0.3333	0.8333	0.00521
O1	0.1874(3)	0.2129(3)	0.6825(3)	0.0081(3)
O2	0.0000	0.4084(4)	1.0000	0.0124(7)
O3	0.0000	0.1438(3)	1.0000	0.0070(4)
B1	0.0000	0.5530(4)	1.0000	0.0062(5)
B2	0.0000	0.0000	1.0000	0.0057(8)

U_{ij}(Gd)	0.00752(10)	0.00752(10)	0.00662(13)	0.000	0.000	0.00376(5)
U_{ij}(Fe)	0.00497(19)	0.0050(2)	0.0057(3)	-0.00015(13)	-0.00008(6)	0.00252(10)
U_{ij}(O1)	0.0077(7)	0.0102(8)	0.0081(8)	-0.0017(7)	-0.0002(6)	0.0057(6)
U_{ij}(O2)	0.0141(13)	0.0081(10)	0.0170(17)	0.0041(6)	0.0083(13)	0.0070(6)
U_{ij}(O3)	0.0082(11)	0.0052(7)	0.0086(11)	0.0008(4)	0.0017(8)	0.0041(5)
U_{ij}(B1)	0.0070(17)	0.0055(10)	0.0067(12)	0.0005(6)	0.0010(12)	0.0035(8)
U_{ij}(B2)	0.0061(13)	0.0061(13)	0.005(2)	0.000	0.000	0.0030(6)

Space Group: R32
a = 9.5526(4) Å
c = 7.5727(3) Å
D_x = 4.662 g/cm^3
Measurement Temperature: 300 K
Crystal Diameter: ~20 μm
Wavelength: 0.41328 Å,
2θ range: 4.2°~40.2°
Flack parameter: 1.04(4)
Absorption Coefficient: 2.9 mm^{-1}
EXTI extinction parameter: 0.01481
Number of Unique Observed Reflections $F_o > 4\sigma(F_o)$: 639
Number of fitting parameters: 36
Amplitude of Max Peak in Final Difference map: 0.56 e/ Å^3 (Gd)
R_1 = 1.3 %, wR_2 = 3.6 %, Goodness of Fit = 0.4

*Atomic displacement parameters U_{ij}(Å^3) are in the order U_{11}, U_{22}, U_{33}, U_{23}, U_{13}, U_{12}

Table 5.2 Structural Parameters from $GdFe_3(BO_3)_4$ at 110K

Atoms	**x**	**y**	**z**	**U_{eq} (Å^2)**
Gd	0.66663(2)	0.66663(2)	1.0000	0.00308(9)
Fe1	1.0000	0.88477(9)	0.6667	0.00273(14)
Fe2	0.33557(5)	0.54988(9)	0.32530(5)	0.00283(13)
O1	0.8123(4)	0.8123(4)	0.5000	0.0046(6)
O2	0.5244(4)	0.6697(2)	0.4933(2)	0.0050(5)
O3	1.0780(4)	1.0780(4)	0.5000	0.0065(6)
O4	0.2703(3)	0.6868(3)	0.4723(3)	0.0058(4)
O5	0.8808(3)	0.6957(3)	0.8198(3)	0.0049(4)
O6	0.2158(3)	0.3624(3)	0.4817(3)	0.0044(4)
O7	0.4614(3)	0.4766(4)	0.1853(4)	0.0045(4)
B1	0.6679(4)	0.6679(4)	0.5000	0.0028(9)
B2	0.4472(5)	0.3274(4)	0.1767(4)	0.0034(6)
B3	1.2219(6)	1.2219(6)	0.5000	0.0038(7)

U_{ij}(Gd) 0.00321(11)	0.00321(11)	0.00291(12)	0.00008(2)	-0.00008(2)	0.00168(7)
U_{ij}(Fe1)0.0029(3)	0.0027(2)	0.0026(3)	0.00001(10)	0.00003(19)	0.00146(14)
U_{ij}(Fe2)0.0030(2)	0.0027(2)	0.0028(2)	0.00011(11)	-0.00001(15)	0.00134(15)
U_{ij}(O1) 0.0042(10)	0.0042(10)	0.0038(13)	0.0009(5)	-0.0009(5)	0.0010(12)
U_{ij}(O2) 0.0040(10)	0.0061(13)	0.0048(11)	-0.0018(9)	-0.0006(7)	0.0023(8)
U_{ij}(O3) 0.0057(10)	0.0057(10)	0.0067(12)	0.0011(5)	-0.0011(5)	0.0018(11)
U_{ij}(O4) 0.0051(9)	0.0069(9)	0.0062(7)	-0.0021(7)	-0.0019(7)	0.0037(8)
U_{ij}(O5) 0.0062(11)	0.0041(10)	0.0044(9)	0.0009(7)	0.0006(8)	0.0025(8)
U_{ij}(O6) 0.0069(10)	0.0032(9)	0.0035(9)	0.0001(7)	0.0006(7)	0.0028(8)
U_{ij}(O7) 0.0056(10)	0.0041(10)	0.0053(9)	0.0002(7)	0.0007(8)	0.0036(8)
U_{ij}(B1) 0.0027(15)	0.0027(15)	0.002(2)	-0.0005(6)	0.0005(6)	0.0005(13)
U_{ij}(B2) 0.0041(13)	0.0029(16)	0.0035(12)	-0.0003(11)	-0.0001(9)	0.0019(11)
U_{ij}(B3) 0.0041(14)	0.0041(14)	0.0034(16)	0.0001(8)	-0.0001(8)	0.0023(17)

Space Group: $P3_121$
a = 9.5454(4) Å c = 7.5615(3) Å
D_x = 4.676 g/cm^3
Measurement Temperature: 110 K
Crystal Diameter: ~20 µm
Wavelength: 0.41328 Å,
2θ range: 2.8°~40.2°
Flack parameter: 1.10(4)
Absorption Coefficient: 2.9 mm^{-1}
EXTI extinction parameter: 0.01243
Number of Unique Observed Reflections $F_o>4\sigma(F_o)$: 1606
Number of fitting parameters: 96
Amplitude of Max Peak in Final Difference map: 0.67e/ Å^3 (O2)
R_1 = 1.9 %, wR_2 = 5.5 %, Goodness of Fit = 1.0

*Atomic displacement parameters U_{ij}(Å^3) are in the order U_{11}, U_{22}, U_{33}, U_{23}, U_{13}, U_{12}

Figure 5.3 shows the lattice parameters extracted from the refinements. Note the right scale is for the HABO system only and the left scale is for the iron borate systems. The a/c ratio for HABO is much larger than that for the iron-based systems, indicating the system is more closely packed in the c direction. Meanwhile, the phase transitions in the GFBO and EFBO (indicated as vertical arrows in Figure 5.3) can be seen clearly (vertical arrow) in the trend of a/c vs. Temperature.

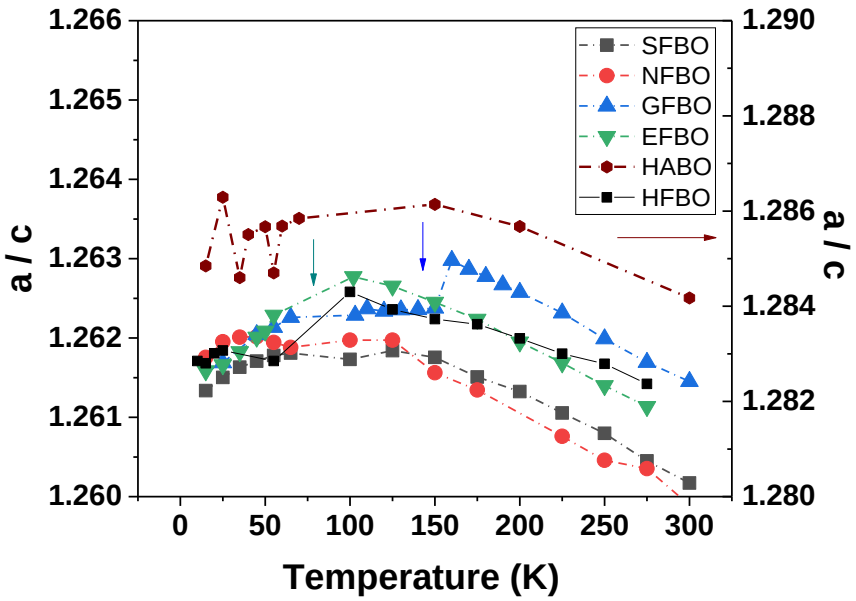

Figure 5.3 a/c ratio vs. Temperature from the single crystal XRD refinements.

The atomic Displacement Parameters (ADPs) of the heavy atoms in the systems with X=Fe haven also been investigated (For HABO system, please refer to Chapter 4), and the results are displayed in Figure 5.4. The anomaly in the NFBO system is probably due to the different setup in the high temperature region and low-temperature region measurements. Debye temperatures extracted from a Debye model are seen to be similar to each other in these systems, suggesting a similar contribution of the rare earth atoms to the structural properties.

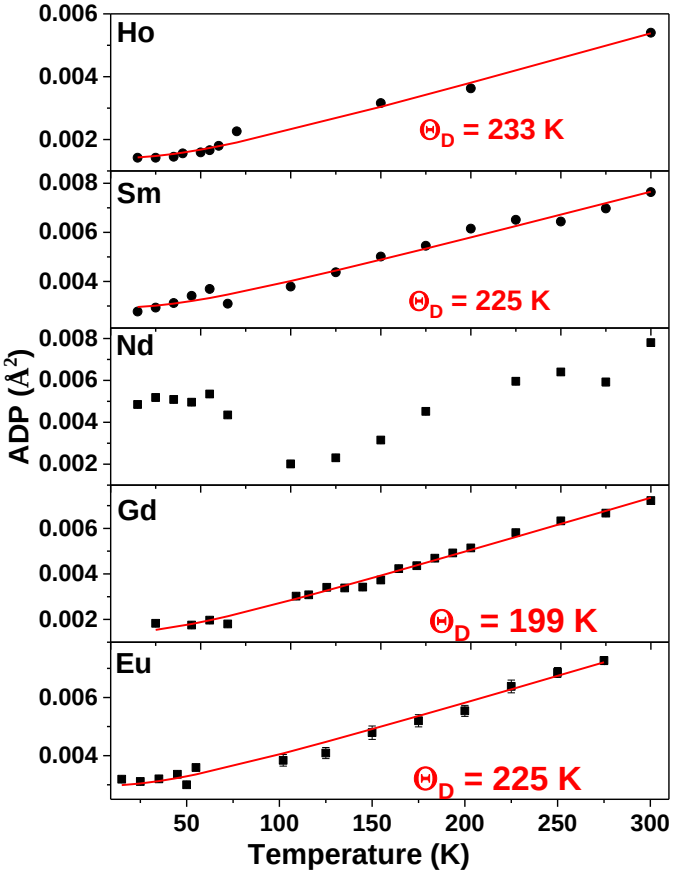

Figure 5.4 Atomic Displacement Parameters (black squares) in the system with X=Fe and the regression line from a Debye model (red).

A more detailed study of the crystal structures is then performed, and the results are shown below. Figure 5.5 shows the structure of $GdFe_3(BO_3)_4$ at 300 K, the Gd and Fe atom both have six neighboring Oxygen atoms. The top and bottom surfaces of the GdO_6 polyhedra are parallel to the ab plane, while in the FeO_6 polyhedra they are slightly tilted. The BO_3 triangles which connect the GdO_6 and FeO_6 polyhedra are parallel to the ab plane.

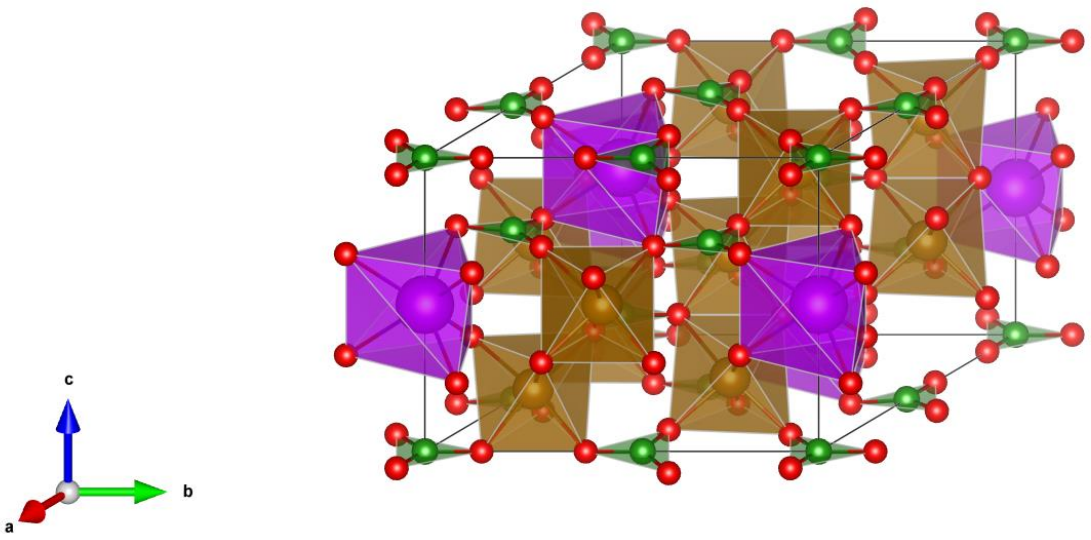

Figure 5.5 Unit cell of $GdFe_3(BO_3)_4$ at 300 K.

When the system goes below 156 K, it can be seen from Table 5.2 that half of the FeO_6 polyhedra become distorted and the BO_3 planes which connect to them tilt with respect to the ab plane. The motions of the atoms are shown in Figure 5.6, to illustrate the idea more clearly, only part of a unit cell is displayed for clarity. The black arrows indicate the direction and amplitude of the movement of each atom; it can be seen that the largest change appears in the BO_3 triangles tilting away from the ab plane.

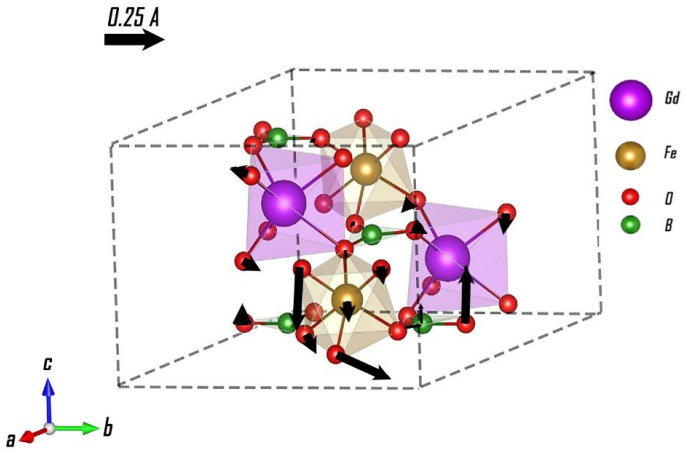

Figure 5.6 Displacement of atoms on going from the fromR32 (high temperature) to $P3_121$ (low temperature) in $GdFe_3(BO_3)_4$.

To Further investigate the structural correlation with the magnetoelectric effect in $RX_3(BO_3)_4$, the relative atomic positions to $SmFe_3(BO_3)_4$ have been studied and are shown in Figure 5.7 for data taken at 25 K. $SmFe_3(BO_3)_4$ is known to have the largest electric field induced polarization at low temperature among the $RFe_3(BO_3)_4$ systems (R= Sm, Eu, Ho, Gd) and does not undergo a structural phase transition. Hence it is a good reference.

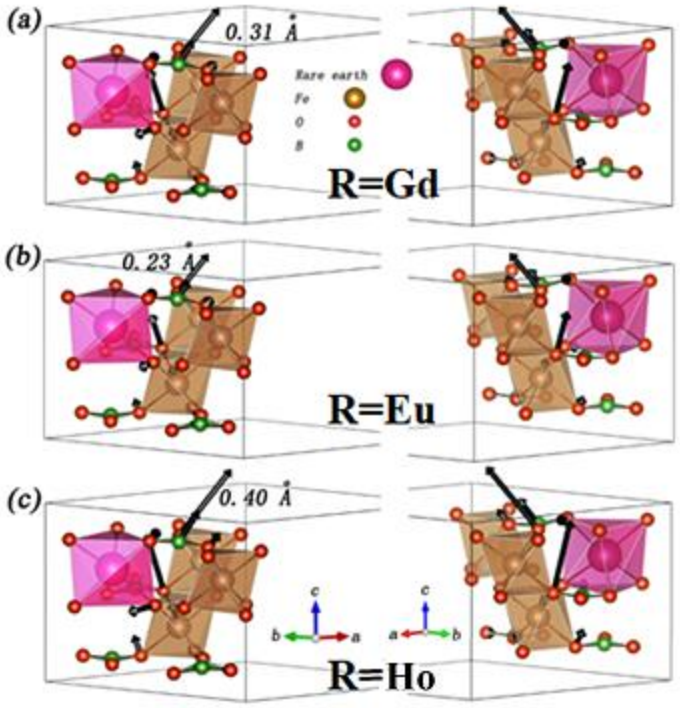

Figure 5.7 Relative atom positions in $RA_3(BO_3)_4$ system respect to SFBO at 25K. R= Gd (a); Eu (b); Ho (c), respectively. The data for Gd, Eu and Ho were taken at 25K.

The arrows reflect the amplitudes and directions of the displacement of specific atoms, and the numbers indicate the value of the longest change. For each structure the arrows are to scale. In the systems with R= Gd, Eu, and Ho, the differences in the atomic positions are seen to be consistent: The largest change in each of the systems is the tilting of the BO_3 plane and the O_3 plane of the FeO_6 polyhedra it connects. The displacement of the same atom is in the same direction in three samples. The tilting angles of the BO_3 with respect to the ab plane for R= Gd, Eu and Ho are 10.9^o, 9.6^o, 12.2^o, respectively. From a structural perspective, it is safe to conclude that the transition to $P3_121$ space is one of the major reasons for the dramatic decrease in the magnetoelectric effect for systems with R= Gd, Eu, and Ho.

As suggested in many references [1], the BO_3 units function as ferroelectric – active groups mainly due to the forming of π electrons. In the case of $RX_3(BO_3)_4$, the tilting of the BO_3 and FeO_6 when a system goes to the lower symmetry structure, may greatly weaken the π bonding of the BO_3 as well as reduce the coupling between the ferroelectric active group BO_3 and the magnetic groups RO_6 and FeO_6. We note that the largest electric field induced polarization of $RX_3(BO_3)_4$ is along the direction within ab plane, the motion described above might be one of the major reasons that greatly reduce the magnetoelectric effect of the system. This is in good agreement with the published results that the electric field induced polarization of $HoFe_3(BO_3)_4$, $GdFe_3(BO_3)_4$ and $EuFe_3(BO_3)_4$ are much lower than systems like $SmFe_3(BO_3)_4$ and $NdFe_3(BO_3)_4$. Meanwhile, for the $HoAl_3(BO_3)_4$ system, our previous research indicated the system is much stiffer along the c axis (see the previous chapter), which would result in much larger couplings between the ferroelectric and magnetic units as suggested by the above theory. In this system the polyhedra and BO_3 planes are less likely to tilt. This is also supported by the experimental result [116] that the magnetoelectric effect in the $HoAl_3(BO_3)_4$ is greater than it in the $SmFe_3(BO_3)_4$ by the factor of ~10. Therefore, we believe that the application of hydrostatic pressure to the $RX_3(BO_3)_4$ systems will mostly like reduce the magnetoelectricity as it distorts the structure and causes a transition to a lower symmetry structure [122]. However, the magnetoelectric effect may be enhanced if the sample was compressed only along the c axis. The magnitude of the uniaxial pressure required will be explored in future work.

It is also necessary to investigate the role of the magnetic ordering on both R site and Fe site (no ordering was found in Al site [see the previous chapter]). Recent studies

showed that the transition metal Fe is not essential to establish large magnetoelectricity in this class of material [41]. At the same time, private communication [104] suggested possible Ho site ordering in $HoAl_3(BO_3)_4$ at low temperature, due to the appearance of a signal at the calculated position of the (100) forbidden peak. In the search for stronger evidence, powder and single crystal neutron diffraction experiments were performed with $HoAl_3(BO_3)_4$ at station NOMAD at SNS, ORNL, and HB-1 at HFIR, ORNL. Figure 5.8 represents the results of the powder diffraction.

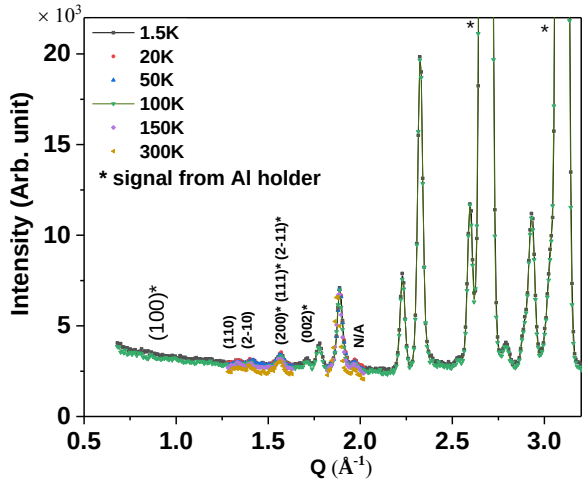

(a)

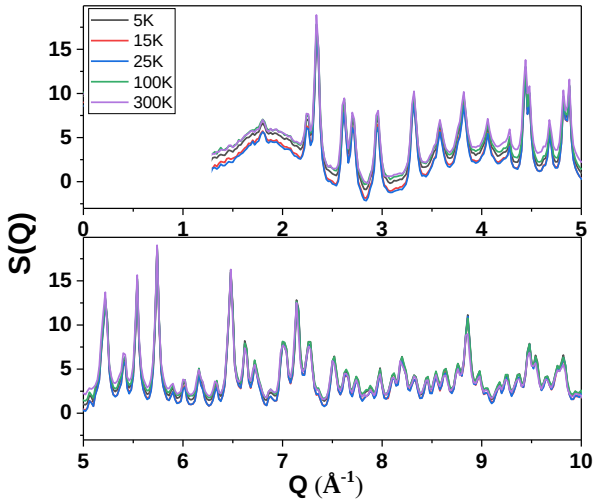

(b)

Figure 5.8 Powder neutron diffraction taken from (a) HB-1 and (b) NOMAD.

For the single crystal measurement, the crystal was first aligned with the c axis in the horizontal plane to find the (202) and (003) peak. The predicted position of the (100) peak was then calculated and scanned along both radial and transversal directions between 5 K to 300 K. The results are shown in Figures 5.6 and 5.7. The powder diffraction measurements between 5 K and 300 K (Figures 5.7 and 5.8) reveal no new peak at low temperature suggesting no magnetic ordering. Single crystal measurements were conducted to enhance the signal to noise ratio and to examine the region around the (100) peak.

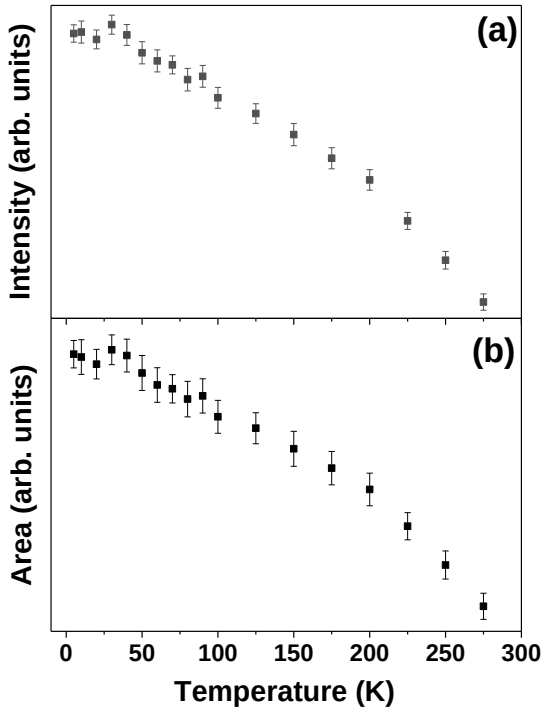

Figure 5.9 (a) Intensity and (b) area for peak (202) vs. temperature.

Single crystal measurements are given in Figures 5.9 and 5.10. Figure 5.9 is the (a) height and (b) area of the peak (202) after fitting the experimental data with a

Gaussian profile, no anomalies can be seen through the entire temperature region. Figure 5.10 is the (a) radial and (b) transverse scan of the region around the calculated position of the (100) forbidden peak. The data seem to be flat between 5 K and 300 K with no obvious appearance or disappearance of a peak. The results from our neutron scattering indicate no evidence for the magnetic ordering in $HoAl_3(BO_3)_4$ involving the a-axis.

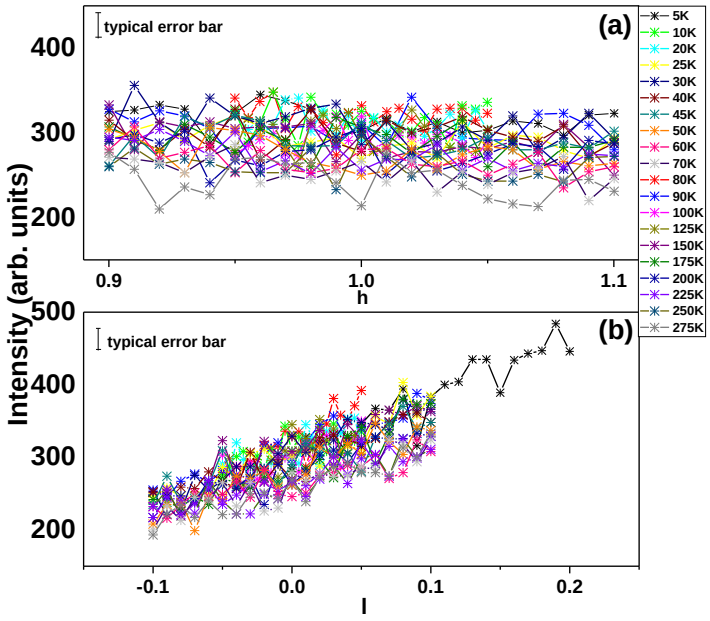

Figure 5.10 (a) Radial and (b) transverse scan of the region around the expected position of the peak (100).

5.4 Summary

In summary, we have conducted single crystal x-ray and neutron diffraction measurements between 5K and 300K with $RX_3(BO_3)_4$ (R= Ho, Eu, Sm, Nd, Gd; X= Fe, Al). The results suggest that the reduced coupling between ferroelectric and magnetic groups caused by the tilt of BO_3 planes and FeO_6 polyhedra is one of the main reasons for the dramatical decrease of the magnetoelectricity in systems with R= Ho, Eu, Gd, and

X=Fe. No magnetic ordering along the a axis was detected in $HoAl_3(BO_3)_4$. It is predicted that the application of pressure along the c axis in $RFe_3(BO_3)_4$ can stabilize the high temperature R32 phase and potentially enhance the electric field induced polarization.

5.5 Acknowledgement

This work is supported by the U.S. Department of Energy (DOE) Grant DE-FG02-07ER46402. Research support for MES and SSW was provided by the U.S. Department of Energy, Basic Energy Sciences, Materials Sciences, and Engineering Division. Synchrotron single crystal x-ray diffraction experiments were performed at *ChemMatCARS (*The University of Chicago, Sector 15), Advanced Photon Source (APS), Argonne National Laboratory (ANL*)*, ChemMatCARS Sector 15 is principally supported by the Divisions of Chemistry (CHE) and Materials Research (DMR), National Science Foundation, under grant number NSF/CHE-1346572. Use of the PILATUS3 X CdTe 1M detector is supported by the National Science Foundation under the grant number NSF/DMR-1531283. Use of the Advanced Photon Source, an Office of Science User Facility operated for the U.S. Department of Energy Office of Science by Argonne National Laboratory, was supported by the U.S. DOE under Contract No. DE-AC02-06CH11357. Single crystal neutron diffraction experiments were performed at HB-1 at the High Flux Isotope Reactor, a DOE Office of Science User Facility operated by the Oak Ridge National Laboratory.

CHAPTER 6

SIZE-DEPENDENT STRUCTURAL PHASE TRANSITIONS IN $SrTiO_3$ NANOPARTICLES

6.1 Introduction

The bulk phase of $SrTiO_3$ (STO) is paraelectric and exhibits a structural phase transition at a pressure, i.e., P^*~6 GPa under hydrostatic pressure. Recently, it was shown that a polar state exists in 10 nm free standing stoichiometric STO nanoparticles under ambient conditions. To explore the size-dependent structural behavior of this system, pressure dependent structural measurements on monodispersed nanoscale $SrTiO_3$ (STO) samples with average diameters of 10 to ~80 nm were conducted to enhance the understanding of the phase diagram of $SrTiO_3$. A robust pressure independent polar structure was detected in the 10 nm sample for pressures up to 13 GPa while a size-dependent cubic to tetragonal transition occurs (at $P = P_c$) for larger particle sizes. The results suggest that the growth of ~10 nm STO particles on substrates with significant lattice mismatch will not alter the polar state of the system for a large range of strain values, possibly enabling device use. Figures and tables in this chapter are from Zhang *et al.*, Applied Physics Letters 111 (5), 052904 (2017).

6.2 Experimental Details

Our monodispersed nanoparticles of $SrTiO_3$ are synthesized by soft chemistry methods. 10 nm $SrTiO_3$ nanoparticles were prepared by employing a hydrothermal technique [123]. More specifically, solutions of titanium bis(ammonium lactate) dihydroxide

(TALH) and strontium hydroxide octahydrate were mixed in a 1: 1 molar ratio with the pH adjusted to 13.5. Hydrazine and oleic acid were added to an autoclave with the precursor solution and heated to 120°C for 24 hrs. The sample was then isolated by centrifugation and washed with water followed by ethanol.

The preparation of 20 nm $SrTiO_3$ nanoparticles was carried out by following the protocol of ref. [124], adding 0.006 mol of $Ti(OC_4H9)_4$ and 0.0072 mol of $Sr(OH)_2$ x $8H_2O$ to n-butylamine (20 mL), and the mixture was allowed to stir for 2 hrs. Subsequently, it was transferred to a Teflon-lined autoclave and run at 180°C for 24 hrs. The resulting white precipitate was isolated and initially washed with diluted formic acid, followed by aliquots of deionized water and ethanol. The washing process was subsequently repeated three times each. The $SrTiO_3$ sample was then allowed to dry overnight at 80ºC.

$SrTiO_3$ nanoparticles of 40 nm diameter were synthesized using a hydrothermal protocol [125]. Specifically, TiO_2 powder (0.18 g, 2.3 mmol) was mixed in a 20 mL aqueous solution of KOH (1.26 g, 23 mmol) to which $Sr(OH)_2 \cdot 8H_2O$ (0.508 g, 2.3 mmol) was also added. The mixture was placed in a 23 mL autoclave and heated to 150°C for 72 hrs. Once the autoclave had cooled to room temperature, the resulting product was isolated, washed with water, and subsequently allowed to dry overnight.

The 83 nm diameter $SrTiO_3$ nanoparticles were generated by methods described in reference [126]. The sample was prepared by grinding powders of strontium oxalate, anatase titanium dioxide, and sodium chloride (1: 1: 20 molar ratio) with a mortar and pestle for 30 min, respectively, until the mixture became homogeneous. Nonylphenyl ether (NP-9 with a molar ratio of 3) was then added to the mixture and further ground

until the mixture was also uniform and homogeneous. The combination was then loaded into a porcelain reaction boat and heated in a tube furnace for 3.5 hr at 820°C. The resulting powder was isolated by centrifugation and subsequently washed with water followed by ethanol to remove any excess salt.

High-pressure X-ray diffraction experiments on samples possessing diameters of 10 nm and 83 nm were conducted at the X17C beamline at the National Synchrotron Light Source (NSLS) at Brookhaven National Laboratory (BNL). A focused beam of dimension 20 μm × 23 μm and a wavelength of 0.4100 Å were used. The sample-detector distance was 287.1 mm. The diffraction patterns were collected with a Rayonix 165 charge coupled device (CCD) detector. Experiments were performed in a diamond-anvil cell (DAC) with stainless steel gaskets and with a 4:1 methanol-ethanol mixture as the pressure transmitting medium. We note that the transition pressures for samples (10 and 83 nm) measured in methanol-ethanol media are below the ~ 10 GPa limit of the hydrostatic behavior of this medium [127]. Several ruby chips were placed in different parts of the chamber for pressure measurements based on the ruby fluorescence wavelengths, and the average reading from three different ruby chips was used to determine the pressure. Four 4000-second scans were collected for each pressure for the 83 nm sample, while two 4000-second scans were collected for the 10 nm sample for each pressure. The 2θ range collected was up to 23º for both data sets.

Experiments performed on the STO particles possessing average diameters of 20 nm and 40 nm were conducted at beamline 13-ID-D at the Advanced Photon Source (APS) at Argonne National Laboratory (ANL). Measurements were conducted with a wavelength of 0.3344 Å and a beam of dimensions 4 μm × 3 μm was used. The sample-

detector distance was 194.2 mm. A 240 μm hole in a rhenium gasket, pre-indented to 50 μm thickness, served as a sample chamber. Ne gas was used as the pressure transmitting medium and gold particles were placed in the DAC for the pressure calibration. At each pressure, 60 s scans were performed and processed. The 2θ range was 0 to 24° for the 20 nm sample, and 0 to 12° for the 40 nm sample, respectively. The variations in the range are a reflection of the corresponding differences in the opening angles of the seats of the different DACs used in the measurements. A sample raw data pattern is given in Figure 6.1. A wedge shape mask was used to integrate the image to ensure the same angular opening for all Bragg peaks.

(a) **(b)**

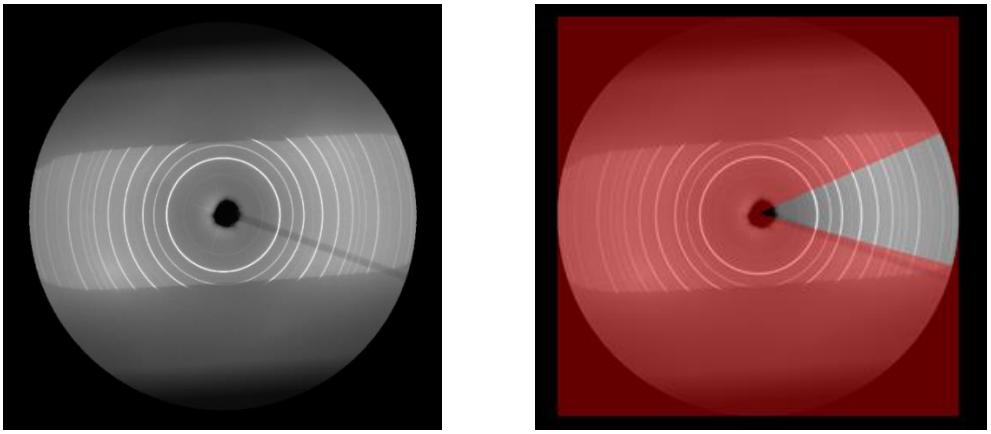

Figure 6.1 (a) Two-dimensional high-pressure XRD data pattern taken at APS beamline 13-ID-D with a CCD detector. The data collected is of high quality with no bright spots from single crystal particles. **(b)** The mask (red) used in data processing to exclude regions of the detector image.

6.3 Results and Discussion

Figure 6.2 shows representative intensity *vs.* 2θ XRD patterns taken at each beamline mentioned above. The transformation to 2θ-space revealed that the peaks from the pattern

of the 83 nm sample illustrated in Figure 6.2(a) are sharper than those from the 20 nm sample, presented in Figure 6.2(b), mainly due to the difference in particle size [128]. The signal from the Ne pressure medium was marked as * in Figure 6.2(b). With the exception of that signal, no new peaks appear over the whole measured pressure range.

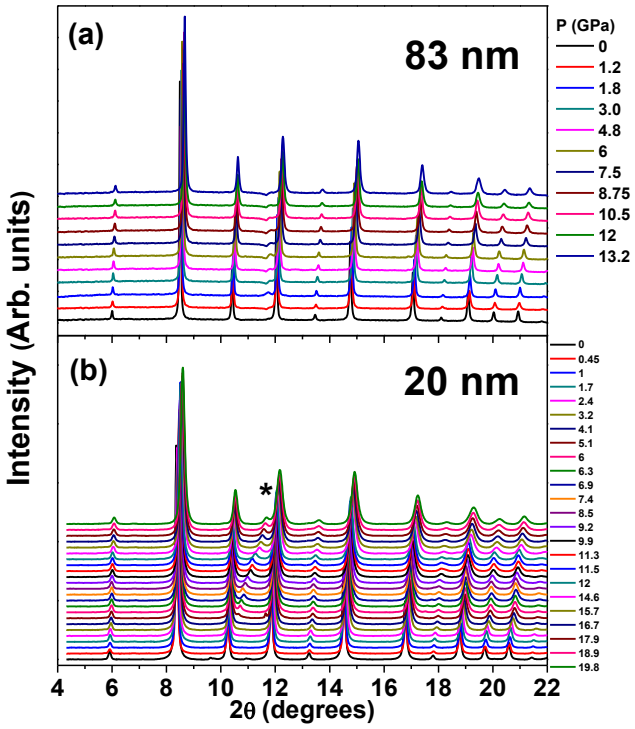

Figure 6.2 High-pressure synchrotron XRD patterns of $SrTiO_3$ with average particle sizes: (a) 83 nm and (b) 20 nm. The 2θ values in (b) have been re-calculated for easy comparison. Peak positions shift systematically to higher 2θ values with increasing pressure. Note that the experimental setups for the two STO samples were different (wavelength and sample-detector distances). Therefore the same Bragg peaks in the two sets of data appear at different 2θ angles. The asterisk indicates peaks of the solid Ne pressure medium in (b).

Rietveld refinements were performed on the collected XRD data to obtain the structural parameters of the STO particles. The profiles of the refinement (data fit) under

ambient pressure for the 83 nm and 20 nm sample are shown in Figure 6.3(a) and Figure 6.3(b). The 2θ values of 6.3(b) have been re-calculated for easy comparison. A high χ^2 value of the refinement in Figure 6.3(b) was obtained mainly due to the background subtracted prior to refinement (see ref. [82]). Typical χ^2 values for 10 nm and 83 nm STO are ~ 0.2 over the pressure range measured.

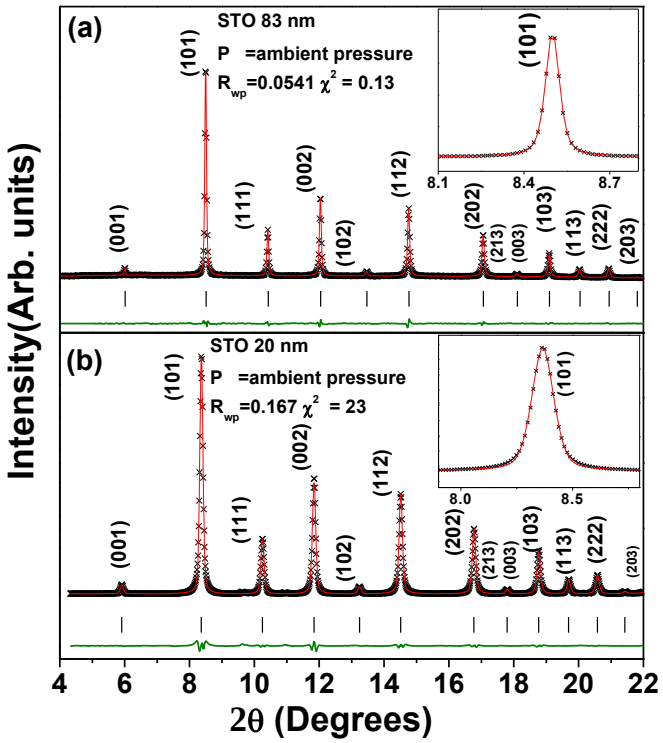

Figure 6.3 Rietveld refinement results at ambient pressure for (a) 83 nm and (b) 20 nm STO. The observed (crosses), calculated (solid line), and difference (bottom line) patterns are shown. The vertical bars show the peak positions of the refined model. The 2θ values of (b) have been re-calculated for easy comparison. The insets show an expanded region for the (101) peak.

In order to better understand the correlation between pressure and particle size, a third order equation of state (EOS) fits using the Birch-Murnaghan (BM) equation

$P(V) = \frac{3B_0}{2}\left[(\frac{V_0}{V})^{\frac{7}{3}} - (\frac{V_0}{V})^{\frac{5}{3}}\right]\left\{1 + \frac{3}{4}(B_0' - 4)\left[(\frac{V_0}{V})^{\frac{2}{3}} - 1\right]\right\}$ were performed with the results presented in Figure 6.4, where B_0 is the bulk modulus and B_0' is the derivative with respect to pressure. Figure 6,4(a) highlights the fitting curve when using the 3rd order BM-EOS between 0 and 12 GPa, showing that data points were clearly off the curve at a certain pressure [129], indicated as P_c. The residual (difference between the fit and the data) shown as the lower plot in each panel reveals a sudden change near 6-7 GPa. The bulk modulus B_0 and its pressure derivative B_0' obtained from the fit are $B_0 = 157 \pm 7$ GPa and $B_0' = 9.1 \pm 2.9$, respectively. B_0' is slightly out of the normal range, with typical values corresponding to B_0' between 2 and 8 [105]. The value of B_0 can be compared with the corresponding value of other well-studied perovskites, which are listed in Table 6.1.

Table 6.1 Bulk Modulus Values

Sample	B (GPa)	B'
$PrTiO_3$ (cubic)	195(3) [130]	4
	237(4) [131]	4.5
	141(5) [132]	4
$PrTiO_3$ (Tetragonal)	100(3) [130]	4
	107(3) [131]	5
	104(4) [132]	4
$BaTiO_3$ (cubic)	162 [133]	
(Tetragonal)	141 [134]	
$EuTiO_3$ (cubic)	180.1 [135]	
(Tetragonal)	190.3(4) [135]	
$SrTiO_3$ (cubic)	176(3) [136]	4.4 (8)
(Tetragonal)	225(6) [137]	4.7 (4)
$SrTiO_3$ nano- particles (This Work)		
(10 nm)	157	9.1
(83 nm)	148	8.9

It can be observed that although the 83 nm sample possesses a structural transition near 6 GPa, which is similar to the bulk value, the bulk modulus is significantly smaller than that of the bulk sample (~220 GPa). (The deviation at 6 GPa is more evident in the diffraction peak widths, Figure 6.4) This result can be caused by the size effects associated with the nanoscale particles. The expansion of the STO lattice with reduced size suggests a lattice softening with size reduction, consistent with the B_0 reduction. The expansion is due to the reduction of the hybridization of the oxygen *p* and titanium *d* bands (see previous work in Ref. [77] supplementary text). This behavior is also observed in Ref. [138], in which the decrease in the electrostatic force caused by the valence reduction of Ce ions and an increase in the ionicity of Ti ions were argued to be the reason for the observed lattice expansions in CeO_{2-x} and $BaTiO_3$ nanoparticles, respectively. A similar analysis was not conducted with the 40 nm sample, due to the lower 2θ range with that data set, as mentioned in the experimental details. By investigating the data associated with the 20 nm sample, as shown in Figure 6.3(b), a deviation (transition) is observed but is shifted towards a lower pressure value of ~2.5 GPa. A 3rd order BM-EOS over the entire pressure range yields to a B_0' value of > 30, which is apparently not correct and strongly suggests a structural-phase transition during the compression. Looking at the residual curve, we also note that there is a possible additional transition near ~7 GPa.

Figure 6.3(c) presents the 3rd order BM-EOS fit for the 10 nm STO sample. The experimental data can be well described with a single first order equation in the whole pressure range (no deviations in the residual curves), which is quite different from the 83 nm sample. The good agreement of the data with the fitting curve suggests no structural

transition in this pressure range. The pressure derivative B_0' extracted from the refinement is 8.9 ± 5.6 which is at the upper limit of results for standard oxides. This enhancement is typical of anisotropic compression [139]. This behavior is in good agreement with our previously reported work [87] that demonstrated that the 10 nm STO sample is polar over a wide temperature range. The peak widths reveal the structural changes with pressure more clearly.

To more clearly view the pressure-dependent structural change, we further investigated the XRD pattern by examining the change in peak widths as a function of pressure (looking for splitting/broadening caused by structural transitions to low-symmetry phases) [135]. The results are presented in Figure 6.4. The basic idea is that when the sample undergoes a transition from the cubic to the tetragonal phase, some of the specific peaks in the XRD pattern will split (for example the (002) and (112) peaks). Although the splitting can be small under many circumstances, it can be well detected when studying the peak width *vs.* the pressure.

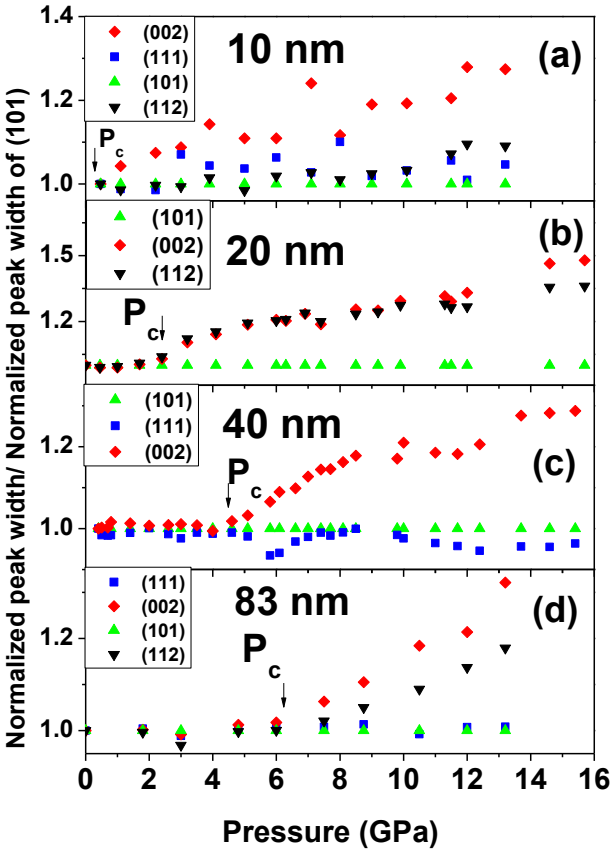

Figure 6.4 Specified peak widths vs. pressure for the STO system extracted from the diffraction patterns for particle sizes (a) 10 nm (b) 20 nm, (c) 40 nm, and (d) 83 nm, respectively. There is a clear shift of the transition pressure (P_c) towards the lower pressure region with decreasing particle size. The widths have been normalized (see text).

In this work, first we fit some chosen peaks with a Lorentzian profile, and then retrieved the corresponding peak width *vs.* pressure curve. Original data can be found in the Supplementary Information section. To visualize the changes clearly, we normalized the peak width as $\varpi_{nor} = {\varpi/\varpi_0}\Big/{\varpi^{(101)}/\varpi_0^{(101)}}$, in which ϖ_{nor} is the normalized peak width; ϖ is the original peak width; ϖ_0 is the original peak width at lowest pressure;

$\varpi^{(101)}$ is the width of the (101)peak, which will not spilt during the cubic-tetragonal transition, and $\varpi_0^{(101)}$ is the width of the peak (101) at lowest pressure. The results are displayed in Figure 6.4. Figure 6.4(a) includes the peak width *vs.* pressure data for the (112), (002), (111), and (101) peaks, which can be attributed to the 10 nm STO sample. The 10 nm sample yields no obvious trends which can be observed through the entire pressure range of all of these four peaks. The (112) and (002) peaks exhibit an almost linear response between ambient pressure and 13 GPa, suggesting that the sample structure is stable in this pressure range. However, as we increased the STO particle size, there are clear deviations in the graphs (Figures 6.4(b), 6.4(c) and 6.4(d)). For example, for the 20 nm sample, all four peaks maintain almost the same width ratio up to ~2.5 GPa, but a sudden increase is observed near ~2.5 GPa in the (112) and (002) peaks, which is likely related to the structural transition from the cubic to the tetragonal phase [135]. This finding serves as strong evidence that the 20 nm STO has given rise to a pressure-induced phase transition at ~2.5 GPa. As the particle size is increased, the transition pressure is seen to shift towards the higher-pressure region. In Figure 3(c), the transition pressure is found to be ~4.5 GPa for the 40 nm sample, and in Figure 3(d), the pressure is noted to be ~6.0 GPa for the 83 nm sample.

Additional information can be gained by fitting the XRD data to a tetragonal model. The pressure dependent splitting of the a and c lattice parameters were extracted for the 83 and 20 nm samples and was seen to follow the same trend found in the peak width variation (See Figure 6.5). The detailed atomic configuration in the tetragonal phase will be explored in future neutron diffraction measurements under pressure.

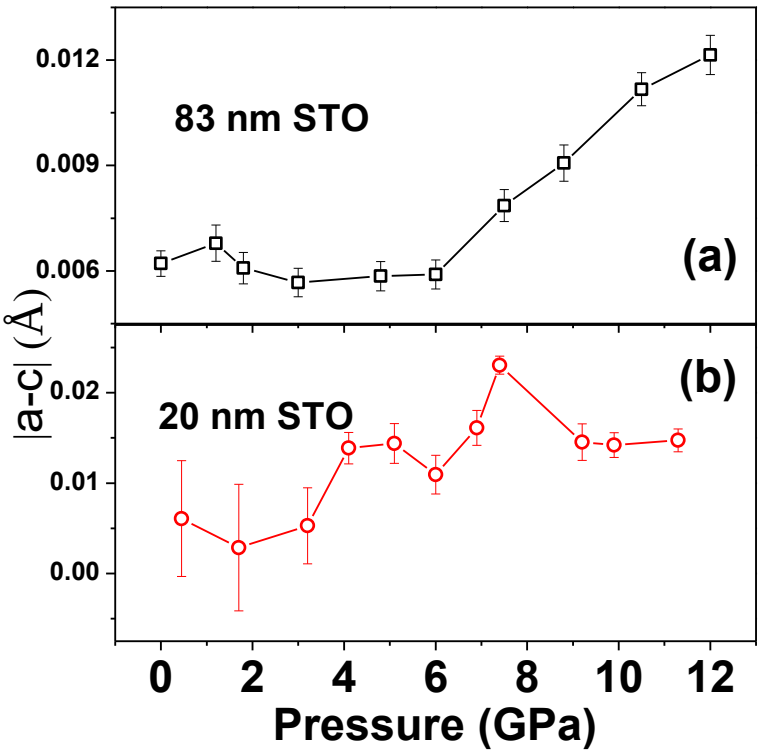

Figure 6.5 (a) The magnitude of the difference between a and c lattice parameters (from Le Bail fit) of 83 nm STO using the P4mm tetragonal space group. Separation between a and c occurs above 6 GPa. (b) The corresponding magnitude of the difference between the a and c lattice parameters of 20 nm STO for the P4mm tetragonal space group. The splitting becomes significant above ~2.5 GPa. The detailed nature and atomic arrangement in the tetragonal state can be determined by neutron powder diffraction measurements in future work.

We further investigated this transition pressure as a function of different particle sizes, based on the theory developed by Chen et al. [140], correlating pressure-induced changes with size-induced changes in the transition temperature. The relationship between the transition pressure P_{cj} and the particle size K_j is found to be related by the following expression: $P_{cj} \sim P_{cb}\left(A - \frac{B}{K_j}\right)$, where P_{cb} is the transition pressure of bulk

sample, and A and B are constants determined by the nature of the chemical bonding inside the sample.

The theory suggests a linear correlation between the transition pressure and the inverse of the particle size. Examination of Figure 6.6(b) reveals that this prediction holds for this system. These combined results are found in Figures 6.5 and 6.6 and give corroborative evidence for our previous conclusion that the 20 nm, 40 nm, and 83 nm STO samples exhibit a pressure-induced phase transition whose onset appears to decrease with decreasing particle size, whereas the 10 nm STO is stable (in a polar phase) between ambient pressure and 13 GPa. The structural phase diagram under pressure is presented as Figure 6.6(a). We note that other oxide systems exhibit even more complex phase changes with size and pressure such as TiO_2 [141]. However, the stabilization of a polar state in STO nanoparticles is a new feature of this work. Detailed modeling of the nanoparticles systems by utilizing density functional methods may assist in determining the microscopic level mechanism for the phase change with particle size and pressure and will be the topic of future work.

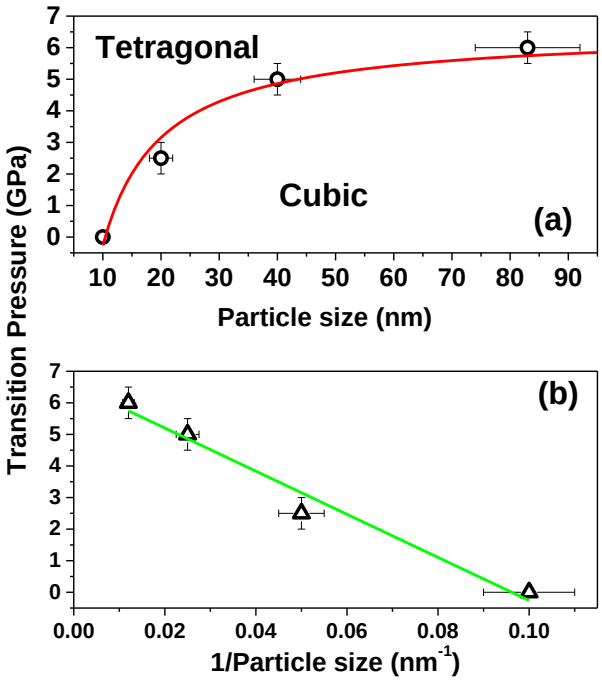

Figure 6.6 Phase diagram of $SrTiO_3$ nanoparticles, with transition pressure *vs.* (a) particle size and (b) inverse of the particle size. The solid lines are fits based on the simple model results in Ref. [140] (see text).

This result provides insight into the possible application of STO nanoparticles of various sizes in data storage devices. We note that in the BaTiO3 system, isotropic pressure suppresses the polar state in bulk samples as pressure increases up to 10 GPa, leading to the cubic state for higher pressures [142]. In general, anisotropic pressure (strain) enhances the polar phase in $ATiO_3$ systems, as mentioned above. We note that polar nano-scale STO particles can be synthesized from simple wet chemical methods. One can grow or deposit the nanoparticles (of diameter ~ 10 nm) onto substrates with significant lattice mismatch without appreciably altering the polar state.

The application of an electric field to orient the particles followed by annealing may possibly produce a high-density nanoscale array of nano-ferroelectric materials. By

controllably depositing the particles onto a densely patterned surface, high capacity storage may be enabled.

In summary, we have conducted pressure-dependent structural measurements (up to ~20 GPa) of monodispersed nanoscale samples with average diameters of 10 nm, 20 nm, 40 nm, and 83 nm, respectively. The transition pressure was found to decrease with decreasing particle size, and a robust pressure-independent structure of the 10 nm sample was observed. The results suggest that growth of STO nanoparticles (with near 10 nm diameter) onto substrates which do not match the underlying STO lattice will not alter the polar state of the system for a large range of strain values, thereby enabling more widespread device use.

6.4 Acknowledgement

This work is supported by the U.S. Department of Energy (DOE) Grant DE-FG02-07ER46402. Research support for MES and SSW was provided by the U.S. Department of Energy, Basic Energy Sciences, Materials Sciences and Engineering Division. Synchrotron powder x-ray diffraction experiments were performed at Brookhaven National Laboratory's National Synchrotron Light Source (NSLS) and Advanced Photon Source (APS). Use of the NSLS was supported by the U.S. Department of Energy, Office of Science, Office of Basic Energy Sciences, under Contract No. DE-AC02-98CH10886. This research used resources of the Advanced Photon Source, a U.S. Department of Energy Office of Science User Facility operated for the DOE Office of Science by Argonne National Laboratory under Contract No. DE-AC02-06CH11357.

CHAPTER 7

FERROELECTRICITY IN MILLED $BaTiO_3$ NANOPARTICLES

7.1 Introduction

Nanoparticles often possess unique electronic, optic and magnetic properties compared to their bulk form (see previous chapters) [143]. Ferroelectric nanoparticles have very promising potential usage in many areas like data storage, medicinal imaging, targeted drug delivery… etc. [144]. Nanoparticles can be prepared by chemical as well as mechanical methods. However most materials been studied in the literature recently (see the introduction chapter) are chemically synthesized. A very important reason is to avoid many serious phenomena accompanied with the milling procedure during the mechanical preparation, such as temperature effect [145], contamination [146], amorphization [147], mechanochemical equilibrium [148], agglomeration and aggregation [148], as well as surfactants absorption [149]. Despite the disadvantages mentioned above, milling can still be very useful especially in preparing (ferro)electric nanoparticles because of the large surface strain usually associated with the milling process [150], provided that one can understand the final structure of the nanoparticles prepared by this method. Moreover, milling is used because it is a straightforward way to make nanoparticles. Milling for long times can produce materials with narrow size distributions.

Nano BTO is reported have of a linearly ordered and monodomain polarization state at nanometre dimensions, as well as room-temperature polarization switching down to particles size ~5 nm [3].

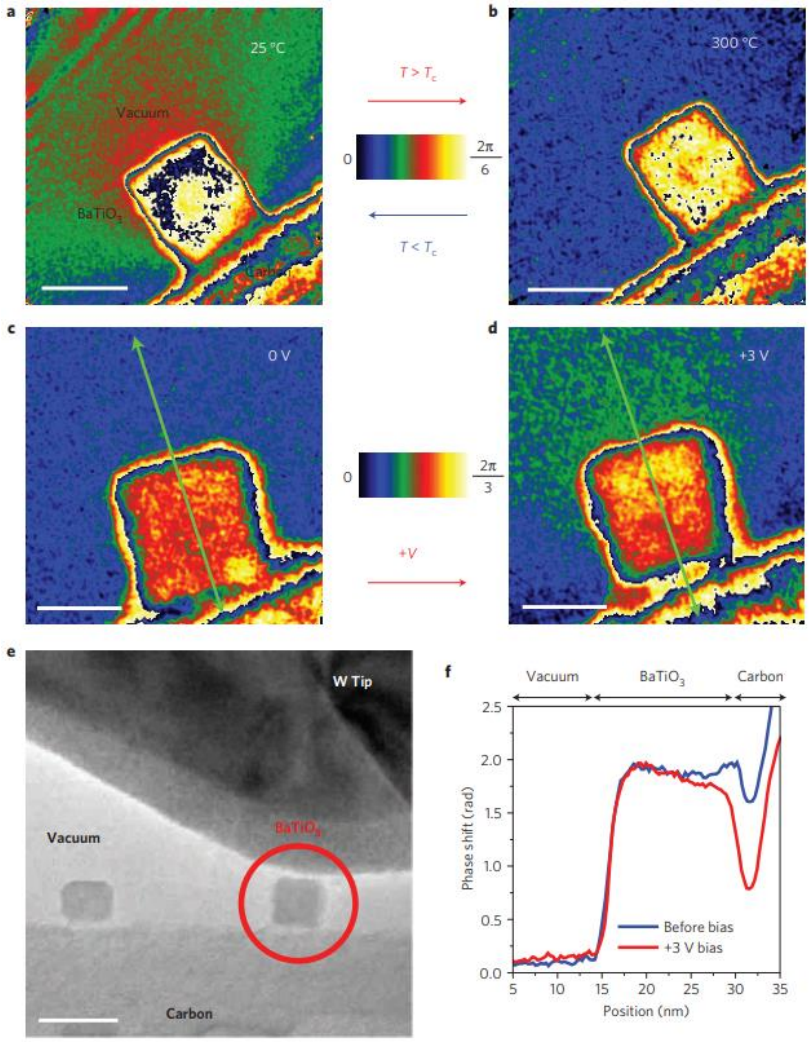

Figure 7.1 Direct polarization imaging of individual BaTiO3 nanocubes with off-axis electron holography
Source: [3]

As has been mentioned earlier [76], a large electric polarization (~ 3 times larger than the bulk sample) has been found in the $BaTiO_3$ (BTO) nanoparticles prepared by mechanical ball milling. The mechanism in this system remains unsolved. This work aims to understand the structure of the final particles prepared in Ref. [76] to ensure possible industry application in the future.

7.2 Sample Preparation and Experimental Methods

The nanoparticles are prepared by mechanical ball milling the commercial bulk $BaTiO_3$ for 25 hours, with oleic acid as a surfactant to prevent particle agglomeration. The ratio of the BTO and oleic acid used was 1:1. The final particle size is determined by TEM imaging as well as XRD refinement. In this work, the particle diameter from milling is determined to be 9 ± 2 nm (Sherrer method). The sample is denoted as ’10 nm as prepared’ BTO nanoparticles in this work. Some of the ’10 nm BTO as prepared’ sample is then dried and washed with alcohol according to Ref. [76]. These particles will be denoted as ’10 nm washed’ BTO in this work. BTO nanoparticles with 700 nm and 50 nm (70 ± 3 nm (Sherrer method)).as the dimension were purchased commercially from Alfa Aesar. The 700 nm BTO is considered to be our bulk sample from our preliminary study. Therefore it will be denoted as ‘700 nm’ or just ‘bulk’ BTO in the following text. Barium Oleate measured in this work is from our collaborator Dr. Evan’s group at the Air Force Research Laboratory, at Wright-Patterson Air Force Base.

Table 7.1 Lattice Parameters from Rietveld Refinement

Sample Type	**Extracted Diameter (**nm**)**	**a (**Å)	**c (**Å))
700 nm sample		3.9941(4)	4.0320(1)
50 nm sample	70(3)	4.0052(1)	4.0268(2) Å
10 nm as prepared	9(2)	4.009(5)	4.02(1)
10 nm washed 13(2)		4.018(5)	4.021(5)

The laboratory X-ray diffraction studies are conducted with a Philips Empyrean X-ray diffractometer with a Copper x-ray tube at Otto H. York Center for Environmental

Engineering and Science, NJIT. Samples have been measured is 10 nm washed BTO as well as the Barium oleate.

The Raman Spectroscopy were measured with a Thermo Fisher DXR Raman Microscopy at Otto H. York Center for Environmental Engineering and Science, NJIT using a 532 nm laser and 10x objective.

The X-ray absorption fine structure measurements with 10 nm as prepared, 10 nm washed, 50 nm and 700 nm BTO are done at beamline 8-ID (ISS) at NSLS 2, BNL.

The PDF analysis with 10 nm washed BTO, and Barium oleate uses the resource at beamline 28-ID-2 (XPD), NSLS 2, BNL, with a wavelength of 0.2366 Å. The PDF analysis with 50 nm and 700 nm BTO are measured at beamline X17A, at NSLS, BNL.

7.3 Results and Discussion

The results from Raman spectroscopy is shown in Figure 7.2 and 7.3. Figure 7.2 is from room temperature Raman spectroscopy for the 10 nm as prepared, 50 nm and 700 nm bulk-like samples. For the 10 nm sample, there is an additional peak near 190 cm^{-1} indicating a reduction in symmetry. This feature becomes enhanced in the rhombohedral phase in the bulk samples (below ~ 183 K) but is evident in the nanoparticles at room temperature. This peak corresponds to an A1 (TO) mode in the tetragonal system as seen by Marssi *et al.* in Ref. [151].

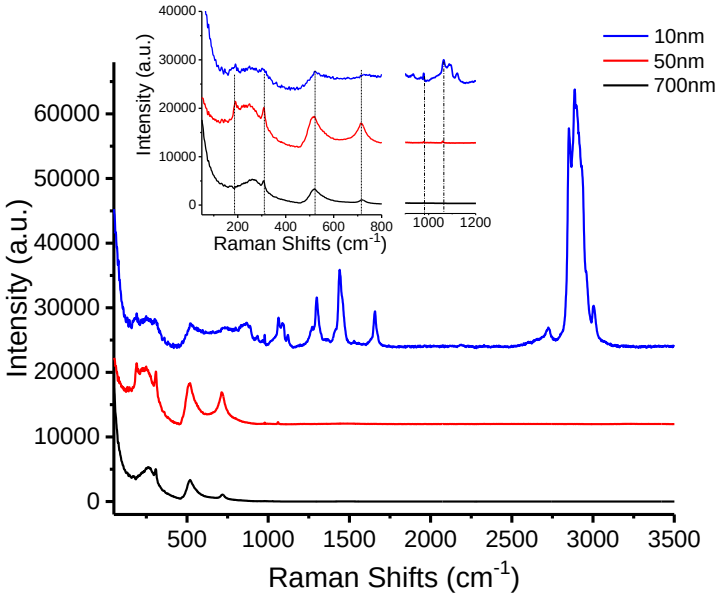

Figure 7.2 Room temperature Raman measurements for 10 nm as prepared (blue), 50 nm (red) and 700 nm (black) BTO.

Meanwhile, it can also be seen that there are additional peaks in the spectra of the 10 nm as prepared BTO which do not exist in the other BTO samples, the high intensity of these features indicates the presence of another substance. The use of the oleate acid during the milling makes it a possible source. Therefore the Raman spectroscopy of oleate acid from Ref. [152] is compared with, and the result is shown in Figure 7.3.

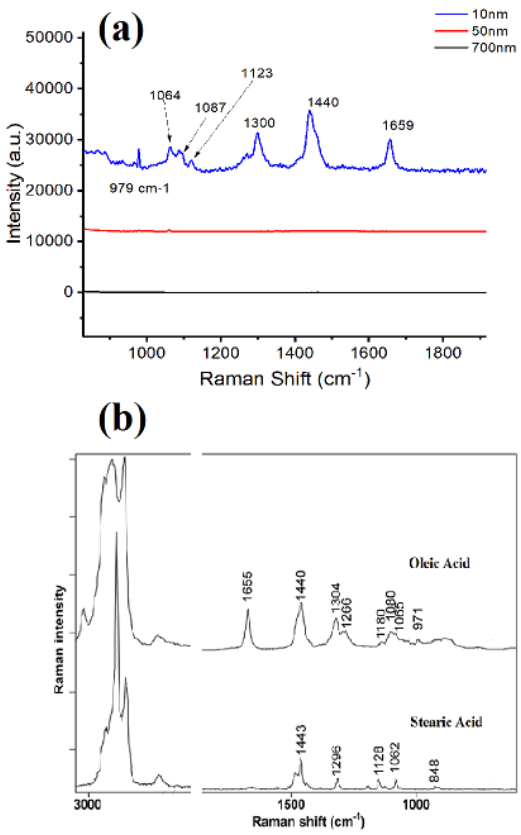

Figure 7.3 (a) Expanded region from Figure 7.1 where the additional peaks exist. (b) Raman spectra of oleate acid in Ref. [152], note that the x-axis is reversed (high to low frequency).
Source: (b) [152].

From Figure 7.3 it is very clear that the additional peaks in the spectra of the 10 nm as prepared BTO match well with the signal of the oleate acid. Therefore, it is safe to conclude that oleate acid is present in the 10 nm as prepared BTO sample prior to the alcohol wash.

The 10 nm as prepared BTO is then washed by alcohol repeatedly with the aim of removing the oleate acid as well as the byproducts of the ball milling, such as Ti-compound and Barium oleate. Reference [76] suggests no existence of the Barium oleate in the 10 nm BTO after the alcohol wash, but the surface strain of the nanoparticles (possibly caused by Barium oleate coating) remain still. To verify that point, synchrotron

XAFS, and laboratory XRD measurements have been conducted and the results are shown in Figures 7.3 and 7.4.

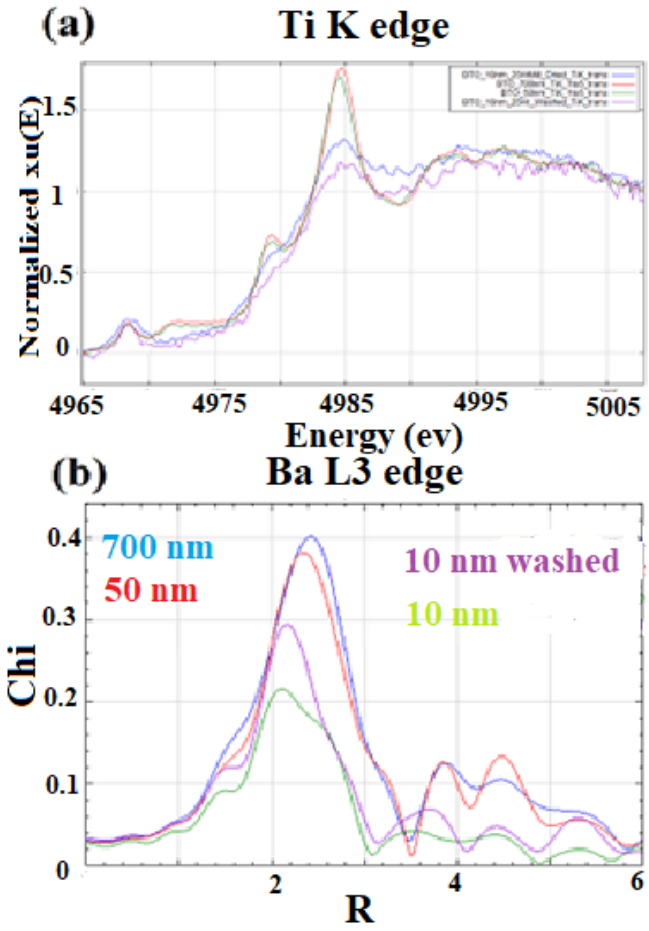

Figure 7.3 XAFS measurements at (a) Ti K edge XANES and (b) Ba L3 edge XAFS structure function for 700 nm (blue), 50 nm (red), 10 nm as prepared (green) and 10 nm washed (purple) BTO.

Figure 7.4 (a) shows the Ti K-Edge x-ray absorption spectra for the 700 and 50 nm samples compared to the 10 nm as prepared, and 10 nm washed sample. Note that the low energy feature near 4967 eV is similar in the 700 nm, 50 nm and 10 nm washed sample. The feature is broader in the 10 nm as prepared sample indicating that this sample has Ti impurities. Note that the strong peak in the 50 and 700 nm samples near

4985 eV is converted to a broad feature in the 10 nm samples due to the reduced long-range structural order in the nanophase. The difference in the unwashed sample (low energy peak) suggests a separate Ti containing impurity unattached to the nanoscale BTO nanoparticles. Figure 7.4 (b) is the Barium L3 XAFS structure function showing the main Ba-O peak. The 700 nm, 50 nm and washed 10 nm sample have a similar shape while the unwashed sample has double structure suggesting multiple components. The difference in the unwashed sample suggests a separate Ba containing impurity unattached to the samples.

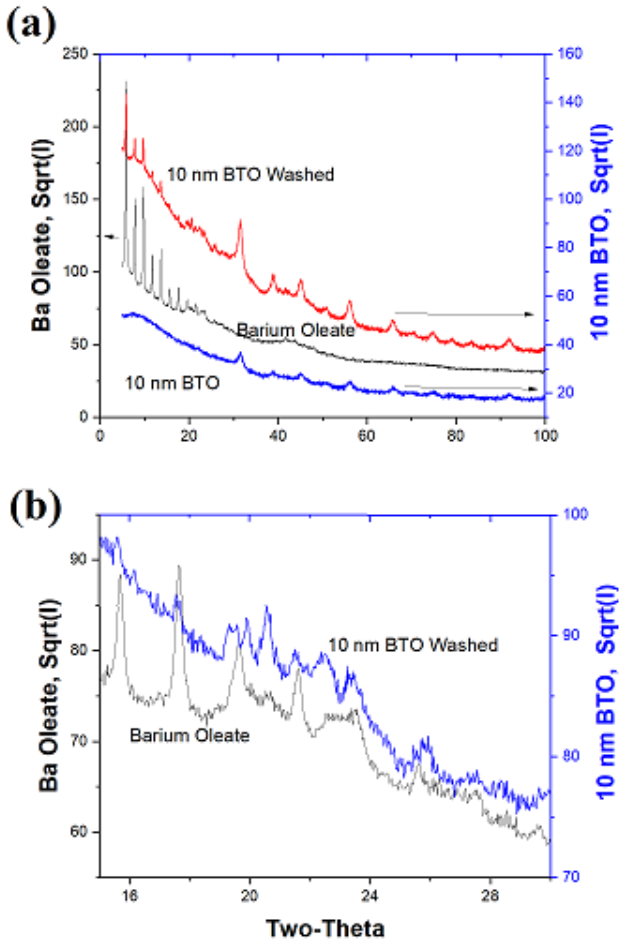

Figure 7.5 (a) XRD measurements of the 10 nm washed BTO and Barium oleate. (b) Zoomed region between 15° to 30° in 2-Θ.

Figure 7.5 is the results of laboratory XRD measurements. The additional features identified in Figure 7.5 (a) are compared with the diffraction pattern of Barium oleate, and the result is shown in Figure 7.5 (b). The positions of these peaks match well with the peaks of Barium oleate, but the intensities of several peaks are off. This could be because of the noise level of the instrument or could also be that the extra compound in the sample is not exactly barium oleate but a very similar derivative of this structure. Additional measurements are needed to understand the full structure of the 10 nm washed BTO sample.

X-ray PDF measurements were conducted to investigate this matter further. The result is displayed in Figure 7.6.

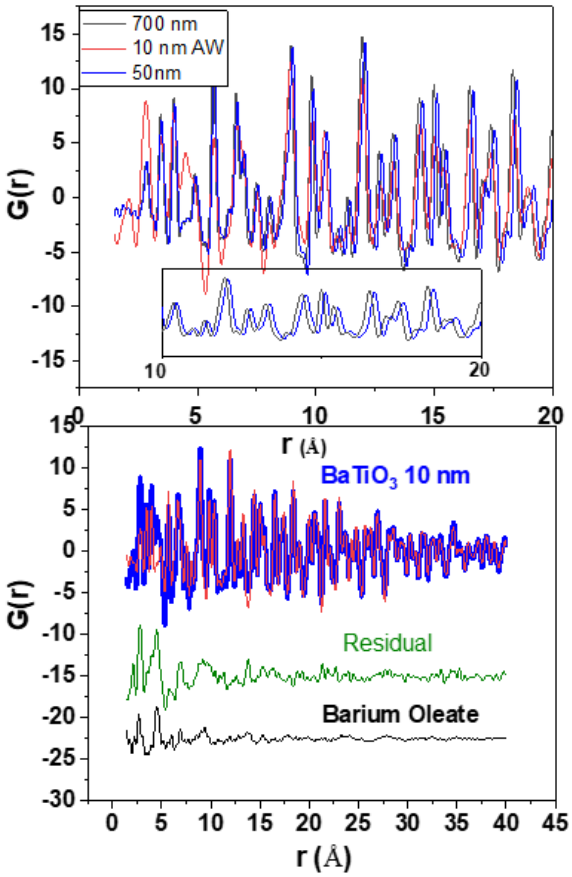

Figure 7.6 (a) G(r) profile for the 700 nm (black), 10 nm washed (red) and 50 nm (blue) BTO, the inset is a zoomed region between 10 to 20 Å. (b) PDF profile (red), refinement

(blue) and the residual (green) for the 10 nm washed BTO, the PDF profile of Barium oleate (black) is shown for comparison.

Figure 7.6 (a) shows the anomalous lattice expansion in the 50 nm BTO nanoparticle evidenced by many references [74], as the peaks shift to higher r regions compared with the signal of the 700 nm BTO. However, the 10 nm washed BTO is more like bulk than nanoparticles as every specific peak remains at almost the same position as in the 700 nm sample. Meanwhile, while the 10 nm washed BTO seems to have the same structure with the 700 nm sample in the high-r regions, additional features are seen in the low-r area. This strongly suggests the existence of another compound which lacks long-range order. To get a better understanding, refinement with PDFgui [89] were conducted by using the data between 10 to 20 Å. The refined parameters are then used to calculate the G(r) below 10 Å so that the residual in the entire data range could be acquired, The result is shown in Figure 7.6 (b). It is very clear that the residual profile matches well with the G(r) of the Barium oleate. This result suggests the presence of Barium oleate in the 10 nm BTO even after been washed with alcohol. The exact form of the Barium oleate is not known. The small signal of this contributon suggests that it is possibly a coating on the nanoparticles.

Meanwhile, the previous statement that the 10 nm washed BTO is more like bulk than nanoscale BTO does seem to be interesting and surprising. To verify the point, systematic temperature dependent PDF refinements are done with the 700 nm, 50 nm and 10 nm washed BTO between 100 K and 500 K. The extracted lattice ratio is shown in Figure 7.7.

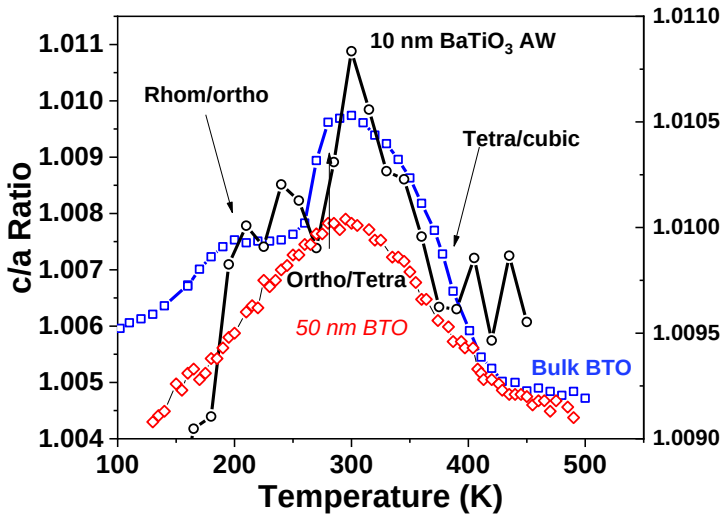

Figure 7.7 c/a ratio of the 700 nm (blue), 50 nm (red) and 10 nm washed (black) BTO nanoparticles.

From the results in Figure 7.7, it can be seen that the cubic to tetragonal transition occurs in all samples at approximately the same temperature [153]. The washed 10 nm sample has an extremely sharp transition near the bulk values. The behavior of the c/a ratio of the 10 nm washed BTO is indeed more like bulk BTO than that of the 50 nm sample.

In summary, BTO nanoparticles prepared by milling are studied together with the 700 nm bulk-like commercial BTO particles and 50 nm nanoparticles as a reference. Raman spectroscopy, XRD, synchrotron XAFS and PDF analysis have been conducted to understand the mechanism behind the large electric polarization in the nanoparticles. The results suggest the alcohol washed BTO sample has a bulk-like structure with Barium oleate component possibly a surface coating. Future experiments need to be conducted to understand the form of the Barium oleate and its role in the large electric polarization in the 10 nm washed BTO nanoparticles.

7.4 Acknowledgement

This work is supported under the U.S. Air Force award FA8650-16-D-54. This research used resources of the National Synchrotron Light Source, a U.S. Department of Energy (DOE) Office of Science User Facility operated for the DOE Office of Science by Brookhaven National Laboratory under Contract No. DE-AC02-98CH10886. This research also used resources of the National Synchrotron Light Source II, a U.S. Department of Energy (DOE) Office of Science User Facility operated for the DOE Office of Science by Brookhaven National Laboratory under Contract No. DE-SC0012704.

CHAPTER 8

CONCLUSION AND FUTURE WORK

8.1 Conclusion

The magnetostructural properties of $RX_3(BO_3)_4$ (R= Ho, Eu, Sm, Nd, Gd; X= Fe, Al) were explored by temperature and magnetic field dependent heat capacity measurements, single crystal x-ray diffraction, pressure and temperature dependent x-ray diffraction measurements, as well as temperature and magnetic field dependent x-ray absorption fine structure measurements. In the system with R=Ho and X=Al, an anomalous change in the structure is found in the region of large magnetoelectric effects, which may be related. The magnetic field dependent structural measurements reveal enhanced correlation between neighboring HoO_6 polyhedra. This observed response is seen to saturate ~ between 2 and 3 T due to the lattice stiffness. These results provide a microscopic level understanding of the mechanism behind the large electric polarization induced by magnetic fields in the general class of $RAl_3(BO_3)_4$ systems (R = rare earth).

In the other systems with R=Fe, the results suggest that the reduced coupling between ferroelectric and magnetic groups caused by the tilting of BO_3 planes and FeO_6 polyhedra is one of the main reasons for the dramatical decrease of the magnetoelectricity in systems with R= Ho, Eu, Gd, and X=Fe. No direct contribution to the magnetoelectric effect was found for the magnetic ordering. The application of pressure along the c axis with $RX_3(BO_3)_4$ can potentially enhance the electric field induced polarization.

In $SrTiO_3$ nanoparticles, we have conducted pressure-dependent structural measurements (up to ~20 GPa) of monodispersed nanoscale samples with average diameters of 10 nm, 20 nm, 40 nm, and 83 nm, respectively. The transition pressure was found to decrease with decreasing particle size, and a robust pressure-independent structure of the 10 nm sample was observed. The results suggest that growth of STO nanoparticles (with near 10 nm diameter) onto substrates which do not match the underlying STO lattice will not alter the polar state of the system for a large range of strain values, thereby enabling more widespread device use.

$BaTiO_3$ nanoparticles prepared by milling are studied together with the 700 nm bulk-like commercial BTO particles as a reference. Raman spectroscopy, XRD, synchrotron XAFS and PDF analysis have been conducted to try to understand the mechanism behind the large electric polarization in the nanoparticles. The results indicate the presence of form of barium oleate in the washed nanoparticles possibly as a coating, The 10 nm washed BTO sample behaves more like bulk than nanoscale BTO. Future experiments need to be conducted to understand the form of the Barium oleate and its role in the large electric polarization in the 10 nm washed BTO nanoparticles.

8.2 Future Work

8.2.1 $RX_3(BO_3)_4$ Systems

In the study with the $RX_3(BO_3)_4$ class of material, the rare earth oxygen polyhedra is found to have enhanced correlations with external magnetic field up to 3 T with the $HoAl_3(BO_3)_4$ system; the structural changes are found to be one of the main reasons causing the dramatic difference in magnetoelectricity for the samples in the $RX_3(BO_3)_4$

class of material. Yet how the structures are coupled with magnetic fields is still to be revealed. More combined magnetic field and temperature structural studies are needed to provide a link between the ground state structure and the magnetoelectric effects. The stable structural phase in magnetic field and the possible long range (and short range) magnetic order must be explored.

Neutron diffraction experiments can also help to address these problems. Neutron diffraction and PDF measurements under magnetic field can be used to study the magnetic ordering of the rare earth and the iron atoms under external magnetic fields. Meanwhile, temperature dependent neutron diffraction with systems that R= Fe can also be used to determine the rare earth site ordering at low temperature without a field.

High-pressure electrical polarization under magnetic field can be measured to try to verify the proposed idea that the application of hydrostatic pressure will most like reduce the magnetoelectric effect in this type of material. This can serve as strong evidence of the conclusion in this work. It is expected that uniaxial pressure will enhance electrical polarization in the Fe based system. Exploring this effect is an extremely important extension of this work.

8.2.2 Nano-SrTiO3 Systems

In this work, a size-dependent structural phase transition under pressure is found for STO nanoparticles of 10 nm, 20 nm, 40 nm, and 83 nm. Yet a few matters are waiting to be concluded in future work.

The most important matter needs to be addressed is the ferroelectricity of the 10nm nanoparticles – direct polarization measurements on STO nanoparticles should be conducted. Piezoresponse Force Microscopy (PFM) is one of the approaches. Due to the

powder form of the sample, methods need to be found to distribute the nanoparticles into a thin layer so that PFM can be used to measure the hysteresis loop (if any) for individual nanoparticles.

The next problem to be answered is the nature of the transition (FE or AFD) for nanoparticles under pressure. High-resolution x-ray diffraction and Raman spectroscopy under high pressure can be utilized to solve the structure of the nanoparticles; theoretical approaches mentioned in Chapter 6 need to be examined and compared with the experimental results in future.

The analysis from Chapter 6 also needs to be conducted with STO nanoparticles of different sizes between 1 nm and 300 nm to study the size-dependence of the nano-STO systems further.

8.2.3 $BaTiO_3$ Nanoparticles by Milling

The existence of Barium oleate is found in the BTO nanoparticles prepared by mechanical milling, but the form and structure are unknown. Transmission Electron Microscopy (TEM) imaging needs to be combined with neutron PDF measurements to obtain the ratio of the BTO and barium oleate phase. With high-Q neutron PDF data detailed two component modeling can be conducted.

APPENDIX

$RX_3(BO_3)_4$ REFINEMENT RESULTS

Table A.1 Structural Parameters from $HoAl_3(BO_3)_4$ at 300K

Atoms	**x**	**y**	**z**	**U_{eq} (Å^2)**	
Ho	0	0	0		
Al	0.8901(8)	2/3	2/3		
O1	0.8146(18)	0.4813(17)	0.83333		
O2	0.0770(22)	0.7436(22)	0.83333		
O3	0.8147(15)	0.7827(14)	0.8122(14)		
B1	2/3	1/3	0.8333		
B2	0.2210(28)	0.8870(28)	0.83333		
U_{ij} (Ho)	0.0074(13)	0.0074(13)	0.0112(15)	0.00372(63)	0.0000	0.0000
U_{ij} (Al)	0.0105(22)	0.0122(26)	0.0131(32)	0.0061(13)	0.0012(9)	0.0023(18)
U_{ij} (O1)	0.0244(57)	0.0244(57)	0.0055(56)	0.0167(70)	0.0040(27)	-0.0040(27)
U_{ij} (O2)	0.0152(70)	0.0152(70)	0.0041(70)	0.0050(68)	0.0015(34)	-0.0015(34)
U_{ij} (O3)	0.0210(58)	0.0204(6)	0.0117(43)	0.0098(51)	-0.0066(41)	-0.0002(43)
U_{ij} (B1)	0.0166(97)	0.0166(97)	0.0140(152)	0.0083(48)	0.0000	0.0000
U_{ij} (B2)	0.0108(77)	0.0108(77)	0.019(11)	-0.0005(104)	-0.0098(67)	0.0098(67)

Space Group: R32
a = 9.2891(16) Å, c = 7.2149(13) Å, Dx = 4.445 g/cm^3
Measurement Temperature: 296 K
Crystal Dimensions: 0.18 × 0.30 × 0.58 mm^3
wavelength: 1.54178 Å,
2θmax: 143.5°
BASF twin parameter: 0.178(56)
Absorption Coefficient : 25.25 mm^{-1}
EXTI extinction parameter:0.01485(33)
Number of Unique Observed Reflections $F_o>4\sigma(F_o)$: 228
Number of fitting parameters: 36
Amplitude of Max Peak in Final Difference map: 1.68 e/ Å^3 (Al)
R_1 = 4.98 %, wR_2 = 12.7 %, Goodness of Fit = 1.23

*Atomic displacement parameters U_{ij}(Å^3) are in the order U_{11}, U_{22}, U_{33}, U_{23}, U_{13}, U_{12}

Table A.2 Structural Parameters from $HoAl_3(BO_3)_4$ at 15K

Atoms	**x**	**y**	**z**	**U_{eq} (Å^2)**	
Ho	0		0	0	
Al	0.88969 (16)		2/3	2/3	
O1	0.81595 (32)		0.48262 (32)	0.83333	
O2	0.07564 (50)		0.74231 (50)	0.83333	
O3	0.81618 (27)		0.78249 (28)	0.81242 (29)	
B1	2/3		1/3	0.8333	
B2	0.22490 (69)		0.89156 (69)	0.83333	
U_{ij} (Ho)	0.0014 (7)	0.0014(7)	0.0015(8)	0.0000	0.0000	0.00070(3)
U_{ij} (Al)	0.0009(3)	0.0008(4)	0.0011(4)	0.00018(44)	0.00009(28)	0.00039(14)
U_{ij} (O1)	0.0018(6)	0.0018(6)	0.0032(8)	0.00064(33)	-0.00064(33)	0.00005(71)
U_{ij} (O2)	0.0033(11)	0.0033(11)	0.0049(11)	0.00041(42)	-0.00041(42)	0.00143(112)
U_{ij} (O3)	0.0026(6)	0.0039(6)	0.0117(43)	-0.0008(5)	-0.00059(50)	0.0023(5)
U_{ij} (B1)	0.0032(10)	0.0032(10)	0.0015(14)	0.0000	0.0000	0.00163(52)
U_{ij} (B2)	0.0067(18)	0.0067(18)	0.0016(11)	-0.0003(54)	-0.0003(54)	0.0063(22)

Space Group: R32
a = 9.2725 (13) Å, c = 7.2168(23) Å, Dx = 4.460 g/cm^3
Measurement Temperature: 15 K
Crystal Diameter: 20 µm
wavelength: 0.41328 Å,
2θ range: 4.2°~40.2°
BASF twin parameter: 0.18(32)
Absorption Coefficient : 2.5 mm^{-1}
EXTI extinction parameter: 0.026 (33)
Number of Unique Observed Reflections $F_o>4\sigma(F_o)$: 1113
Number of fitting parameters: 35
Amplitude of Max Peak in Final Difference map: 1.59 e/ Å^3 (Al)
R_1 = 1.39 %, wR_2 = 5.05 %, Goodness of Fit = 0.853

*Atomic displacement parameters U_{ij}(Å^3) are in the order U_{11}, U_{22}, U_{33}, U_{23}, U_{13}, U_{12}

Table A.3 Structural Parameters from $NdFe_3(BO_3)_4$ at 300K

Atoms	**x**	**y**	**z**	**U_{eq} (Å^2)**
Nd	0.0000	0.0000	0.0000	0.00782(14)
Fe	0.88399(12)	0.6667	0.6667	0.00547(16)
O1	0.8106(6)	0.4773(6)	0.8333	0.0078(7)
O2	0.0769(7)	0.7436(7)	0.8333	0.0113(9)
O3	0.8116(5)	0.7859(6)	0.8146(6)	0.0096(5)
B1	0.6667	0.3333	0.8333	0.0056(12)
B2	0.2210(8)	0.8876(8)	0.8333	0.0066(7)

U_{ij} (Nd)	0.0083(2)	0.0083(2)	0.0069(2)	0.000	0.000	0.00413(9)
U_{ij} (Fe)	0.0053(2)	0.0056(3)	0.0056(4)	-0.00008(18)	-0.00004(9)	0.00280(15)
U_{ij} (O1)	0.0062(10)	0.0062(10)	0.0095(17)	0.0014(6)	-0.0014(6)	0.0021(12)
U_{ij} (O2)	0.0090(14)	0.0090(14)	0.012(2)	0.0027(9)	-0.0027(9)	0.0021(16)
U_{ij} (O3)	0.0075(11)	0.0108(13)	0.0118(13)	-0.0033(10)	-0.0008(10)	0.0056(10)
U_{ij} (B1)	0.0042(18)	0.0042(18)	0.008(3)	0.000	0.000	0.0021(9)
U_{ij} (B2)	0.0078(18)	0.0078(18)	0.0074(17)	0.0005(10)	-0.0005(10)	0.006(3)

Space Group: R32
a = 9.5888(9)Å
c = 7.6108(8)Å
D_x = 4.497 g/cm^3
Measurement Temperature: 300 K
Crystal Diameter: 20 µm
Wavelength: 0.41328 Å,
2θ range: 4.2°~54.7°
Flack parameter: 1.18(12)
Absorption Coefficient: 2.43 mm^{-1}
EXTI extinction parameter: 0.015920
Number of Unique Observed Reflections $F_o>4\sigma(F_o)$: 1380
Number of fitting parameters: 36
Amplitude of Max Peak in Final Difference map: 0.55 e/ Å^3 (Nd)
R_1 = 5.3 %, wR_2 = 13.3 %, Goodness of Fit = 0.83

*Atomic displacement parameters U_{ij}(Å^3) are in the order U_{11}, U_{22}, U_{33}, U_{23}, U_{13}, U_{12}

Table A.4 Structural Parameters from $NdFe_3(BO_3)_4$ at 15K

Atoms	**x**	**y**	**z**	**U_{eq} (Å^2)**
Nd	0.0000	0.0000	1.0000	0.00485(15)
Fe	0.3333	0.21709(12)	0.6667	0.0057(2)
O1	0.2146(5)	0.0265(5)	0.8158(5)	0.0081(5)
O2	0.1446(6)	0.1446(6)	0.5000	0.0068(7)
O3	0.4100(7)	0.4100(7)	0.5000	0.0079(9)
B1	0.5531(7)	0.5531(7)	0.5000	0.0072(8)
B2	0.0000	0.0000	0.5000	0.0076(15)

U_{ij}(Nd)	0.00621(17)	0.0062(2)	0.0021(2)	0.000	0.000	0.00311(8)
U_{ij}(Fe)	0.0061(4)	0.0063(3)	0.0047(5)	0.00004(11)	0.0001(2)	0.00306(18)
U_{ij}(O1)	0.0092(13)	0.0087(13)	0.0071(13)	0.0011(10)	-0.0003(11)	0.0051(11)
U_{ij}(O2)	0.0073(12)	0.0073(12)	0.0057(17)	0.0001(7)	-0.0001(7)	0.0035(14)
U_{ij}(O3)	0.0083(16)	0.0083(16)	0.007(2)	0.0014(8)	-0.0014(8)	0.0041(18)
U_{ij}(B1)	0.0069(19)	0.0069(19)	0.008(2)	-0.0001(12)	0.0001(12)	0.004(3)
U_{ij}(B2)	0.008(2)	0.008(2)	0.007(4)	0.000	0.000	0.0039(11)

a = 9.5925(5)Å
c = 7.6025(4)Å
D_x = 4.498 g/cm^3
Measurement Temperature: 15 K
Crystal Diameter: 20 µm
Wavelength: 0.41328 Å,
2θ range: 4.2°~44.1°
Flack parameter: 1.15(10)
Absorption Coefficient : 2.5 mm^{-1}
EXTI extinction parameter: 0.009743
Number of Unique Observed Reflections $F_o>4\sigma(F_o)$: 812
Number of fitting parameters: 36
Amplitude of Max Peak in Final Difference map: 1.77 e/ Å^3 (Nd)
R_1 = 2.7 %, wR_2 = 7.3 %, Goodness of Fit = 0.59

*Atomic displacement parameters U_{ij}(Å^3) are in the order U_{11}, U_{22}, U_{33}, U_{23}, U_{13}, U_{12}

Table A.5 Structural Parameters from $EuFe_3(BO_3)_4$ at 275K

Atoms	**x**	**y**	**z**	**U_{eq} (Å^2)**	
Eu	0.0000	0.0000	0.5000	0.00727(14)	
Fe	0.44988(8)	0.44988(8)	0.5000	0.00477(14)	
O1	0.2576(5)	0.3333	0.3333	0.0111(7)	
O2	0.5208(3)	0.6411(3)	0.3499(3)	0.0077(4)	
O3	0.5223(4)	0.3333	0.3333	0.0065(5)	
B1	0.6667	0.3333	0.3333	0.0044(9)	
B2	0.1137(5)	0.3333	0.3333	0.0056(6)	
U_{ij}(Eu)	0.0079(2)	0.00791(15)	0.00599(16)	0.000	0.000	0.00396(7)
U_{ij}(Fe)	0.0049(2)	0.0049(2)	0.0045(3)	0.00006(7)	-0.00006(7)	0.00232(16)
U_{ij}(O1)	0.0072(11)	0.0144(14)	0.0142(18)	-0.0092(14)	-0.0046(7)	0.0072(7)
U_{ij}(O2)	0.0073(8)	0.0060(8)	0.0075(9)	0.0018(6)	-0.0005(7)	0.0016(8)
U_{ij}(O3)	0.0055(8)	0.0088(12)	0.0062(12)	-0.0014(9)	-0.0007(4)	0.0044(6)
U_{ij}(B1)	0.0042(14)	0.0042(14)	0.005(2)	0.000	0.000	0.0021(7)
U_{ij}(B2)	0.0049(12)	0.0054(18)	0.0065(14)	-0.0003(13)	-0.0001(7)	0.0027(9)

Space Group: R32
a = 9.5584(3)Å
c = 7.5792(3)Å
D_x = 4.608 g/cm^3
Measurement Temperature: 275K
Crystal Diameter: 20 μm
Wavelength: 0.41328 Å,
2θ range: 4.2°~44.1°
Flack parameter: 0.50(5)
Absorption Coefficient : 2.76 mm^{-1}
EXTI extinction parameter: 0.142753
Number of Unique Observed Reflections $F_o>4\sigma(F_o)$: 763
Number of fitting parameters: 36
Amplitude of Max Peak in Final Difference map: 0.69 e/ Å^3 (Eu)
R_1 = 2.5 %, wR_2 = 4.7 %, Goodness of Fit = 1.17

*Atomic displacement parameters U_{ij}(Å^3) are in the order U_{11}, U_{22}, U_{33}, U_{23}, U_{13}, U_{12}

Table A.6 Structural Parameters from $EuFe_3(BO_3)_4$ at 15K

Atoms	**x**	**y**	**z**	**U_{eq} (Å^2)**
Eu	0.66676(2)	0.66676(2)	1.0000	0.00319(8)
Fe1	1.0000	0.88433(7)	0.6667	0.00359(11)
Fe2	0.33520(4)	0.54970(7)	0.32671(4)	0.00363(10)
O1	0.8118(4)	0.8118(4)	0.5000	0.0064(5)
O2	0.5241(3)	0.6691(2)	0.4944(2)	0.0059(4)
O3	1.0774(3)	1.0774(3)	0.5000	0.0072(5)
O4	0.2688(3)	0.6841(2)	0.4760(3)	0.0075(3)
O5	0.8810(3)	0.6949(3)	0.8191(3)	0.0059(4)
O6	0.2157(3)	0.3616(3)	0.4816(3)	0.0060(4)
O7	0.4599(3)	0.4765(3)	0.1861(3)	0.0059(4)
B1	0.6678(4)	0.6678(4)	0.5000	0.0049(7)
B2	0.4475(4)	0.3284(4)	0.1751(3)	0.0056(5)
B3	1.2215(5)	1.2215(5)	0.5000	0.0057(7)

U_{ij}(Eu)	0.00312(8)	0.00312(8)	0.00334(11)	0.00002(2)	-0.00002(2)	0.00158(6)
U_{ij}(Fe1)	0.0034(2)	0.00352(17)	0.0038(3)	-0.00003(8)	-0.00005(15)	0.00168(11)
U_{ij}(Fe2)	0.0033(2)	0.00349(17)	0.0041(2)	-0.00007(10)	-0.00011(11)	0.00165(12)
U_{ij}(O1)	0.0051(9)	0.0051(9)	0.0080(13)	0.0005(4)	-0.0005(4)	0.0017(10)
U_{ij}(O2)	0.0055(9)	0.0068(10)	0.0059(10)	-0.0010(7)	-0.0008(6)	0.0034(7)
U_{ij}(O3)	0.0062(8)	0.0062(8)	0.0068(12)	0.0009(5)	-0.0009(5)	0.0013(10)
U_{ij}(O4)	0.0074(9)	0.0085(9)	0.0081(7)	-0.0023(7)	-0.0019(6)	0.0052(7)
U_{ij}(O5)	0.0066(8)	0.0054(8)	0.0059(9)	0.0005(6)	0.0003(7)	0.0031(7)
U_{ij}(O6)	0.0073(9)	0.0050(8)	0.0069(8)	0.0006(6)	0.0012(6)	0.0038(7)
U_{ij}(O7)	0.0068(8)	0.0053(9)	0.0063(9)	0.0010(6)	0.0024(6)	0.0035(7)
U_{ij}(B1)	0.0027(11)	0.0027(11)	0.009(2)	0.0000(6)	0.0000(6)	0.0008(12)
U_{ij}(B2)	0.0050(11)	0.0043(13)	0.0061(12)	0.0006(9)	0.0005(8)	0.0014(9)
U_{ij}(B3)	0.0071(13)	0.0071(13)	0.0056(16)	-0.0007(6)	0.0007(6)	0.0055(15)

Space Group: $P3_121$
a = 9.5574(2), c = 7.5757(2)
D_x = 4.611 g/cm^3
Measurement Temperature: 15K
Crystal Diameter: 20 µm
Wavelength: 0.41328 Å,
2θ range: 2.8°~44.1°
Flack parameter: 1.08(4)
Absorption Coefficient : 2.87 mm^{-1}
EXTI extinction parameter: 0.040954
Number of Unique Observed Reflections $F_o>4\sigma(F_o)$: 1851
Number of fitting parameters: 96
Amplitude of Max Peak in Final Difference map: 1.09 e/ Å^3 (Eu)
R_1 = 2.4 %, wR_2 = 4.8 %, Goodness of Fit = 0.67

*Atomic displacement parameters U_{ij}(Å^3) are in the order U_{11}, U_{22}, U_{33}, U_{23}, U_{13}, U_{12}

Table A.7 Structural Parameters from $GdFe_3(BO_3)_4$ at 300K

Atoms	**x**	**y**	**z**	**U_{eq} (Å^2)**
Gd	0.0000	0.0000	0.5000	0.00722(9)
Fe	0.11673(7)	0.3333	0.8333	0.00521
O1	0.1874(3)	0.2129(3)	0.6825(3)	0.0081(3)
O2	0.0000	0.4084(4)	1.0000	0.0124(7)
O3	0.0000	0.1438(3)	1.0000	0.0070(4)
B1	0.0000	0.5530(4)	1.0000	0.0062(5)
B2	0.0000	0.0000	1.0000	0.0057(8)

U_{ij}(Gd)	0.00752(10)	0.00752(10)	0.00662(13)	0.000	0.000	0.00376(5)
U_{ij}(Fe)	0.00497(19)	0.0050(2)	0.0057(3)	-0.0002(1)	-0.00008(6)	0.00252(10)
U_{ij}(O1)	0.0077(7)	0.0102(8)	0.0081(8)	-0.0017(7)	-0.0002(6)	0.0057(6)
U_{ij}(O2)	0.0141(13)	0.0081(10)	0.0170(17)	0.0041(6)	0.0083(13)	0.0070(6)
U_{ij}(O3)	0.0082(11)	0.0052(7)	0.0086(11)	0.0008(4)	0.0017(8)	0.0041(5)
U_{ij}(B1)	0.0070(17)	0.0055(10)	0.0067(12)	0.0005(6)	0.0010(12)	0.0035(8)
U_{ij}(B2)	0.0061(13)	0.0061(13)	0.005(2)	0.000	0.000	0.0030(6)

Space Group: R32
a = 9.5526(4) Å
c = 7.5727(3) Å
D_x = 4.662 g/cm^3
Measurement Temperature: 300 K
Crystal Diameter: 20 µm
Wavelength: 0.41328 Å,
2θ range: 4.2°~40.2°
Flack parameter: 1.04(4)
Absorption Coefficient : 2.9 mm^{-1}
EXTI extinction parameter: 0.01481
Number of Unique Observed Reflections $F_o > 4\sigma(F_o)$: 639
Number of fitting parameters: 36
Amplitude of Max Peak in Final Difference map: 0.56 e/ Å^3 (Gd)
R_1 = 1.3 %, wR_2 = 3.6 %, Goodness of Fit = 0.4

*Atomic displacement parameters U_{ij}(Å^3) are in the order U_{11}, U_{22}, U_{33}, U_{23}, U_{13}, U_{12}

Table A.8 Structural Parameters from $GdFe_3(BO_3)_4$ at 25K

Atoms	**x**	**y**	**z**	**U_{eq} (Å^2)**
Gd	0.33358(2)	0.33358(2)	0.0000	0.00183(9)
Fe1	0.21361(9)	0.54949(9)	0.34234(4)	0.00230(10)
Fe2	-0.11552(9)	0.88448(9)	0.0000	0.00221(10)
O1	0.0000	0.8129(4)	0.1667	0.0037(5)
O2	0.1457(4)	0.66984(11)	0.17422(14)	0.0038(4)
O3	0.1471(3)	0.3629(3)	0.1857(3)	0.0039(3)
O4	0.0000	0.07790(19)	0.1667	0.0050(3)
O5	-0.1196(3)	0.1845(3)	0.5137(3)	0.0041(3)
O6	0.0135(3)	0.4763(3)	0.4803(3)	0.0042(3)
O7	0.31050(16)	0.72745(14)	0.53142(18)	0.00466(19)
B1	-0.1211(5)	0.32646(19)	0.4882(2)	0.0042(5)
B2	0.0000	0.2223(5)	0.1667	0.0039(5)
B3	0.0000	0.66821(19)	0.1667	0.0041(9)

U_{ij}(Gd)	0.00183(10)	0.00183(10)	0.0019(1)	-0.00003(1)	0.00003(1)	0.00095(5)
U_{ij}(Fe1)	0.00205(14)	0.00210(15)	0.0027(1)	0.00002(8)	-0.00012(8)	0.00096(13)
U_{ij}(Fe2)	0.00196(15)	0.00196(15)	0.0025(2)	0.00007(6)	-0.00007(6)	0.00086(15)
U_{ij}(O1)	0.0044(10)	0.0023(7)	0.0052(9)	-0.0005(3)	-0.0011(7)	0.0022(5)
U_{ij}(O2)	0.0025(7)	0.0049(9)	0.0049(8)	0.0012(6)	0.0003(4)	0.0025(5)
U_{ij}(O3)	0.0030(6)	0.0036(6)	0.0039(6)	-0.0013(5)	-0.0005(5)	0.0006(5)
U_{ij}(O4)	0.0063(7)	0.0040(4)	0.0056(6)	-0.0007(2)	-0.0014(5)	0.0031(3)
U_{ij}(O5)	0.0053(6)	0.0035(7)	0.0041(7)	0.0001(5)	-0.0010(5)	0.0027(5)
U_{ij}(O6)	0.0039(6)	0.0032(6)	0.0042(6)	-0.0001(5)	0.0007(5)	0.0008(5)
U_{ij}(O7)	0.0059(4)	0.0033(4)	0.0049(4)	-0.0005(4)	-0.0007(4)	0.0024(4)
U_{ij}(B1)	0.0057(9)	0.0027(9)	0.0041(8)	0.0009(7)	0.0003(6)	0.0020(6)
U_{ij}(B2)	0.0023(11)	0.0041(9)	0.0048(11)	-0.0004(4)	-0.0008(9)	0.0012(5)
U_{ij}(B3)	0.0036(15)	0.0046(14)	0.004(2)	-0.0003(3)	-0.0005(5)	0.0018(7)

Space Group: $P3_121$
a = 9.5477(3), c = 7.5674(2)
D_x = 4.670 g/cm^3
Measurement Temperature: 25K
Crystal Diameter: 20 μm
Wavelength: 0.41328 Å,
2θ range: 2.8°~44.1°
Flack parameter: 1.06(5)
Absorption Coefficient : 3.12 mm^{-1}
EXTI extinction parameter: 0.020427
Number of Unique Observed Reflections $F_o > 4\sigma(F_o)$: 2480
Number of fitting parameters: 96
Amplitude of Max Peak in Final Difference map: 0.78 e/ Å^3 (B3)
R_1 = 1.5 %, wR_2 = 7.2 %, Goodness of Fit = 0.55

*Atomic displacement parameters U_{ij}(Å^3) are in the order U_{11}, U_{22}, U_{33}, U_{23}, U_{13}, U_{12}

Table A.9 Structural Parameters from $SmFe_3(BO_3)_4$ at 300K

Atoms	**x**	**y**	**z**	**U_{eq} (Å^2)**
Sm	0.0000	0.0000	0.0000	0.00764(11)
Fe	0.88379(8)	0.66667	0.66667	0.00491(14)
O1	0.81078(36)	0.47745(36)	0.83333	0.0067(5)
O2	0.07573(44)	0.74240(44)	0.83333	0.0104 (7)
O3	0.81204(35)	0.78617(33)	0.81641(39)	0.0087(4)
B1	0.66667	0.33333	0.83333	0.0051(10)
B2	0.21936(46)	0.88603(46)	0.83333	0.0056(6)

U_{ij}(Sm)	0.00818(12)	0.00818(12)	0.00657(16)	0.00000	0.00000	0.0041(1)
U_{ij}(Fe)	0.00457(20)	0.00470(24)	0.00551(34)	-0.00024(16)	-0.00012(8)	0.0024(1)
U_{ij}(O1)	0.00446(80)	0.00446(80)	0.0082(13)	0.00120(51)	-0.00120(51)	0.0001(9)
U_{ij}(O2)	0.00579(99)	0.00579(99)	0.0145(19)	0.00429(72)	-0.00429(72)	-0.0010(9)
U_{ij}(O3)	0.00830(88)	0.01011(92)	0.0097(10)	-0.00259(83)	-0.00065(79)	0.0060(7)
U_{ij}(B1)	0.0040(14)	0.0040(14)	0.0073(26)	0.00000	0.00000	0.0020(7)
U_{ij}(B2)	0.0041(12)	0.0041(12)	0.0067(14)	-0.00079(86)	0.00079(86)	0.0010(9)

Space Group: R32
a = 9.63880 (3)Å
c = 7.6488(3) Å
D_x = 4.477g/cm^3
Measurement Temperature: 300 K
Crystal Diameter: 20 µm
Wavelength: 0.41328 Å,
2θ range: 4.2°~40.1°
Flack parameter: 0.5(5)
Absorption Coefficient : 6.49mm^{-1}
EXTI extinction parameter: 0.000442
Number of Unique Observed Reflections $F_o>4\sigma(F_o)$: 837
Number of fitting parameters: 36
Amplitude of Max Peak in Final Difference map: 1.45 e/ Å^3 (Fe)
R_1 = 2.2 %, wR_2 = 5.4 %, Goodness of Fit = 0.59

*Atomic displacement parameters U_{ij}(Å^3) are in the order U_{11}, U_{22}, U_{33}, U_{23}, U_{13}, U_{12}

Table A.10 Structural Parameters from $SmFe_3(BO_3)_4$ at 15K

Atoms	**x**	**y**	**z**	**U_{eq} (Å^2)**
Sm	0.0000	0.0000	1.0000	0.00277(9)
Fe	0.3333	0.21681(7)	0.6667	0.00295(12)
O1	0.2137(3)	0.0258(3)	0.8162(3)	0.0051(3)
O2	0.1443(3)	0.1443(3)	0.5000	0.0043(4)
O3	0.4092(4)	0.4092(4)	0.5000	0.0048(5)
B1	0.5524(4)	0.5524(4)	0.5000	0.0045(5)
B2	0.0000	0.0000	0.5000	0.0047(9)

U_{ij}(Sm)	0.0028(1)	0.00283(10)	0.00265(12)	0.000	0.000	0.00142(5)
U_{ij}(Fe)	0.0029(2)	0.00302(18)	0.0029(3)	0.00007(6)	0.0001(1)	0.00146(10)
U_{ij}(O1)	0.0057(7)	0.0039(7)	0.0054(7)	0.0010(6)	0.0009(6)	0.0022(6)
U_{ij}(O2)	0.0032(7)	0.0032(7)	0.0053(10)	0.0004(4)	-0.0004(4)	0.0006(8)
U_{ij}(O3)	0.0037(8)	0.0037(8)	0.0061(11)	0.0010(5)	-0.0010(5)	0.0013(10)
U_{ij}(B1)	0.0027(10)	0.0027(10)	0.0060(12)	0.0000(7)	0.0000(7)	-0.0003(16)
U_{ij}(B2)	0.0040(12)	0.0040(12)	0.006(2)	0.000	0.000	0.0020(6)

Space Group: R32
a = 9.5767(3)Å
c = 7.5925(3) Å
D_x = 4.569 g/cm^3
Measurement Temperature: 15 K
Crystal Diameter: 20 µm
Wavelength: 0.41328 Å,
2θ range: 4.2°~40.1°
Flack parameter: 0.44(5)
Absorption Coefficient : 2.74 mm^{-1}
EXTI extinction parameter: 0.019044
Number of Unique Observed Reflections $F_o>4\sigma(F_o)$: 813
Number of fitting parameters: 36
Amplitude of Max Peak in Final Difference map: 0.98 e/ Å^3 (B1)
R_1 = 1.4 %, wR_2 = 4.4 %, Goodness of Fit = 0.4

*Atomic displacement parameters U_{ij}(Å^3) are in the order U_{11}, U_{22}, U_{33}, U_{23}, U_{13}, U_{12}

Table A.11 Structural Parameters from $HoFe_3(BO_3)_4$ at 275K

Atoms	**x**	**y**	**z**	**U_{eq} (Å^2)**
Ho	0.66502(2)	1.0000	0.3333	0.00415(5)
Fe1	0.88447(6)	0.88447(6)	0.0000	0.00388(9)
Fe2	0.66357(3)	0.45140(6)	0.32155(4)	0.00401(8)
O1	0.8543(3)	0.5248(3)	0.15697(18)	0.0062(4)
O2	0.5334(2)	0.5247(2)	0.1863(2)	0.0067(3)
O3	0.6962(2)	0.8172(2)	0.1557(2)	0.0067(3)
O4	0.72263(18)	0.30366(18)	0.45884(19)	0.0070(3)
O5	0.9221(2)	0.9221(2)	0.5000	0.0088(4)
O6	1.0000	0.8126(3)	0.1667	0.0062(4)
O7	0.7847(2)	0.6371(2)	0.4808(3)	0.0068(3)
B1	0.7780(4)	0.7780(4)	0.5000	0.0060(5)
B2	0.5518(3)	0.6765(3)	0.1822(3)	0.0064(4)
B3	1.0000	0.6684(3)	0.1667	0.0065(7)

U_{ij}(Ho)	0.00360(6)	0.00356(6)	0.00526(7)	0.00020(3)	0.00010(2)	0.00178(3)
U_{ij}(Fe1)	0.00308(14)	0.00308(14)	0.00542(17)	-0.00002(7)	0.00002(7)	0.00149(14)
U_{ij}(Fe2)	0.00324(15)	0.00313(14)	0.00575(14)	-0.00005(9)	0.00016(10)	0.00167(10)
U_{ij}(O1)	0.0050(7)	0.0051(7)	0.0080(8)	-0.0004(5)	0.0006(5)	0.0022(7)
U_{ij}(O2)	0.0084(7)	0.0045(7)	0.0076(7)	-0.0001(5)	-0.0010(6)	0.0035(6)
U_{ij}(O3)	0.0051(7)	0.0053(7)	0.0086(7)	0.0001(6)	0.0006(5)	0.0017(6)
U_{ij}(O4)	0.0062(6)	0.0064(6)	0.0084(6)	0.0003(5)	0.0003(5)	0.0031(5)
U_{ij}(O5)	0.0076(7)	0.0076(7)	0.0097(9)	-0.0015(4)	0.0015(4)	0.0026(8)
U_{ij}(O6)	0.0064(10)	0.0053(7)	0.0074(9)	0.0000(4)	-0.0001(8)	0.0032(5)
U_{ij}(O7)	0.0070(7)	0.0052(7)	0.0088(7)	-0.0004(5)	-0.0007(6)	0.0036(6)
U_{ij}(B1)	0.0074(10)	0.0074(10)	0.0063(12)	-0.0005(5)	0.0005(5)	0.0060(12)
U_{ij}(B2)	0.0065(9)	0.0041(10)	0.0076(8)	0.0006(7)	-0.0004(7)	0.0019(7)
U_{ij}(B3)	0.0071(14)	0.0059(11)	0.0068(15)	0.0006(5)	0.0011(9)	0.0036(7)

Space Group: $P3_121$
a = 9.5707(14), 7.5855(15)
D_x = 4.700 g/cm^3
Measurement Temperature: 275K
Crystal Diameter: 20 μm
Wavelength: 0.41328 Å,
2θ range: 2.8°~40.2°
Flack parameter: 0.49(2)
Absorption Coefficient : 8.06 mm^{-1}
EXTI extinction parameter: 0.002330
Number of Unique Observed Reflections $F_o>4\sigma(F_o)$: 1944
Number of fitting parameters: 96
Amplitude of Max Peak in Final Difference map: 1.18 e/ Å^3 (Fe2)
R_1 = 1.4 %, wR_2 = 3.8 %, Goodness of Fit = 1.0

*Atomic displacement parameters U_{ij}(Å^3) are in the order U_{11}, U_{22}, U_{33}, U_{23}, U_{13}, U_{12}

Table A.12 Structural Parameters from $HoFe_3(BO_3)_4$ at 10K

Atoms	**x**	**y**	**z**	**U_{eq} (Å^2)**
Ho	0.66486(2)	1.0000	0.3333	0.00355(6)
Fe1	0.88413(6)	0.88413(6)	0.0000	0.00351(10)
Fe2	0.66351(3)	0.45169(6)	0.32133(4)	0.00367(9)
O1	0.8543(3)	0.5250(3)	0.1565(2)	0.0062(4)
O2	0.5327(2)	0.5248(3)	0.1864(3)	0.0066(3)
O3	0.6959(2)	0.8174(3)	0.1557(3)	0.0067(3)
O4	0.72209(19)	0.3030(2)	0.4578(2)	0.0068(3)
O5	0.9222(2)	0.9222(2)	0.5000	0.0079(4)
O6	1.0000	0.8128(3)	0.1667	0.0068(5)
O7	0.7848(3)	0.6371(2)	0.4808(3)	0.0067(3)
B1	0.7784(4)	0.7784(4)	0.5000	0.0062(6)
B2	0.5515(4)	0.6767(3)	0.1826(3)	0.0056(4)
B3	1.0000	0.6680(3)	0.1667	0.0061(7)

U_{ij}(Ho) 0.0030(1)	0.00299(7)	0.00464(8)	0.00012(4)	0.00006(2)	0.00149(3)
U_{ij}(Fe1)0.0028 (2)	0.00283(15)	0.00491(17)	0.00000(7)	0.00000(7)	0.00146(15)
U_{ij}(Fe2)0.0029(2)	0.00289(15)	0.00536(14)	-0.00010(9)	0.00006(11)	0.00152(11)
U_{ij}(O1) 0.0048(7)	0.0051(7)	0.0084(8)	-0.0002(5)	0.0007(5)	0.0021(7)
U_{ij}(O2) 0.0070(7)	0.0045(7)	0.0085(7)	0.0004(6)	-0.0004(6)	0.0030(6)
U_{ij}(O3) 0.0056(7)	0.0052(7)	0.0083(7)	-0.0001(6)	0.0006(6)	0.0021(6)
U_{ij}(O4) 0.0061(6)	0.0064(6)	0.0084(6)	0.0000(6)	0.0005(5)	0.0037(5)
U_{ij}(O5) 0.0067(7)	0.0067(7)	0.0097(9)	-0.0009(4)	0.0009(4)	0.0029(8)
U_{ij}(O6) 0.0072(11)	0.0054(7)	0.0085(10)	0.0000(4)	0.0000(9)	0.0036(5)
U_{ij}(O7) 0.0066(7)	0.0052(7)	0.0088(7)	-0.0004(6)	-0.0001(6)	0.0033(6)
U_{ij}(B1) 0.006(1)	0.0061(10)	0.0081(13)	0.0002(6)	-0.0002(6)	0.0044(12)
U_{ij}(B2) 0.0053(9)	0.0035(10)	0.0068(9)	0.0011(8)	-0.0002(7)	0.0013(8)
U_{ij}(B3) 0.0067(1)	0.0047(11)	0.0077(15)	0.0002(5)	0.0003(10)	0.0033(7)

Space Group: $P3_121$
a = 9.5707(14)), 7.5855(15)
D_x = 4.700 g/cm^3
Measurement Temperature: 10K
Crystal Diameter: 20 µm
Wavelength: 0.41328 Å,
2θ range: 2.8°~40.2°
Flack parameter: 0.49(3)
Absorption Coefficient : 3.49 mm^{-1}
EXTI extinction parameter: 0.000000
Number of Unique Observed Reflections $F_o>4\sigma(F_o)$: 1800
Number of fitting parameters: 96
Amplitude of Max Peak in Final Difference map: 1.06 e/ Å^3 (Fe1)
R_1 = 1.4 %, wR_2 = 4.0 %, Goodness of Fit = 1.05

*Atomic displacement parameters U_{ij}(Å^3) are in the order U_{11}, U_{22}, U_{33}, U_{23}, U_{13}, U_{12}

REFERENCES

[1] (a) H. Wu, L. Li, L.-Z. Liang, S. Liang, Y.-Y. Zhu and X.-H. Zhu, Journal of the European Ceramic Society **35,** 411 (2015).
(b) R. D. Johnson and P. G. Radaelli, Annual Review of Materials Research **44**, 269 (2014).
(c) N. A. Spaldin, S. W. Cheong and R. Ramesh, Physics Today **63**, 38 (2010).
(d) K. F. Wang, J. M. Liu and Z. F. Ren, Advances in Physics **58**, 321 (2009).
(e) R. Ramesh and N. A. Spaldin, Nature materials **6**, 21 (2007).
(f) S.-W. Cheong and M. Mostovoy, Nature materials **6**, 13 (2007).

[2] J. Valasek, Physical Reviews **15**, 537 (1920).

[3] M. J. Polking, M. G. Han, A. Yourdkhani, V. Petkov, C. F. Kisielowski, V. V. Volkov, ... and R. Ramesh, Nature Materials **11**, 700(2012).

[4] J. F. Scott, Nature materials **6**, 256 (2007).

[5] W. Rontgen, Annals of Physics **35**, 264 (1888).

[6] P. Curie, Journal de Physique **3**, 393 (1894).

[7] P. Debye, Zeitschrift für Physik **36**, 300 (1926),

[8] (a) M. Fiebig, Journal of Physics D: Applied Physics **38**, 8 (2005).
(b) M.I. Bichurin, V.M. Petrov, R.V. Petrov, Journal of Magnetism and Magnetic Materials **324**, 3548 (2012).
(c) T. Birol, N. Benedek, H. Das, A. Wysocki, A. Mulder, B. Abbett, E. Smith, S. Ghosh, C. Fennie, Current Opinion in Solid State and Materials Science **16**, 227 (2012).
(d) M. Fiebig, T. Lottermoser, D. Meier and M. Trassin, Nature Reviews Materials **1**, 16046 (2016).
(e) W. Eerenstein, N. D. Mathur and J. F. Scott, Nature **442**, 759 (2006).
(f) N. Spaldin, Nature Review Materials **2**,17017 (2017)

[9] H. Schmid, Ferroelectrics **162**, 665 (1994).

[10] N. Spaldin and M. Fiebig, Science **309**, 391 (2005).

[11] J. Van Den Brink and D. I. Khomskii, Journal of Physics: Condensed Matter **20**, 434217 (2008).

[12] B. D. Stojanovic, C. Jovalekic, V. Vukotic, A. Z. Simoes and J. A. Varela, Ferroelectrics **319**, 65 (2005).

[13] G. Lawes, A. Harris, T. Kimura, N. Rogado, R. Cava, A. Aharony, O. Entin-Wohlman, T. Yildirim, M. Kenzelmann, C. Broholm and A. Ramirez, Physical Review Letters **95**, 087205 (2005).

[14] A. Arkenbout, T. Palstra, T. Siegrist and T. Kimura, Physical Review B **74**, 184431 (2006).

[15] S. Park, Y. Choi, C. Zhang and S. W. Cheong, Physical Review Letters **98**, 057601 (2007).

[16] T. Kimura, J. C. Lashley and A. P. Ramirez, Physical Review B **73**, 220401(R) (2006).

[17] Y. Yamasaki, S. Miyasaka, Y. Kaneko, J. P. He, T. Arima and Y. Tokura, Physical Review Letters **96**, 207204 (2006).

[18] X. K. Wei, T. Zou, F. Wang, Q. H. Zhang, Y. Sun, L. Gu, A. Hirata, M. W. Chen, Y. Yao, C. Q. Jin and R. C. Yu, Journal of Applied Physics **111**, 073904 (2012).

[19] J. Hwang, E. S. Choi, H. D. Zhou, J. Lu and P. Schlottmann, Physical Review B **85**, 024415 (2012).

[20] (a) M. Shang, C. Zhang, T. Zhang, L. Yuan, L. Ge, H. Yuan and S. Feng, Applied Physics Letters **102**, 062903 (2013).
(b) X. Xu and W. Wang, Modern Physics Letters B **28**, 1430008 (2014).

[21] (a) F. Hong, Z. Cheng and X. Wang, Journal of Applied Physics **112**, 013920 (2012).
(b) J. Magesh, P. Murugavel, R. V. K. Mangalam, K. Singh, C. Simon and W. Prellier, Journal of Applied Physics **112**, 104116 (2012).
(c) B. Lorenz, ISRN Condensed Matter Physics **2013**, 1 (2013).
(d) T. Kimura, T. Goto, H. Shintani, K. Ishizaka, T. Arima and Y. Tokura, Nature **426**, 55 (2003).
(e) N. Hur, S. Park, P. A. Sharma, S. Guha and S. W. Cheong, Physical Review Letters **93**, 107207 (2004).

[22] (a) O. Zaharko and H. Berger, Journal of Physics: Condensed Matter **22**, 056002 (2010).
(b) F. Wu, E. Kan, C. Tian and M. H. Whangbo, Inorganic Chemistry **49**, 7545 (2010).
(c) Y. S. Oh, S. Artyukhin, J. J. Yang, V. Zapf, J. W. Kim, D. Vanderbilt and S. W. Cheong, Nature communications **5**, 3201 (2014).

[23] (a) N. Ikeda, H. Ohsumi, K. Ohwada, K. Ishii, T. Inami, K. Kakurai, ... and H. Kitô, Nature **436**, 1136 (2005).
(b) M. A. Subramanian, T. He, J. Chen, N. S. Rogado, T. G. Calvarese and A. W. Sleight, Advanced Materials **18**, 1737 (2006).

[24] K. C. Liang, W. Zhang, B. Lorenz, Y. Y. Sun, P. S. Halasyamani and C. W. Chu, Physical Review B **86**, 094414 (2012).

[25] M. Vopsaroiu, M. G. Cain, G. Sreenivasulu, G. Srinivasan and A. M. Balbashov, Material Letters **66**, 282 (2012).

[26] (a) A. Roy, R. Gupta and A. Garg, Advances in Condensed Matter Physics, **1** (2012).
(b) M. M. Vopson, E. Zemaityte, M. Spreitzer and E. Namvar, Journal of Applied Physics **116**, 113910 (2014).
(c) M. Gajek, M. Bibes, S. Fusil, K. Bouzehouane, J. Fontcuberta, A. Barthélémy and A. Fert, Nature materials **6**, 296 (2007).

[27] F. Yang, Y. C. Zhou, M. H. Tang et al., Journal of Physics D **42**, 072004 (2009).

[28] Y. Wang, J. Hu, Y Lin and C. Nan, NPG Asia Materials **2**, 61 (2010)

[29] Y. Chye, T. Liu, D. Li, K. Lee, D. Lederman and T. H. Myers, Applied Physics Letters **88**, 132903 (2006).

[30] L. Kozielski and F. Clemens, Processing and Application of Ceramics **6**, 15 (2012).

[31] (a) J.F. Scott, Nature Materials **6**, 256 (2007).
(b) M. Gajek, M. Bibes, S. Fusil, K. Bouzehouane, J. Fontcuberta, A. Barthelemy and A. Fert, Nature Materials **6**, 296 (2007).

[32] (a) A. K. Zvezdin, S. S. Krotov, A. M. Kadomtseva, G. P. Vorob'ev, Y. F. Popov, A. P. Pyatakov, L. N. Bezmaternykh and E. A. Popova, Journal of Experimental and Theoretical Physics Letters **81**, 272 (2005).
(b) F. Yen, B. Lorenz, Y. Sun, C. Chu, L. Bezmaternykh and A. Vasiliev, Physical Review B **73**, 054435 (2006).
(c) S. S. Krotov, A. M. Kadomtseva, Y. F. Popov, G. P. Vorob'ev, A. V. Kuvardin, K. I. Kamilov, L. N. Bezmaternykh and E. A. Popova, Journal of Magnetism and Magnetic Materials **300**, e426 (2006).
(d) Ph. Goldner, O. Guillot-Noël, J. Petit, M. Popova and L. Bezmaternykh, Physical Review B **76**, 165102 (2007).
(e) T. Kurumaji, K. Ohgushi and Y. Tokura, Physical Review B **89**, 195126 (2014).

[33] T. N. Stanislavchuk, E. P. Chukalina, M. N. Popova, L. N. Bezmaternykh and I. A. Gudim, Physics Letters A **368**, 408 (2007).

[34] (a) R. Chaudhury, F. Yen, B. Lorenz, Y. Sun, L. Bezmaternykh, V. Temerov and C. Chu, Physical Review B **80**, 104424 (2009).
(b) C. Ritter, A. Vorotynov, A. Pankrats, G. Petrakovskii, V. Temerov, I. Gudim and R. Szymczak, Journal of Physics: Condensed Matter **20**, 365209 (2008).
(c) A. Pankrats, G. Petrakovskii, A. Kartashev, E. Eremin and V. Temerov, Journal of Physics: Condensed Matter **21**, 436001 (2009).
(d) A. A. Demidov and D. V. Volkov, Physics of the Solid State **53**, 985 (2011).
(e) V. I. Zinenko, M. S. Pavlovskii, A. S. Krylov, I. A. Gudim and E. V. Eremin, Journal of Experimental and Theoretical Physics **117**, 1032 (2014).
(f) D. K. Shukla, S. Francoual, A. Skaugen, M. V. Zimmermann, H. C. Walker, L. N. Bezmaternykh, ... and J. Strempfer, Physical Review B **86**, 224421 (2012).

[35] J. E. Hamann-Borrero, S. Partzsch, S. Valencia, C. Mazzoli, J. Herrero-Martin, R. Feyerherm, E. Dudzik, C. Hess, A. Vasiliev, L. Bezmaternykh, B. Büchner and J. Geck, Physical Review Letters **109**, 267202 (2012).

[36] K. N. Boldyrev, T. N. Stanislavchuk, A. A. Sirenko, L. N. Bezmaternykh and M. N. Popova, Physical Review B **90**, 121101 (2014).

[37] K. N. Boldyrev, T. N. Stanislavchuk, S. A. Klimin, M. N. Popova and L. N. Bezmaternykh, Physics Letters A, **376**, 2562 (2012).

[38] K. N. Boldyrev and D. A. Erofeev, Optics and Spectroscopy, **116** 872 (2014).

[39] E. A. Popova, A. N. Vasiliev, V. L. Temerov, L. N. Bezmaternykh, N. Tristan, R. Klingeler and B. Büchner, Journal of Physics: Condensed Matter **22**, 116006 (2010).

[40] E. A. Popova, D. V. Volkov, A. N. Vasiliev, A. A. Demidov, N. P. Kolmakova, I. A. Gudim, ... and R. Klingeler, Physical Review B **75**, 224413 (2007).

[41] R. P. Chaudhury, B. Lorenz, Y. Y. Sun, L. N. Bezmaternykh, V. L. Temerov and C. W. Chu, Physical Review B **81**, 220402(R) (2010).

[42] Y. Saeed, N. Singh and U. Schwingenschlögl, Journal of Applied Physics **110**, 103512 (2011).

[43] K. C. Liang, R. P. Chaudhury, B. Lorenz, Y. Y. Sun, L. N. Bezmaternykh, V. L. Temerov and C. W. Chu, Physical Review B **83**, 180417(R) (2011).

[44] A. L. Freydman, A. D. Balaev, A. A. Dubrovskiy, E. V. Eremin, V. L. Temerov and I. A. Gudim, Journal of Applied Physics **115**, 174103. (2014).

[45] (a) C. Q. Sun, Prog. Solid State Chemistry **35**, 1 (2007).
(b) W. H. Qi, Journal of Material Science **41**, 5679. (2006)

[46] C. Q. Sun, W. H. Zhong, S. Li, B. K. Tay, H. L. Bai, E.Y. Jiang, Journal of Physical Chemistry B **108**, 1080 (2004).

[47] P. Chen, X. Xu, C. Koenigsmann, A. C. Santulli, S. S. Wong, and J. L. Musfeldt, Nano letters **10**, 4526 (2010).

[48] W. Han, J. Zhu, S. Zhang, H. Zhang, X. Wang, Q. Wang, C. Gao, and C. Jin, Journal of Applied Physics **113**, 193513 (2013).

[49] Y. Li, W. Qi, Y. Li, E. Janssens, and B. Huang, Journal of Physical Chemistry C **116**, 9800 (2012).

[50] S. M. Clark, S. G. Prilliman, C. K. Erdonmez and A. P. Alivisatos, Nanotechnology **16,** 2813, (2005).

[51] S. B. Qadri, J. Yang, B. R. Ratna, E. F. Skelton, and J. Z. Hu, Applied Physics Letters **69**, 2205 (1996).

[52] V. Swamy, A. Kuznetsov, L. S. Dubrovinsky, P.F. McMillan, V.B. Prakapenka, G. Shen, and B. C. Muddle, Physical Review Letters **96,** 135702 (2006).

[53] M. X. Gu, C. Q. Sun, Z. Chen, T. C. Au Yeung, S. Li, C. M. Tan, V. Nosik, Physical Review B **75**, 125403 (2007).

[54] D. Lee, H. Lu, Y. Gu, S-Y. Choi, S-D. Li, S. Ryu, T. R. Paudel et al., Science **349**, 1314(2015).

[55] M. Itoh, R. Wang, Y. Inaguma, T. Yamaguchi, Y. J. Shan and T. Nakamura, Physical Review Letters **82**, 3540(1999).

[56] T. Mitsui and W. B. Westphal, Physical Review **124**, 1354 (1961).

[57] P. A. Fleury and J. M. Worlock, Physical Review **174**, 613 (1968).

[58] A. F. Devonshire, Advances in Physics **3**, 85 (1954).

[59] J. H. Haeni, P. Irvin, W. Chang, R. Uecker, P. Reiche, Y. L. Li, ... and D. G. Schlom, Nature **430**, 758 (2004).

[60] M. D. Biegalski, E. Vlahos, G. Sheng, Y. L. Li, M. Bernhagen, P. Reiche, R. Uecker, S. K. Streiffer, L. Q. Chen, V. Gopalan, D. G. Schlom, and S. Trolier-McKinstry, Physical Review B **79**, 224117 (2009).

[61] H. W. Jang, A. Kumar, S. Denev, M. D. Biegalski, P. Maksymovych, C. W. Bark, ... and C. B. Eom, Physical Review Letters **104**, 197601 (2010).

[62]Y. P. Cai, D. Z. Han, and R. Y. Ning, The Journal of Chemical Physics **23**, 237 (2010).

[63] (a) R. A. Cowley, Physical Review Letters **9**, 159 (1962).
(b) W. Taylor and A. F. Murray, Solid State Communications **31**, 937 (1979).
(c) D. A. Bruce and W. G. Stirling, Journal of Physics C **16**, 841 (1983).

[64]A. G. Beattie and G. A. Samara, Journal of Applied Physics **42**, 2376 (1971).

[65] Bin Okai and Jiichiro Yoshimoto, Journal of the Physics Society of Japan **39**, 162 (1975).

[66] (a) T. Ishidate, S. Sasaki and K. Inoue, High Pressure Research **1**, 53 (1988).
(b) B. Bonello and M. Fischer, The Journal of Acoustical Society of America **86, 2**257 (1989).
(c) M. Fisher, D. Bonello, A. Polian and J.-M. Leger, Geophysical Monograph Series; Perovskite: A Structure of Great Interest to Geophysics and Materials Science **45**, 125 (1989).

[67] (a) T. Ishidate and T. Isonuma, Ferroelectrics **137**, 45 (1992).
(b) A. Grzechnik, G. H. Wolf and P. F. McMillan, Journal of Raman Spectroscopy **28**, 885 (1997).

[68] (a) M. Fischer, B. Bonello, J. Itié, A. Polian, E. Dartyge, A. Fontaine and H. Tolentino, Physical Review B **42**, 8494 (1990).
(b) D. Cabaret, B. Couzinet, A. M. Flank, J. P. Itie, P. Lagrade and A. Polian, X-Ray Absorption Fine Structure--XAFS **13**, 120 (2007).
(c) J. P. itie, B. Couzinet, A. M. Flank, P. Lagrade and A. Polian, X-Ray Absorption Fine Structure--XAFS **13**, 241 (2007).
(d) J. P. Itie, A. M. Flank, P. Lagarde, S. Ravy and A. Polian, NatoSci Peace Sec B, 51 (2010).

[69] A. Hachemi, H. Hachemi, A. Ferhat-Hamida and L. Louail, Physica Scripta **82**, 025602 (2010).

[70] M. Guennou, P. Bouvier, J. Kreisel and D. Machon, Physical Review B **81**, 054115 (2010).

[71] (a) D. Lheureux, A. Polian, M. Fischer, M. Gauthier and J. P. Itie, 2000 Institute of Electrical and Electronics Engineers Ultrasonic Symposium 557 (2000).
(b) Q. Wang, J. Yang, B. Liu, C. Liu, T. Hu, Y. Li, N. Su, D. Sang, Y. Han and C. Gao, physica status solidi (b) **248**, 1111 (2011).
(c) S.-C. Weng, R. Xu, A. H. Said, B. M. Leu, Y. Ding, H. Hong, X. Fang, M. Y. Chou, A. Bosak, P. Abbamonte, S. L. Cooper, E. Fradkin, S. L. Chang and T. C. Chiang, Europhysics Letters **107** (3), 36006 (2014).

[72] X.Wu, D. Wu and X. Liu, Solid State Communications **145** 255 (2008).

[73] Sook-IlKwunand Tae Kwon Song, Ferroelectrics **197**, 125 (1997).

[74] S. Tsunekawa, K. Ishikawa, Z. Li, Y. Kawazoe and A. Kasuya, Physical Review Letters **85**, 3440 (2000)

[75] Takuya Hoshina, Hirofumi Kakemoto, Takaaki Tsurumi, and Satoshi Wada, Journal of Applied. Phys. **99**, 054311 (2006).

[76] (a) S. Basun, G. Cook, V. Reshetnyak, A. Glushchenko and D. Evans, Physical Review B **84**, 024105, (2011).
(b) D. Evans, S. Basun, G. cook, I. Pinkevych and V. Reshetnyak, Physical Review B **84**, 174111, (2011).

[77] T. A. Tyson, T. Yu, M. Croft, M. E. Scofield, D. Bobb-Semple, J. Tao, C. Jaye, D. Fischer and S. S. Wong, Applied Physics Letters **105**, 091901 (2014).

[78] W. Röntgen, Science **3**, 227 (1896).

[79] A. Sokolov and I. Ternov, Akademia Nauk SSSR, Moskovskoie Obshchestvo Ispytatelei prirody. Sektsia Fiziki. Sinkhrotron Radiation, Nauka Eds., Moscow, 1966.

[80] B. Warren, *X-ray Diffradction*, New York, NY: Dover Publications, 1990.

[81] I. Elishakoff, *Probabilistic Methods in the Theory of Structures: Strength of Materials, Random Vibrations, and Random Buckling*. Hackensack, NJ: World Scientific, 1983.

[82] B. Toby, Powder diffraction **21**, 67 (2006).

[83] A. Lawson and T. Tang, Review of Scientific Instruments **21**, 815 (1950).

[84] A. Jayaraman, Reviews of Modern Physics **55**, 65 (1983).

[85] D. Dunstan, Review of Scientific Instruments **60**, 3789 (1989).

[86] S. Klotz, J. Chervin, P. Munsch and G. Marchand, Journal of Physics D: Applied Physics **42**, 075413 (2009).

[87] H. Mao, J. Xu, and P. Bell, Journal of Geophysical Research: Solid Earth **91**, 4676 (1986).

[88] (a) R. B. Neder and T. Proffen, *Diffuse Scattering and Defect Structure Simulations*, Oxford, UK: Oxford University Press, 2008.
(b) T. Egami and S. L. J. Billinge, *Underneath the Bragg Peaks: Structural Analysis of Complex Materials*, Pergamon, Amsterdam: Elsevier, 2003.
(c) T. Proffen, S. J. L. Billinge, T. Egami, and D. Louca, Zeitschrift für Kristallographie **218**, 132 (2003).
(d) V. Petkov, *Characterization of Materials*, Hoboken, NJ: Wiley, 2012.
(f) R. Dinnerbier and S. Billinge, *Powder Diffraction: Theory and Practice*, Cambridge, UK: The Royal Society of Chemistry, 2008.

[89] C. Farrow, P. Juhas, J. Liu, D. Bryndin, E. Božin, J. Bloch, Th Proffen, and S. Billinge, Journal of Physics: Condensed Matter **19**, 335219 (2007).

[90] G. Bunker, *Introduction to XAFS*, Cambridge, UK: Cambridge University Press, 2010.

[91] J. S. Hwang, K. J. Lin and C. Tien, Review of Scientific Instruments **68**, 94 (1997).

[92] (a)W. Yang and P. Ayers, Computational Medicinal Chemistry for Drug Discovery, CRC Press, 103 (2003).
(b) R. M. Martin, *Electronic Structure: Basic Theory and Practical Methods*, Cambridge, UK: Cambridge Press, 2004.

[93] P. Blaha, K. Schwarz, G. Madsen, D. Kvasnicka and J. Luitz, An augmented plane wave+ local orbitals program for calculating crystal properties (Vienna University of Technology ,2001).

[94] H. Chen, T. Yu, P. Gao, J. Bai, J. Tao, T. A. Tyson, L. Wang, and R. Lalancette, Inorganic Chemistry **52**, 9692 (2013).

[95] (a) J. Hafner, Journal of Computational Chemistry **29**, 2044 (2008).
(b) G. Kresse and J. Furthmüller, Computational Materials Science **6**, 15 (1996).
(c) G. Kresse and J. Furthmüller, Physical Review B **54**,11169 (1996).

[96] A. Hammersley, European Synchrotron Radiation Facility Internal Report ESRF97HA02T (1997).

[97] V. Petricek, M. Dusek and L. Palatinus, Zeitschrift für Kristallographie **229**, 345 (2014).

[98] P. Juhas, T. Davis, C. L. Farrow and S. J. Billinge, Journal of Applied Crystallography **46**, 560 (2013).

[99] J. Lu, C. Fu and J. Chen, Applied Optics **50**, 116 (2011).

[100] A. I. Begunov, A. A. Demidov, I. A. Gudim and E. V. Eremin, Journal of Experimental and Theoretical Physics Letters **97**, 528 (2013).

[101] (a) M. Janoschek, P. Fischer, J. Schefer, B. Roessli, V. Pomjakushin, M. Meven, ... and L. Bezmaternikh, Physical Review B **81**, 094429 (2010).
(b) P. Fischer, V. Pomjakushin, D. Sheptyakov, L. Keller, M. Janoschek, B. Roessli, ... and D. Velikanov, Journal of Physics: Condensed Matter **18**, 7975. (2006).

[102] C. Ritter, A. Pankrats, I. Gudim and A. Vorotynov, , Journal of Physics: Condensed Matter **24**, 386002 (2012).

[103] (a) C. Ritter, A. Vorotynov, A. Pankrats, G. Petrakovskii, V. Temerov, I. Gudim and R. Szymczak, Journal of Physics: Condensed Matter **22**, 206002 (2010).
(b) C. Ritter, A. Vorotynov, A. Pankrats, G. Petrakovskii, V. Temerov, I. Gudim and R. Szymczak, Journal of Physics: Condensed Matter **20**, 365209 (2008).
(c) C. Ritter, A. Balaev, A. Vorotynov, G. Petrakovskii, D. Velikanov, V. Temerov and I. Gudim, Journal of Physics: Condensed Matter **19**, 196227 (2007).

[104] (a) T. Heitmann, Q. Zhang, K. C. Liang, L. M. Bezmaternykh, V. L. Temerov, B. Lorenz and D. Vaknin, Annual Fall Meeting of the APS Prairie Section, PSF13 Meeting of the American Physical Society. (2013).
(b) T. Heitmann, private communications.

[105] V. G. Tyuterev and N. Vast, Computational Materials Science **38**, 350 (2006).

[106] K. Strössner, M. Cardona, W. J. Choyke, Solid State Communications **63**, 113 (1987).

[107] M. L. Cohen, Physical Review B **32**, 7988 (1985).

[108] I. Loa, P. Adler, A. Grzechnik, K. Syassen, U. Schwarz, M. Hanfland, ... and M. P. Pasternak, Physical Review Letters **87**, 125501 (2001).

[109] (a) M. B. Smith, K. Page, T. Siegrist, P. L. Redmond, E. C. Walter, R. Seshadri, ... and M. L. Steigerwald, Journal of American Chemistry Society **130**, 6955 (2008).
(b) V. Petkov, M. Gateshki, M. Niederberger and Y. Ren, Chemistry of Materials **18**, 814 (2006).

[110] P. Debye, Annals of Physics **344**, 789 (1912).

[111] (a) D. R. Chipman, Journal of Applied Physics **31**, 2012 (1960).
(b) M. Rosen, Physical Review Letters **19**, 695 (1967).
(c) R. N. Clayton and S. W. Kieffer, Stable isotope geochemistry: A tribute to Samuel Epstein, Geochemical Society **3**, 3 (1991).
(d) R. Gumeniuk, W. Schnelle, H. Rosner, M. Nicklas, A. Leithe-Jasper and Y. Grin, Physical Review Letters **100**, 017002 (2008).

[112] K. R. Knox, E. S. Bozin, C. D. Malliakas, M. G. Kanatzidis and S. J. L. Billinge, Physical Review B **89**, 014102 (2014).

[113] K. R. Knox, A. M. M. Abeykoon, H. Zheng, W. G. Yin, A. M. Tsvelik, J. F. Mitchell, ... and E. S. Bozin, Physical Review B **88**, 174114 (2013).

[114] C. Lee, J. Kang, K. H. Lee and M. H. Whangbo, Chemistry of Materials **21**, 2534 (2009).

[115] (a) M. Gamża, A. Ślebarski and H. Rosner, European Physical Journal B **67**, 483 (2009).
(b) S. Goumri-Said and M. B. Kanoun, Journal of Physics D: Applied Physics **41**, 035004 (2008).

[116] Y. Hinatsu, Y. Doi, K. Ito, M. Wakeshima and A. Alemi, Journal of Solid State Chemistry **172**, 438 (2003).

[117] L. Bezmaternykh, V. Temerov, I. Gudim, Crystallography Reports **50**, 97 (2005).

[118] Bruker, A. P. E. X, *Saint and SADABS*, Madison, WI: Bruker AXS Inc., 2009.

[119] G. Sheldrick, XPREP, Madison, WI: Bruker AXS Inc., 2003.

[120] G. Sheldrick, Acta Crystallographica Section A: Foundations and Advances **71**, 3 (2015).

[121] A. Spek, Journal of Applied Crystallography **36**, 7 (2003).

[122] A. Gavriliuk, S. A. Kharlamova, I. Lyubutin, I. A. Troyan, S. Ovchinnikov, A. Potseluiko, M. Eremets, and R. Boehler, Journal of Experimental and Theoretical Physics Letters **80**, 426 (2004).

[123] K. Fujinami, K. Katagiri, J. Kamiya, T. Hamanaka and K. Koumoto, Nanoscale **2**, 2080 (2010).

[124] C. Chai, X. Shi, Z.Yang, K. Li and P. Peng, International Journal of Engineering Science technology and Research **3**, 101 (2014).

[125] C. Chen, Q. Dai, C. Miao and L. Xu, Hongwei Song, Royal Society of Chemistry Advances **5**, 4844 (2015).

[126] Y. Mao, S. Banerjee and S. S. Wong, Journal of American Chemistry Society **125**, 15718 (2003).

[127] Ross J. Angel, Maciej Bujak, Jing Zhao, G. Diego Gatta and Steven D. Jacobsen, Journal of Applied Crystallography **40**, 26 (2007).

[128] V. K. Pecharsky and P. Y. Zavalij, *Fundamentals of Powder Diffraction and Structural Characterization of Materials*, Berlin, Germany: Springer, 2009.

[129] Y. Sharma, S. Sahoo, A. K. Mishra, P. Misra, S. P. Pavunny, A. Dwivedi, S. M. Sharma, and R. S. Katiyar. Journal of Applied Physics **117,** 094101(2015).

[130] A. Sani, M. Hanflan and D. Levy, Journal of Physics: Condensed Matter **14**, 10601 (2002).

[131] A. Sani, M. Hanfland, and D. Levy, Journal of Solid State Chemistry **167**, 446 (2002).

[132] J. Zhu, H. Xu, J. Zhang, C. Jin, L. Wang and Y. Zhao, Journal of Applied Physics **110**, 084103 (2011).

[133] K. H. Hellwege, A. M. Hellwege, *Eds. Ferroelectrics and Related Substances* **16**; Landolt-B€ornstein, New Series, Group III; Berlin, Germany: Springer, 1981.

[134] A. Schaefer, H. Schmitt, A. Dorr, Ferroelectrics **69**, 253 (1986).

[135] P. Parisiades, E. Liarokapis, J. Köhler, A. Bussmann-Holde and M. Mezouar, arXiv preprint arXiv:1505.05049. (2015).

[136] L. R. Edwards and R. W. Lynch, Journal of Physics and Chemistry of Solids **31**, 573. (1970).

[137] M. Guennou, P. Bouvier, J. Kreisel and D. Machon, Physical Review B **81**, 054115. (2010).

[138] S. Tsunekawa, K. Ishikawa, Z. Q. Li, Y. Kawazoe and A. Kasuya, Physical Review Letters **85**, 3440 (2000).

[139] I. Loa, P. Adler, A. Grzechnik, K. Syassen, U. Schwarz, M. Hanfland, G. K.Rozenberg, P. Gorodetsky and M. P. Pasternak, Physical Review Letters **87**, 125501 (2001).

[140] Z. Chen, C. Q. Sun, Y. Zhou and G. Ouyang, Journal of Physical Chemistry C **112**, 2423 (2008).

[141] A. San-Miguel, Chemical Society Reviews **35**, 876 (2006).

[142] J. P. Itie´, B. Couzinet, A. Polian, A. M. Flank and P. Lagarde, Europhysics Letters **774**, 706 (2006).

[143] F. Kruis, H. Fissan and A. Peled, Journal of Aerosol Science **29**, 511 (1998).

[144] G. Reiss and A. Hütten, Nature Materials **4**, 725 (2005).

[145] L. Takacs and J. McHenry, Journal of Material Science **41**, 5246 (2007).

[146] C. Suryanarayana, Progress in Material Science **46**, 1 (2001).

[147] V. Boldyrev and K. Tk*áč*ov*á*, Journal of Material Synthesis **8**, 121 (2001).

[148] A. Juh*á*sz and L. Opoczky, *Mechanical Activation of Minerals by Grinding: Pulverizing and Morphology of Particles*,Chichester, UK: Ellis Horwood, (1990).

[149] J. Dutta and H. Hofmann, In: H.S. Salva (Ed.) *Encyclopedia of Nanoscience and Nanotechnology*, Valencia, CA: American Scientific Publishers, 2004.

[150] P. Baláž, *Mechanochemistry in Nanoscience and Minerals Engineering*, Berlin, Germany: Springer, 2008.

[151] M. Marssi and R. Farhi, Journal of Applied Physics **80**, 1079 (1996).

[152] T. Tolstik, C. Marquadt, C. Matthaus, N. Bergner, C. Bielecki, C. Krafft, A. Stallmach and J. Popp, Analyst **139**, 6036 (2014).

[153] G. Kwei, A. Lawson and S. Billinge, Journal of Physical Chemistry **97**, 2368 (1993).